

AD621990

Columbia University  
in the City of New York

IONIZING SHOCK STUDIES IN AN  
ELECTROMAGNETICALLY DRIVEN  
SHOCK TUBE

by  
Bennett Miller

Best Available Copy



DDC  
RECEIVED  
OCT 18 1965  
RECEIVED  
DDC/PA

PLASMA LABORATORY  
SCHOOL OF ENGINEERING AND APPLIED SCIENCE  
NEW YORK 27, N.Y.

20370

IONIZING SHOCK STUDIES IN AN  
ELECTROMAGNETICALLY DRIVEN  
SHOCK TUBE

By

Bennett Miller

June, 1965

Plasma Laboratory  
Report No. 19  
S. W. Mudd Building  
Columbia University  
New York, N.Y., 10027

This study was supported in part by the Air Force Office  
of Scientific Research under Project AF-49(638)-1254.

26570

## ERRATA

- Page 3, line 30: "includēd" should read "included"
- Page 51, line 7: should read "...sions on the time scale in Fig. 26 and that, for convenience,  $U_l = 1$ . The recursion formula..."
- Page 51, line 10: "...EMF(at point 1)," should read "...EMF(at point 1)."
- Page 51, line 10: delete "where"
- Page 51, line 11: delete entire line
- Page 51, line 12: delete "...mensions and the shock velocity."
- Page 54, line 25: insert "is" between "traces" and "not" and between "but" and "rather"
- Page 58, line 15: "(See page 20)" should read (See page 16)"
- Page 108 - 114: All equation numbers in the text should be preceded by "A," e.g. "(1)" should read "(A1)"
- Page 113, line 11: "Fig. C" should read "Fig. A3"
- Page 118, line 10: "(3)" should read "(B3)"
- Page 119, line 6: "(6) should read "(B6)"
- Page 121, line 4: delete "î"
- Page 123, line 14: "Eq. (10)" should read "Eq. (C10)"
- Page 126, line 17: replace "the" with "A representative"
- Page 126, line 30: "applies applies" shc read "applies"

Page 127, lines 16 - 18

delete and replace with "Assuming we know  $U_{x_1}$  (that it is known remains to be seen), we know  $B(x_1, t_1 < t < t_2)$  because we know  $B_1, t, U$ , and the  $EMF(t)$ . Actually, we must know how to separate the time range  $t_1 < t < t_2$  from the complete  $EMF$  trace. Obviously, this can be done if one knows  $U_1$  and  $U_2$ . We will discuss later, how one obtains these quantities."

Page 128, line 10:

"Taussig<sup>25</sup>" should read "Taussig<sup>33</sup>"

Page 129, line 19:

delete "." after  $t_4$  and insert "and remain 0 for  $t > t_4$ ."

Page 128, line 20:

after "0" insert "and remains 0"

Page 128, line 20:

delete "To get  $U_1$ " and insert "The determination of  $U_1$  is slightly more involved. For the case shown in Fig. C3, it is clear that at  $t_1$  the  $EMF$  observed at the output of the pick-up probe will be 0. After  $t_1$  the  $EMF$  will rise or fall depending on the exact time variation of  $B$ . In any case, the velocity of the point at which the  $EMF$  departs from 0 will be  $U_1$  (it being understood that the time here considered is greater than  $\tau_r$ ). In other cases it may be that the  $EMF$  never falls to 0 except for  $t > t_4$ . In that event one can..."

Page 128, line 25:

after "in" insert "determining the various time regions (e.g. see equation 20) and for..."

## Table of Contents

	Abstract	iv
1.	Introduction	1
2.	History and Theory of Magneto-hydrodynamic Shocks	4
2.1	"Classical" Magneto-hydrodynamic Shocks	4
	2.1.1 Theor	4
	2.1.2 Experiments	17
2.2	Normal Ionizing Shocks	20
	2.2.1 Theory	20
	2.2.2 Experiments	28
3.	An Experiment To Verify the Theory of Normal Ionizing Shocks	30
3.1	Apparatus	30
	3.1.0 Introduction	30
	3.1.1 The Shock Tube	31
	3.1.2 The Magnetic Field	33
	3.1.3 The Capacitor Bank	34
	3.1.4 Air-Gap Switch	35
	3.1.5 Pre-ionization: Circuitry and Technique	36
	3.1.6 Control Circuitry	37
	3.1.7 Operation	38
3.2	Shock Tube Instrumentation	40
	3.2.0 Introduction	40
	3.2.1 Current Monitoring Loop	40
	3.2.2 Photomultipliers and Associated Circuitry	41
	3.2.3 Magnetic Field Probes	41
	3.2.4 Electric Field Probes	43
3.3	Data and Error Analysis	45
	3.3.0 Introduction	45

## Table of Contents (Cont'd.)

3.3.1	Shock Velocity Measurement	45
3.3.2	Instantaneous Current Measurement	47
3.3.3	Measurement of Switch-on and Drive Magnetic Field	48
3.3.4	Electric Field Measurements	56
3.4	Comparison with Theory	58
3.5	Conclusions	66
4.	References	67
5.	Acknowledgements	70
6.†	Figures and Tables	71
7.	Appendices	108
7.1	Appendix A: Analysis of the Capacitor-Inductor Bank When Used as a Square-Pulse Current Generator	108
7.2	Appendix B: Theory of Operation of the Current Monitor Probe	118
7.3	Appendix C: Measurement of Magnetic Fields in Moving Media	120
7.4	Appendix D: Shock Width and Shock Formation Study	132

---

† For list of figures and tables see Sec. 6.

## ABSTRACT

A coaxial electromagnetic shock tube has been used to study ionizing shocks propagating through hydrogen. An experiment is described which produced plane switch-on ionizing shocks. Studies were conducted covering the sub-Alfvenic, trans-Alfvenic and super-Alfvenic regimes. Data is presented that verifies the existence of switch-on fronts in all these regimes, and demonstrates the significant effect of the initial electric field on the shock jump conditions. The results substantiate the theory of normal ionizing shocks developed by Taussig.

A simple physical criterion, modeled on the Chapman-Jouguet (C-J) hypothesis, is employed to choose from among the several theoretically predicted ionizing waves propagating at a given speed. This criterion has strong intuitive support and results in a consistent picture of ionizing shock propagation that is in general agreement with our experimental observations. The existence of a small homogeneous plasma sample, behind the ionizing shock wave and before the expansion fan, is demonstrated. Previous failures to find large homogeneous plasma samples are shown to be consistent with the theory of ionizing shock waves and the C-J hypothesis.

## 1. INTRODUCTION

The present theory of shock phenomena in fluids has its roots in the middle of the nineteenth century. At that time, Riemann and Earnshaw<sup>1,2</sup> studied long wavelength, large amplitude disturbances propagating in media described by non-linear partial differential equations. Their studies lead to the prediction that under certain circumstances very narrow regions would form and propagate through a fluid. Across those regions the macroscopic properties of the fluid were expected to exhibit large scale changes. Those narrow spatial regions are what we know today as shock waves.

At the turn of the century, Vielle<sup>3</sup> conducted the first experimental study of shocks, but after his work interest unexplainably declined. Almost no studies were conducted during the next forty years with the exception of those conducted by Payman and his associates<sup>4</sup> in the "thirties." The hiatus was abruptly terminated by the onset of the Second World War. The Allies early recognized how little was known about the problems of detonation, explosion, trans-sonic flow, and super-sonic flow, areas that are all intimately connected with the formation and propagation of shock fronts.

During the war, Bleakney and his co-workers at Princeton started research into those areas. As a result of their studies the diaphragm, gas driven, shock tube became the basic tool of the scientist working in high temperature gas dynamics. By the early 1950's, Laporte at Michigan and Kantrowitz and his co-workers at Cornell had so refined the shock tube that they reached the practical limit of its ability to produce high temperature gases. They concluded that the maximum temperature obtainable in the conventional gas driven shock tube would be about 2 e.v.

But, by this time, the controlled thermonuclear program was under way and it called for laboratory analysis of dense gases at hundreds, and even thousands, of electron volts. By 1950 de Hoffman and Teller<sup>5</sup> had developed a theory of shocks in such immensely hot fluids. It was based on the model of an infinitely conducting fluid immersed in magnetic and electric fields and it served as the starting point for many subsequent theoretical studies.

In the early 1950's, Fowler et. al. developed a magnetically driven shock tube that was to become the forerunner of the coaxial electromagnetic shock tube.<sup>6</sup> Concurrently, the theory of de Hoffman and Teller was being expanded, dissected and reassembled. By 1959 the admissible solutions to the magneto-hydrodynamic (mhd) shock jump equations were well understood and thoroughly explored. Questions of mhd shock wave stability were being discussed and advances in understanding were being made. Experimental studies, however, were relatively crude and inconclusive. Most experiments involved strong shock waves propagating into a cold gas and hence were far from the mhd shock wave analyses based on an infinitely conducting fluid. In 1959, an attempt was made to generalize the original mhd shock theory so as to include the possibility of a jump in conductivity across the shock front. This approach was taken by two Russians<sup>7,8,9</sup> who investigated the mathematical properties of a shock propagating into a gas whose conductivity was assumed zero and of such strength that the gas behind could be assumed infinitely conducting. This model allows the upstream gas to support an arbitrary electric field and gives rise to the type of discontinuity that will occupy us in this study - the ionizing shock. Other pioneering work in this area was done by Gross and Kunkel<sup>10</sup> and Helliwell and Pack<sup>11</sup>,

in 1962. More recent studies will be described in the body of this report. With this introduction we turn our attention to the report itself.

Chapter 2 is divided into two parts. The first is devoted to a concise exposition of the "classical" theory of magneto-hydrodynamic shocks, i.e. shocks allowed in a gas whose conductivity is infinite, while the second presents and explains the most important features of the latest theory of ionizing shocks.

Chapter 3 has five sections. The first two constitute a complete report on the construction, operation and instrumentation of a coaxial electromagnetic shock tube. The third explains reduction of the raw data to a form convenient for comparison with theory. The fourth presents a proposal that describes, simply and consistently, the behavior of ionizing shocks. The proposal is based on the theory developed in the second section of Chap. 2 and on the data in the third section of the third chapter. The reduced data is compared with the proposal and conclusions are drawn in the fifth section.

Four appendices are included to present material mentioned, but not treated, in the text. The first two are summaries of the theory of shaped-pulse capacitor banks and current monitor probes. They have been included for completeness and to simplify the reader's approach to each area. The third (Appendix C) develops a complete picture of the application of coil probes to the measurement of magnetic fields in moving media. The treatment is significant in that it points up the danger of using an oversimplified view of such probes and further, a general result is derived that is applicable to all such instrumentation. Appendix D has been included to present additional data obtained during these experiments. Some data on ionizing shock formation time and ionizing shock thickness is contained therein.

## 2. HISTORY AND THEORY OF MAGNETO-HYDRODYNAMIC SHOCKS

### 2.1 "Classical" Magneto-hydrodynamic Shocks

#### 2.1.1 Theory

It is generally acknowledged that the first treatment of magneto-hydrodynamic (mhd) shocks was the work of de Hoffman and Teller<sup>5</sup> in 1950. However, their treatment was by no means exhaustive, and it was not until the work of Bazer and Ericson<sup>12</sup> in 1959 that a careful study was done of the admissible solutions to the shock jump equations. The work of Bazer and Ericson leaned most heavily on two earlier papers. The first was an incisive study by Friedrichs<sup>3</sup> of non-linear wave motion. He was the first to recognize the "switch-on" behavior of one class of shock jump solutions. And the second, which lead directly into the work of Bazer and Ericson, was a study by Friedrichs and Kranzer<sup>14</sup> which amplified and extended Friedrich's earlier analysis.

At the same time that these papers were being authored, independent work was progressing in the same area. Between 1950 and 1959 important work was completed by Lüst<sup>15</sup> who derived directly the non-relativistic mhd shock jump equations (in contrast to the work of de Hoffman and Teller which was done within a relativistic framework) and by Lundquist<sup>16</sup> who was the first to treat the non-linear, hyperbolic system of partial differential equations that govern non-dissipative magneto-hydrodynamic flow. Even as far back as 1949 and 1950<sup>17,18</sup> there were studies showing the remarkable feature that characterizes mhd flow, the existence of three distinct,

directionally dependent, small-disturbance propagation speeds. However, these earlier studies evolved in connection with a linearized approach to the mhd problem and so could not treat shock phenomena.

To set the framework for subsequent discussions a necessarily brief discussion of "classical" mhd shock theory will be presented. Here the word "classical," far from meaning old or well understood, is simply being used to distinguish mhd shock studies done in infinitely conducting media from the more recent work done on ionizing shocks, where the pre-shocked gas is considered to be completely non-conducting ( $\sigma = 0$ ), and only the post-shock gas is assumed to be infinitely conducting.

The appearance of shocks in any real fluid is bound up with the non-linear nature of the partial differential equations that govern the flow. In the study of infinitely conducting media with all dissipative coefficients taken as zero, the equations form a system of eight scalar partial differential equations coupling Maxwell's laws with the fluid equations that specify conservation of mass, momentum and energy. The equations, often called the Lundquist equations,<sup>19</sup> are:

$$\frac{\partial \vec{H}}{\partial t} - \nabla \times (\vec{v} \times \vec{H}) = 0 \quad (1)$$

$$\left(\frac{\partial}{\partial t} + \vec{v} \cdot \nabla\right) \rho + \rho \nabla \cdot \vec{v} = 0 \quad (2)$$

$$\left(\frac{\partial}{\partial t} + \vec{v} \cdot \nabla\right) \vec{v} + \frac{1}{\rho} \nabla p(\rho, s) - \frac{\mu}{\rho} (\nabla \times \vec{H}) \times \vec{H} = 0 \quad (3)$$

$$\left(\frac{\partial}{\partial t} + \vec{v} \cdot \nabla\right) s = 0 \quad (4)$$

where  $\vec{H}$  is the magnetic field,  $\vec{v}$  is the fluid velocity with respect to any fixed reference frame,  $\rho$  is the fluid

density;  $p$  is the fluid pressure considered as a function of the two thermodynamic variables  $\rho$  and  $S$  (entropy), and  $S$  is the fluid entropy.

Equation (1) is derived from Maxwell's equations with displacement currents neglected (a  $(\frac{v}{c})^2 \ll 1$  approximation) and  $\sigma$  (electrical conductivity) assumed infinite. Equation (2) is the well-known statement of mass conservation. Equation (3) is a statement of conservation of momentum in the fluid. It is derived by assuming:

a) that  $\nabla \times \vec{H} = \vec{j}$  so that the  $\vec{j} \times \vec{B}$  term in the Lorentz force can be written as  $\mu(\nabla \times \vec{H}) \times \vec{H}$ :

b) that the Debye shielding distance is so small in comparison to any flow length that the body force due to interaction of the electric field  $\vec{E}$  with any net charge density can be neglected;

c) that gradients are sufficiently gentle so that the scalar pressure term dominates the viscous force term, and

d) that gravitational effects are neglected.

Equation (4) states that the system is reversible and adiabatic - entropy is conserved. This equation is derived from the general energy conservation equation by neglecting all dissipative effects. It is obvious that Eq. (4) simply means that  $p$  and  $\rho$  are connected through the adiabatic equation of state  $p = A(S)\rho^\gamma$ .

A system of equations such as just described would seem at first sight to be so restrictive as to be inapplicable. Just the contrary is the case, for one need only assume that the particle distribution function in the fluid is "local" Maxwellian to prove that it is precisely these equations that will govern mhd fluid flow.<sup>20</sup> The achievement of a "local" Maxwellian distribution is obviously effected through

collisions and so the validity of the Lundquist system depends on how fast and within what length scale an arbitrary distribution is "Maxwellized." Petscheck and Kantrowitz<sup>21</sup> have discussed reasonable criteria for estimating the range of temperature and electron density within which the Lundquist equations are valid. They argue that the characteristic length,  $L$ , of the flow field must satisfy two conditions:

$$L \gg \frac{3 \times 10^{-14} T^2}{N_e} \quad (5a)$$

$$L \gg 2/T^2 \quad (5b)$$

where  $L$  is in centimeters,  $T$  is temperature in e.v. and  $N_e$  is the electron number density in particles/cc. If 5a and 5b are satisfied, the Lundquist equations can be assumed to govern the behavior of the flow field. The inequalities 5(a) and 5(b) represent a dimensional analysis of the assumptions used in deriving the Lundquist equations. For example, if we assume  $\sigma \gg 0$  we are actually requiring that the magnetic Reynolds number,  $R_m = \mu \sigma v L$ , be much greater than 1, where  $L$  is, as before, the characteristic length of the flow field and  $v$  is the characteristic fluid velocity. Further, the isentropic assumption is equivalent to saying that during the characteristic flow time,  $\frac{L}{v}$ , the amount of heat added to the fluid via conduction is much less than the thermal energy of the plasma. Thus, we require  $k \frac{T}{L^2} \cdot \frac{L}{v} \ll \rho C_p T$  where  $k$  is the heat conduction co-efficient, and  $C_p$  is the heat capacity at constant pressure. In a similar fashion, we require  $L \gg$  Debye length to insure electrical neutrality. Then, using kinetic theory expressions for  $k$ , and  $\sigma$ , 5(a) and 5(b) can be constructed.

If an attempt is made to construct a solution to the system (1) through (4), subject to explicit boundary conditions and using any sensible power series expansion, one finds that there exist special surfaces, called characteristic surfaces, on which one cannot specify initial data and still construct a solution, and across which there can exist jump discontinuities in the derivatives of the dependent variables. This is a direct result of the hyperbolic nature of the system of equations.<sup>19</sup> In addition, as is well-known in ordinary gas dynamics, there is a critical time (after the initiation of some compressive fluid disturbance) beyond which a unique continuation of a smooth solution to a flow problem is impossible.<sup>22</sup> After this time the situation is no longer described by the Lundquist equations, and finite discontinuities or "jumps" will appear in the dependent variables. This is the mathematical origin of shock waves.

The shock problem is immensely simplified as a result of the conservation form of the differential equations that govern the continuous flow, i.e., as we have seen in the Lundquist equations, each equation consists of the sum of derivatives of functions involving the dependent variables. From this fact it can be shown<sup>19</sup> that across a shock the dependent variables are related by a system of algebraic equations directly derivable from the original partial differential equations through any one of several equivalent approaches. One may use a generalized Rankine-Hugoniot relation,<sup>19</sup> or a simple substitution technique first used by Friedrichs,<sup>13</sup> or, finally, the direct integration approach which treats the shock as an infinitesimal discontinuity and requires integration from the constant state ahead of the shock to the constant state behind.<sup>22</sup> Each method gives the same set of algebraic jump equations relating flow properties on one side of the shock

to flow properties on the other. If the set of jump equations is viewed from the rest frame of the shock and, if it is assumed that the flow is one-dimensional (in the x-direction), then all the dependent variables are functions only of x and t, and the jump equations become:

$$H_x = \text{constant} \quad A1$$

$$H_{z2} u_2 - H_x w_2 = H_{z1} u_1 - H_x w_1 \quad A2$$

$$\rho_2 u_2 = \rho_1 u_1 \equiv m \quad A3$$

$$\rho_2 u_2^2 + p_2 + \frac{\mu H_{z2}^2}{2} = \rho_1 u_1^2 + p_1 + \frac{\mu H_{z1}^2}{2} \quad A4$$

$$\rho_2 u_2 w_2 - \mu H_x H_{z2} = \rho_1 u_1 w_1 - \mu H_x H_{z1} \quad A5$$

$$m \left( \frac{\gamma}{\gamma-1} \frac{p_2}{\rho_2} + \frac{u_2^2 + w_2^2}{2} \right) + \mu H_{z2} (H_{z2} u_2 - H_x w_2) = m \left( \frac{\gamma}{\gamma-1} \frac{p_1}{\rho_1} + \frac{u_1^2 + w_1^2}{2} \right) + \mu H_{z2} (H_{z2} u_2 - H_x w_2) + \mu H_{z1} (H_{z1} u_1 - H_x w_1) \quad A6$$

$$m [S_2(p, \rho) - S_1(p, \rho)] \geq 0 \quad A7$$

where the numerical subscript 1 (2) denotes the region ahead of (behind) the wave, the flow velocity vector  $\vec{v}$  has components (u, 0, w) and the magnetic field vector  $\vec{H}$  has components (H<sub>x</sub>, 0, H<sub>z</sub>). The geometry is shown in Fig. 1. The fact that the flow vector and the magnetic field ahead of and behind the wave can be restricted to the x-z plane without any consequent loss of generality is proved in Bazer and Ericson.<sup>1,2</sup>

To establish the basic situation with which we will be concerned in all subsequent discussions, let us now require that the fluid ahead of the shock be at rest in the laboratory reference frame, and even more important, that  $H_{z1} = 0$ . It is this latter restriction which gives rise to the designation "normal" shock since, in this case, the shock front is normal to the magnetic field ahead of it. By virtue of the fact that the shock frame has been assumed in motion along the x-axis we get

$$0 = u_1^{LF} = u_1 + U_s \text{ or } u_1 = -U_s, \text{ and} \quad (6)$$

$$0 = w_1^{LF} = w_1 \quad (7)$$

where the superscript LF means that the quantity is to be considered in the laboratory frame and  $U_s$  is defined to be the velocity of the shock with respect to the laboratory frame. With these substitutions A1-A6 become A1'-A6':

$$H_x = \text{constant} \quad A1'$$

$$H_{z2} u_2 - H_x w_2 = 0 \quad A2'$$

$$\rho_2 u_2 = \rho_1 u_1 \equiv m \quad A3'$$

$$\rho_2 u_2^2 + p_2 + \frac{\mu H_{z2}^2}{2} = \rho_1 u_1^2 + p_1 \quad A4'$$

$$\rho_2 u_2 w_2 - \mu H_x H_{z2} = 0 \quad A5'$$

$$m \left( \frac{\gamma}{\gamma-1} \frac{p_2}{\rho_2} + \frac{u_2^2 + w_2^2}{2} \right) + u H_{z2} (H_{z2} u_2 - H_x w_2) = m \left( \frac{\gamma}{\gamma-1} \frac{p_1}{\rho_1} + \frac{u_1^2}{2} \right) \quad A6'$$

Assuming that we know  $u_1^{LF}$ ,  $\rho_1, p_1, H_{x_1}$ , the system A1'-A6' constitutes a set of 6 equations in the seven unknowns:  $U_s, H_{x_2}, H_{z_2}, u_2, w_2, p_2$  and  $\rho_2$ . The system, therefore, determines a one-parameter family of solutions for the downstream states in terms of some given upstream state. We note that A7 has not been considered since it only serves to separate the entropy increasing solutions from the entire set of solutions. A complete discussion of all the admissible solutions to A1'-A6' (excluding stability considerations) is given in Bazer and Ericson.<sup>12</sup> A review of some major features of the solutions will be presented below. First, however, a few general remarks about mhd shocks are in order.

In striking contrast to the situation in ordinary gas dynamics, the mhd jump equations admit two distinct kinds of shocks, each of which propagates with a distinct velocity. A plausibility argument that illustrates this behavior proceeds as follows. In conventional compressible fluid theory a shock forms in the following way. Let an infinitesimal, compressive pressure pulse be driven into a cold gas. The disturbance propagates through the cold gas at the sound speed,  $a_1$ . The gas behind the pulse is at a slightly higher temperature by virtue of the pulse's compressive nature. The sound speed in the compressed region is now  $a_2 > a_1$  since the square of the sound speed depends solely and linearly on the temperature. If a second compressive pressure pulse is later initiated at the same boundary as the first it propagates into the slightly heated gas at  $a_2 > a_1$  and, therefore catches up with the first disturbance. Similarly a third pulse catches the first two, and a fourth, the preceding three. In this way, a sharp spatial discontinuity is established in the gas (i.e., a shock is formed). The ordinary gas dynamic

equations yield only one small-disturbance propagation speed, the sound speed, and hence only one kind of shock can be produced. The mhd equations, however yield three different, small amplitude propagation speeds. They are generally denoted by  $C_{fast}$ ,  $C_{intermediate} \equiv b_n$  and  $C_{slow}$  and they are characterized by the inequalities:

$$C_{slow} \leq a \leq C_{fast} \quad (8)$$

$$C_{slow} \leq b_n \leq C_{fast} \quad (9)$$

In (8) and (9)  $a$  is the ordinary sound speed in the gas and the "intermediate" wave speed,  $b_n$ , often called the transverse wave speed, is just the ordinary Alfvén speed,  $b = \frac{\sqrt{u_0} |\vec{H}|}{\sqrt{\rho}}$ , with  $|\vec{H}|$  replaced by the component of  $\vec{H}$  in the propagation direction  $\vec{n}$ .

It is apparent that in the case in which the magnetic field is parallel to the propagation direction,  $b_n = b$ . In the same case, it can be shown there is a degeneracy that requires  $C_{fast}$  to coincide with either  $a$  or  $b$  depending on which of these is larger.<sup>1,3</sup> The ratio  $a/b$ , then, becomes an important parameter in mhd shock theory. From now on we will restrict ourselves to the situation where  $a/b < 1$ , since it is only in this case that the shock solutions admit the important "switch-on" wave.<sup>1,2</sup> We will have more to say about this later.

In exact analogy with ordinary gas dynamics, a pressure pulse propagating at any of the three small-disturbance speeds might be expected to form a shock and therefore we would expect to find three different shocks possible in any mhd fluid flow. However, an "intermediate" or transverse small-distur-

bance will not exhibit any steepening tendency. An infinitesimal transverse pulse leaves both density and magnetic field behind it unchanged. Hence, the propagation speed behind the wave is identical to that in front and subsequent pulses do not "catch" the initial disturbance. Large amplitude disturbances of the transverse variety can be propagated without any change in shape. Only fast and slow pressure pulses exhibit the kind of steepening behavior that characterizes a pressure pulse propagating in an ordinary gas dynamic situation. Thus, it is the fast and slow waves that give rise to the two shock modes spoken of above. Known as the fast and the slow shock, these modes derive their names, quite obviously, from the fact that the former is formed by pressure pulses traveling at the fastest of the three small disturbance speeds and the latter is formed from pressure pulses traveling at the slowest of the three small-disturbance speeds.

We now turn our attention directly to A1'-A6'. Following Taussig<sup>33</sup> we introduce the following dimensionless variables:

$$\tilde{u}_i = \frac{|u_i|}{b_{xi}}, \quad \tilde{a}_i = \frac{a_i}{b_{xi}}, \quad \tilde{w}_i = \frac{w_i}{b_{xi}}, \quad b_i = \frac{D_{zi}}{b_{xi}}, \quad i = 1, 2 \quad \text{where}$$

$$b_{xi} = \sqrt{\frac{\mu}{\rho_i}} H_x, \quad b_{zi} = \sqrt{\frac{\mu}{\rho_i}} H_{zi} \quad \text{and} \quad a_i = \sqrt{\frac{\gamma P_i}{\rho_i}}.$$

Substituting into A1'-A6' the system is reduced to dimensionless form. Solving for  $\tilde{u}_2$  (assuming for convenience, that  $\gamma = \frac{5}{3}$ ) we derive a fourth order equation for  $(\tilde{u}_2)^2$ ,

$$\left(\frac{1-\tilde{u}_2^2}{2}\right)(\tilde{u}_1^2 - \tilde{u}_2^2)[\tilde{u}_1^2 - (4\tilde{u}_2^2 - 3\tilde{a}_1^2)] = 0. \quad (10)$$

Equation (10) obviously has four roots, one of which is double:

$$\tilde{u}_2^2 = 1, \quad \text{a double root;} \quad (11a)$$

$$\tilde{u}_2^2 = \tilde{u}_1^2; \quad \text{and} \quad (11b)$$

$$\tilde{u}_2^2 = \frac{1}{4}(\tilde{u}_1^2 - 3\tilde{a}_1^2). \quad (11c)$$

These are plotted in Fig. 2. With these solutions for  $\tilde{u}_2$  in terms of the parameter  $\tilde{u}_1$  (we have already assumed  $\tilde{a}_1$  fixed and  $< 1$ ) we can go back to A1'-A6' and solve systematically for all the shock properties in region 2. This has been done by Bazer and Ericson.<sup>1,2</sup>

The solution  $\tilde{u}_2^2 = \tilde{u}_1^2$  represents the trivial "null" solution to the jump equations, that is, all the shock properties remain unchanged across the shock. Though trivial, the null solution is by no means unimportant. In Fig. 2 it represents the dividing line between regions of admissible and inadmissible solutions. All solutions in the region  $\tilde{u}_2 > \tilde{u}_1$  are not physically realizable because they imply a negative entropy change across the shock. This can be seen immediately from the fact that for  $\tilde{u}_2 > \tilde{u}_1$ ,  $\rho_2 < \rho_1$ . But, expansive shocks are entropy decreasing shocks, and are therefore not allowed. (For proof of this see Bazer and Ericson<sup>1,2</sup> where it is also proved that only compressive shocks,  $\rho_2 > \rho_1$ , have  $S_2 > S_1$ ). In addition, the null solution gives rise to an important class of solutions in the theory of ionizing shocks (see Sec. 2.2.1).

The solution  $\tilde{u}_2^2 = 1$  is represented by the straight line BC in Fig. 2. Note that to the left of B there can be

no solutions because  $\rho_2 < \rho_1$ . The line BC is the switch-on solution that has already been mentioned several times but has not been discussed. The switch-on wave has three salient features. First, if  $\tilde{u}_2^2 = 1$  is substituted in A1'-A6' and if we solve for  $H_{z2}$ , we find that along BC,  $H_{z2} \neq 0$ . A direct result of this fact is that a current flows through the shock and, using  $\nabla \times \vec{H} = \vec{j}$ , the current density is of precisely the magnitude necessary to produce the  $H_{z2}$  predicted. The qualitative behavior of  $H_{z2}$  along BC is easy to predict.  $H_{z2}$  is initially 0 at B, as it must be since B is on the null solution where properties are unchanged across the wave. It rises to a maximum at some point along BC and falls to 0 at point C. Beyond C,  $H_{z2}$  is imaginary and therefore, no solutions exist. Thus, across a switch-on shock there is a sudden appearance of a tangential magnetic field and an associated tangential fluid velocity, determined by A2'. A magnetic, as well as a shear discontinuity, has been switched-on behind the shock. It is to be noted that only the switch-on solution (SW) exhibits this behavior. Since this shock has no ordinary gas dynamic analog (a shear discontinuity cannot be supported in ordinary fluid flow) it has been the subject of intensive theoretical and experimental investigation.

The second feature of switch-on shocks is that the flow field behind the shock has a normal component relative to the shock which is exactly the normal Alfvén velocity,  $b_n$ , and which remains unchanged as the shock speed increases. And third, the switch-on shock divides the  $\tilde{u}_2 - \tilde{u}_1$  diagram into two distinct regions, the slow shock region  $\tilde{u}_2 < 1$ , and the fast shock region  $\tilde{u}_2 > 1$ , where the designations "slow" and "fast" conform to the definitions of Bazer and Ericson.<sup>12</sup>

The question of switch-on stability has not yet been answered in full. It has been shown that the switch-on shock has a unique structure<sup>23</sup> but beyond that very little conclusive work is available.

The solution  $\tilde{u}_2^2 = \frac{1}{4} (\tilde{u}_1^2 - 3\tilde{\alpha}_1^2)$  has been plotted as the curve C'ADCE $\infty$ . It has three distinct regions: O'A, ADC, and CE  $\infty$ . O'A is inadmissible from entropy considerations. ADC is classed as a slow gas shock solution and CE  $\infty$ , a fast gas shock solution. The adjective "gas" is used to indicate that the solutions behave somewhat like classical gas dynamic shocks in that no tangential magnetic field or velocity is switched on. Though neither of the admissible solutions exhibit switch-on behavior, nevertheless they have come in for extensive review, particularly DC. Taniuti and Jeffrey<sup>19</sup> report that DC is a non-evolutionary solution, i.e., it is a solution of the jump equations but it is not a solution that is continuously dependent on infinitesimal changes in boundary conditions. Gardner and Kruskal<sup>24</sup> conclude that it is not stable, while Petcheck and Kantrowitz<sup>21</sup> have argued for the interpretation that DC is an extraneous solution.

All the arguments suffer from one following criticism. If we must exclude DC, we may ask what happens in a piston problem to slow shocks that are driven at speeds just beyond those corresponding to the point D. Must they jump to a switch-on type of discontinuity, even though the piston need not be constrained to rotate? Or, if not, what does happen? The questions are unanswered. The regions AD and CE $\infty$  are well understood. The former is evolutionary but has not yet been shown to be stable.<sup>19</sup> The latter has been demonstrated to be both stable and evolutionary.<sup>19</sup>

### 2.1.2 Experiments

As early as 1951 strong mhd shocks were being generated in the laboratory, though they were not recognized nor studied as such at the time.<sup>6</sup> The devices then used were known as T-tubes for they consisted of a glass vessel in the form of a T. Embedded in the head of the T were two electrodes between which an intense electrical discharge was initiated. By bringing the return current path near the discharge (called back-strapping) the current was driven by the Lorentz force into the stem of the T forming a strong shock wave in the process. By 1957 Kolb,<sup>25</sup> using the T-tube, had driven a deuterium plasma at approximately 15 cm/ $\mu$ s, graphically demonstrating the immense advantage the electromagnetic driver enjoys over the conventional pressure driver. However, most of the T-tube studies were concerned with producing a hot plasma for use as a spectroscopic source and little work was done in verifying mhd shock jump properties.

The first attempt to verify, in any sense, the mhd jump equations was made by Patrick in 1959<sup>26</sup> using a magnetic annular shock tube (MAST). Since the operation of the Columbia coaxial shock tube described in chapter 3 is a close parallel to the MAST, we need only mention that the MAST provided cleaner, more reproducible laboratory conditions for mhd shock formation than the T-tube.

In any laboratory situation it is crucial that there be available an accurate theoretical analysis of the operation of laboratory devices, and the mhd shock problem is no exception. Without a theory of electromagnetic shock tube opera-

tion, it would be a hopeless task to try to verify the shock jump equations. For this reason much work has been done on solving the shock formation problem in the context of a realistic laboratory boundary value problem. The earliest theoretical model, advanced by Garwin and Rosenbluth in 1954,<sup>27</sup> was the "snowplow" model. Still in use today as a good qualitative description of the "magnetic" piston (see Sec. 3.1.1 for more discussion of this term), the theory described the drive current sheet as a "snowplow" pushing gas ahead of it and establishing a strong shock. In 1958, Wright and Black<sup>28</sup> extended this model by including acceleration of the "snowplow" and discussing the time that must elapse before steady conditions prevail in any electromagnetically driven shock tube. Kemp and Petscheck<sup>29</sup> further refined the shock tube problem. They allowed gas to flow through the snowplow by considering a rarefaction fan that carried the drive current, but, more important, they motivated their work with reference to the experimental design of Patrick<sup>28</sup> so that a device and a theory were simultaneously available. The analysis predicted that between the shock and the rarefaction fan one should find, as one would hope, a region of uniform hot plasma, i.e., precisely the uniform region behind the shock that we have been calling region 2. Patrick's initial work<sup>28</sup> showed that reasonable agreement between observed shock velocities and those predicted by the Kemp and Petscheck model could be obtained. Later work<sup>30</sup> showed marginal evidence of the formation of a homogeneous gas sample (hgs) behind a strong mhd shock, and also some of the magnetic compression effects that occur in the case of non-normal fields.

The most recent attempts to verify the jump equations, with only normal fields being imposed, have not been conclusive. Heiser<sup>31</sup> shows evidence of switch-on behavior but his

results contain great scatter and are open to differing interpretations. Heywood<sup>32</sup> states that for the normal field configuration, the Kemp and Petschek model does not describe shock tube behavior since neither hgs nor switch-on behavior could be observed or produced in his experiment. In sum, through January 1965, there has been no complete experimental study of the "classical" mhd shock problem, let alone the special normal case.

The most important reason for the lack of any definitive experimental studies is that the classical theory requires that any mhd shock be formed in an already infinitely conducting fluid. Since such a fluid is not readily available, the question of producing one becomes pertinent. One way to do so would be to take a cold non-conducting gas ( $\sigma = 0$ ), drive a strong shock through it and make it infinitely conducting. This approach leads, quite naturally, to the study of the ionizing shock. If we restrict ourselves, as above, to only normal magnetic fields we have normal ionizing shocks. Their properties and their theory will now be presented.

## 2.2 Normal Ionizing Shocks

### 2.2.1 Theory

The extension of "classical" mhd shock theory to the case where the fluid is assumed to have finite conductivity is accomplished by the trivial addition of a Poynting vector term to the energy jump equation.<sup>11</sup> The consequences of the addition of this term, however, are anything but trivial. Not only does it produce a whole new class of possible solutions to the jump equations, but it also predicts phenomena heretofore totally unexpected and unappreciated.

By a normal ionizing shock we mean that we restrict ourselves to the case of a normal magnetic field, a stationary fluid ahead of the shock in the laboratory frame, an electric field only in the plane of the shock ( $E_x \equiv 0$  everywhere) and a theoretical model in which the gas upstream of the shock has  $\sigma = 0$  and downstream  $\sigma = \infty$ . It then follows quite simply, that the jump equations governing normal ionizing shock are A1'-A6' with the addition of a term  $+E_y H_{z2}$  to the left hand side of A6'. For convenience we will rewrite these equations as B1-B6, with all quantities in the shock frame.

$$H_x = \text{constant} \quad (\text{B1})$$

$$H_{z2} u_2 - H_x w_2 = 0 \quad (\text{B2})$$

$$\rho_2 u_2 = \rho_1 u_1 \equiv m \quad (\text{B3})$$

$$\rho_2 u_2^2 + p_2 + \frac{\mu H_{z2}^2}{2} = \rho_1 u_1^2 + p_1 \quad (\text{B4})$$

$$\rho_2 u_2 w_2 - \mu H_x H_{z2} = 0 \quad (\text{B5})$$

$$m \left( \frac{\gamma}{\gamma-1} \frac{p_2}{\rho_2} + \frac{u_2^2 + w_2^2}{2} \right) + \mu H_{z2} (H_{z2} u_2 - H_x w_2) + E_y H_{z2} =$$

$$m \left( \frac{\gamma}{\gamma-1} \frac{p_1}{\rho_1} + \frac{u_1^2}{2} \right) \quad (\text{B6})$$

Using B2 and B6 reduces this system to B1'-B5', the system that will be used from now on.

$$H_x = \text{constant} \quad (\text{B1}')$$

$$\rho_2 u_2 = \rho_1 u_1 \quad (\text{B2}')$$

$$\rho_2 u_2^2 + p_2 + \frac{\mu H_{z2}^2}{2} = \rho_1 u_1^2 + p_1 \quad (\text{B3}')$$

$$\rho_2 u_2 w_2 - \mu H_x H_{z2} = 0 \quad (\text{B4}')$$

$$m \left( \frac{\gamma}{\gamma-1} \frac{p_2}{\rho_2} + \frac{u_2^2 + w_2^2}{2} \right) + E_y H_{z2} = m \left( \frac{\gamma}{\gamma-1} \frac{p_1}{\rho_1} + \frac{u_1^2}{2} \right) \quad (\text{B5}')$$

It is to be noted that  $E_y$  appears without subscript 1 or 2. This is a direct result of the fact that  $E_y$  is constant across the shock. Also implicit in the system B1'-B5' is the fact that  $\vec{E}$  has been assumed to be of the form  $(0, E_y, 0)$ , an assumption that can be made with no loss of generality for, by rotating one's coordinate system, the vanishing of  $E_z$  can always be assured ( $E_x \equiv 0$  everywhere has already been required).

The major departure, in physical terms, of the ionizing shock model from the classical model is the ability of the

upstream non-conducting gas to support a nonzero electric field that is independent of flow velocity and magnetic field in that region. Only in the region behind the shock where  $\sigma = \infty$  must we require that  $\vec{E} = -\vec{v} \times \vec{B}$ . Since the upstream electric field is allowed to take on arbitrary values, we expect  $E_y$  to appear as a parameter in any ionizing shock theory. This is precisely the case.

The particular model chosen to describe ionizing shocks was adopted because it permits the simplest theoretical treatment. By a straightforward exercise in the use of the Galilean transformation  $\vec{E}' = \vec{E} + \vec{v} \times \vec{B}$  one can easily rewrite  $E_y$  in the shock frame in terms of the downstream variables (or, since  $E_y$  is a parameter it might be more appropriate to think in terms of relating the downstream variables to  $E_y$ ). The relationship is

$$E_y = \mu(u_2 H_{z2} - w_2 H_x). \quad (12)$$

If (12) is used in B5' and if the dimensionless variables already introduced in 2.1.1 are supplemented by an additional dimensionless variable  $\tilde{E} = \frac{E_y}{\sqrt{\mu\rho_1} b_{x_1}^2}$ , then B1'-B5' can be reduced exactly as A1'-A6' was reduced in Sec. 2.1.1. The generalization of (10) becomes

$$\left(\frac{1-\tilde{u}_2^2}{2}\right)^2 (\tilde{u}_1^2 - \tilde{u}_2^2)[\tilde{u}_1^2 - (4\tilde{u}_2^2 - 3\tilde{a}_1^2)] + \frac{3}{8}(\tilde{u}_1 \tilde{E})^2 \left(\frac{2}{3} + \frac{\tilde{u}_2^2}{2}\right) = 0. \quad (13)$$

As before we have  $\tilde{u}_2$  as a function of  $\tilde{u}_1$  but in addition we now have  $\tilde{E}$  playing the role of a parameter. (As in Sec. 2.1 we fix, a priori,  $\frac{a}{b} < 1$ .)

Equation (13) was first derived and discussed in full detail by Taussig,<sup>33</sup> although the actual problem was first appreciated by Liubimov and Kulikovsky in 1959.<sup>7, 8, 9</sup> The substance of Taussig's work will be presented here. There are several important features that distinguish normal ionizing shock solutions from classical mhd shock solutions. Most can be described by referring to Fig. 3, reprinted, with additions, from Taussig's report. The heavy black lines represent the  $\tilde{E} = 0$  solutions discussed in Sec. 2.1.1 and presented in Fig. 2. For a given  $\tilde{E} > 0$  the solutions to (13) are shown as the light curves in Fig. 3. Three features are immediately apparent. First, the  $\tilde{E} > 0$  solutions are bounded by the  $\tilde{E} = 0$  solutions and this is, in fact, true for any  $\tilde{E} > 0$ . Second, if  $\tilde{E}$  is specified, there are ranges for which no shock solutions are available, e.g., the region  $q_1 < \tilde{u}_1 < q_2$  contains no real solutions to Eq. (13); and also, the contours that describe the  $\tilde{E} > 0$  solutions are separate and distinct as is evident from the figure. Third, contours in ABC are closed curves while in O'AO and E'BCE they are open curves.

Not so evident is the fact, proved by Taussig, that all solutions for  $\tilde{E} > 0$  are nested within the  $\tilde{E} = 0$  boundary in a way such that, for any two values of  $\tilde{E}$ , denoted  $\tilde{E}_1$  and  $\tilde{E}_2$ , if  $\tilde{E}_2 > \tilde{E}_1$ , then the  $\tilde{E}_2$  contour must lie within the  $\tilde{E}_1$  contour. Further arguments can be advanced to prove that not only are the  $\tilde{E} > 0$  solutions nested, but there exists a critical value of  $\tilde{E}$ , denoted by  $\tilde{E}^*$ , such that beyond  $\tilde{E}^*$  there exists no solutions to (13) within region ABC. This means that as we increase  $\tilde{E} \rightarrow \tilde{E}^*$  the closed contours in ABC shrink to a point. In the same limit of  $\tilde{E} \rightarrow \tilde{E}^*$ ,  $q_2 \rightarrow \infty$  and  $q_1 \rightarrow 0$ .

Each contour for a particular  $\tilde{E} > 0$  solution is divided into several sections which join continuously. The sections are labeled N, G, and SW corresponding to the portion considered being closest to the null (N), gas (G) or switch-on (SW) solution of the  $\tilde{E} = 0$  case, respectively. This division is far from arbitrary. It corresponds to distinct differences in the jump properties across the shock. One determines the jump properties as before by going back to the full set of equations B1'-B5' and systematically solving for all variables in region 2, given  $\tilde{u}_1$  and  $\tilde{u}_2$ . Two important results of such a program must be mentioned:

- 1) unambiguous, switch-on behavior is extended to all the  $\tilde{E} > 0$  shock solutions, and
- 2) the null branch of any contour becomes a full-fledged shock in contrast to the "null shock" in the  $\tilde{E} = 0$  theory, which is simply a mathematical result with no physical significance.

In regard to the first of these points we note that switch-on behavior is not only extended to slow and fast shocks but, even more remarkably, to the expansive shocks in region O'A0.

This brings us to another of the unexpected features of normal ionizing shocks - the admissibility of expansive shocks from an entropy viewpoint.

Consideration of the Hugoniot equation for normal ionizing shocks leads to the conclusion that in ABC all solutions are entropy increasing, while in O'A0 and E'BCE only the solutions from the "bracket" points,  $\bar{1}$ , in the direction of the arrow are entropy increasing (see Fig. 3). Thus, as stated above, at least a sub class of expansive shocks is admissible as a shock solution while, as already noted in the classical theory all expansive shocks are excluded.

The problem of stability and evolutionarity has not yet been successfully attacked for the case of normal ionizing shocks. Only transverse ionizing shocks (i.e., ionizing shocks where  $\vec{H}$  is parallel to the shock front) have been shown to be evolutionary. This was done by C.K. Chu in 1964.<sup>34</sup> Chu's discussion leads to a remarkable prediction. In order for there to be a unique structure to the transverse ionizing shock the electric field upstream of the shock cannot be arbitrary, as has been assumed throughout this discussion, but must be altered to some predictable value by the emission of an electromagnetic wave from the shock front. It has not been established that this result is carried over intact to the case of the normal ionizing shock but there is every indication that it is. Verification of this point awaits further experimental studies.

Though not complete, an interesting discussion can be advanced to argue for the inadmissibility of all  $\tilde{E} > 0$  solutions in the region  $\tilde{u}_2 > 1$ , for the case of the normal ionizing shock. Returning to  $B^4$ , we solve for  $w_2$  and substitute in (12) to get;

$$E_Y = \frac{\mu H_{z2}}{u_2} (u_2^2 - b_{x2}^2) = \frac{\mu H_{z2} b^2}{v_2} (\tilde{u}_2^2 - 1). \quad (14)$$

For convenience, let us assume the geometry of Fig. 1. (The argument is identical for any coordinate system.) Now  $\mu$  and  $b_{x2}^2$  are always  $> 0$ ;  $\tilde{u}_2 > 1$  by hypothesis; and  $u_2 > 0$  for the geometry chosen, all of which implies that  $E_Y$  and  $H_{z2}$  are always of the same sign. But this would seem impossible for the following reason. Since  $E_Y$  is continuous across the

shock we expect, if we believe  $\vec{j} = \sigma\vec{E}$ , to have  $\vec{j}$  parallel to  $\vec{E}$ . But this  $\vec{j}$  will give rise to an  $H_{z2}$  in the  $-z$  direction contrary to the statement  $H_{z2}$  must be greater than 0. Taussig includes in his report a proof by C.K. Chu that attempts to substantiate that these shocks have no structure and therefore probably do not exist. From such arguments we are led to the possibility that only  $\vec{E} = 0$  solutions propagate steadily for  $\tilde{u}_2 > 1$ . Since the method by which ionizing shocks are initiated would seem to preclude the possibility of having  $\vec{E} = 0$  ahead of the wave (see Sec. 3.1) the question arises, how does the wave adjust to the  $\vec{E} = 0$  requirement. Possibly the electromagnetic wave postulated by Chu is emitted from the shock with just sufficient strength to completely cancel the nonzero electric field ahead of the shock. The answer to this question can only be provided by experiment. In the next chapter we will show preliminary evidence that points to the existence of  $\vec{E} > 0$  solutions in apparent disagreement with the above inadmissibility argument.

To complete the theoretical basis for an experimental study of normal ionizing shocks in hydrogen, Taussig has extended his original work to include dissociation and ionization across the shock front.<sup>25</sup> His work provides a computer program whereby, if one specifies all upstream variables including shock speed, gas composition, electric field and normal magnetic field, then the downstream state is determined, complete with percentage dissociation, percentage ionization, temperature, etc. In addition, following Kemp and Petschek exactly, he includes integration through the rarefaction fan that follows the shock. Thus, a complete theory of ionizing shock properties including chemistry, and within the context of a laboratory situation, is available. For our work, such

a refined theory is not necessary. The effects of chemistry serve only to modify slightly the non-chemistry calculations. No new wave solutions result from inclusion of equilibrium chemistry, and hence such effects will be important only when the downstream variables can be measured to within a few percent. However, it is not appropriate to neglect the fact that if one deals experimentally with hydrogen (as we do), and if one ionizes the hydrogen, there is a transition from diatomic to monatomic gas. In such a transition,  $\gamma$  changes from about 1.40 to 1.67. This effect was not included in the theory just presented. There,  $\gamma$  was assumed constant. If one does include the jump in  $\gamma$  in the jump Eq. B5', the form and all the features of the solutions remain as we have discussed them - only the numbers change. All subsequent work in this report is matched to the theory presented in this chapter with the added stipulation that there be a jump in  $\gamma$ , across the shock, from 1.40 to 1.67.

### 2.2.2 Experiments

From an experimental viewpoint, ionizing shock studies must be preliminary to any studies of classical mhd shocks. This is a point that has been too often overlooked. It is only within the last two years that serious work has begun on producing and understanding ionizing shocks. The first such studies were reported in 1963 and 1964 by Watson-Munro et al at the University of Sydney in Australia.<sup>36, 37, 38</sup> They concentrated on verifying the theoretical results of Gross and Kunkel,<sup>10</sup> which at that time was the only available theoretical study of the jump properties of ionizing fronts. The Sydney group succeeded in verifying the wave speed predictions of Kunkel and Gross.

At about the same time Vlasses reported on ionizing shocks produced in an inverse pinch experiment.<sup>39, 40</sup> His work, though mostly qualitative, was important in that he recognized the essential differences between ionizing waves, ordinary gas shocks and mhd shocks. In mid-1965 Patrick and Pugh,<sup>41</sup> reporting on their work with ionizing fronts, report evidence of an N type ionizing front in a coaxial electromagnetic shock tube. However, their experiment was performed with initial magnetic fields in the plane of the shock front rather than normal to it.

The works just discussed represent, to the author's knowledge, all the experiments conducted specifically to study the mechanics of mhd ionizing shock fronts. All have been mainly concerned with measuring wave speeds and mapping out device operation and none has been significantly extended beyond that. In the next chapter an experiment is described for which

the experimental evidence fits a simple explanation of ionizing shock behavior. The proposal that is advanced and verified is inductively constructed from the theory of normal ionizing shocks just presented, from experimental evidence obtained, and from analogy with classical gas dynamic phenomena. We will see that the complete range of shock velocities can be mapped by a single curve that has strong intuitive support. Further, the experiment verifies two of the most unusual aspects of the ionizing shock front - the appearance of the switch-on shock and the extension of the switch-on shock to the slow shock regime.

### 3. AN EXPERIMENT TO VERIFY THE THEORY OF NORMAL IONIZING SHOCKS

#### 3.1 Apparatus

##### 3.1.0 Introduction

An experimental verification of the normal ionizing shock theory presented in 2.2.1 requires a device capable of generating an essentially one-dimensional shock, propagating through hydrogen, whose velocity lies in the range  $10^6$  to greater than  $10^7$  cm/sec. In this range a hydrogen plasma can be produced with any desired degree of dissociation and/or ionization.

Attempts to attain such experimental conditions have been made with conventional pressure driven shock tubes. However, with these devices there is an upper limit of about 2 e.v. for the temperature that can be produced in the shocked gas. A device that seems to hold great promise as a research tool in the area of strong ionizing shocks is the coaxial electromagnetic shock tube. The basic principle of its operation is simple. One discharges a large amount of current from one electrode to an adjacent electrode, and the self-induced magnetic field is used to propel this current into a cold, low-pressure gas region. The coaxial geometry requires that the discharge be across the annulus between cylinders and so, if the return ground is carefully arranged, a toroidal current flow configuration is formed, and all the self-induced magnetic field is confined within it. The Lorentz force on the free-surface of the current flow propels that

surface down the region between the cylinders. This mechanism is analogous to forcing a piston into a cylinder and, like its mechanical counterpart, it sets up a shock that propagates ahead of it. Since the "piston" can be driven very fast, the shock that travels ahead of it can generate a very high temperature plasma (see Fig. 4 ).

The experimental apparatus consists of:

- 1.) a one meter long, seven-centimeter mean diameter coaxial shock tube with a one-centimeter annulus;
- 2.) a solenoidal magnet capable of generating longitudinal d.c. magnetic fields from 500 gauss to 13.8 kilogauss;
- 3.) a 40,000 joule capacitor bank designed to deliver a trapezoidal, 14 $\mu$ s pulse of 150,000 amperes into .2 ohm load;
- 4.) an air-gap switch for switching the bank into the shock tube;
- 5.) instrumentation to measure shock speeds, induced magnetic fields, and electric fields;
- 6.) control circuitry for firing the shock tube and timing the diagnostic devices.

### 3.1.1 The Shock Tube

The shock tube is basically a simple device consisting of a three inch i.d. stainless steel cylinder, one meter long. An inner aluminum cylinder of 2 $\frac{1}{4}$  inches o.d. is mounted coaxial with the stainless outer one. One end of the inner cylinder is provided with a copper knife-edge so that a preferred breakdown path is provided when the capacitor bank

voltage is applied between the inner and outer cylinders. The knife-edge is mounted on a  $\frac{1}{2}$  inch copper rod that feeds through a plexi-glass end piece to one end of the air-gap switch (see Fig. 5 ). The air-gap switch then connects to the high voltage side of the capacitor bank.

The knife-edge is positioned on the inner conductor so that after assembly inside the solenoidal magnet it is in a homogeneous region of the magnetic field (see Fig. 6 ). In addition, to provide a well-defined boundary, from which the shock wave is launched, a flat glass plate is positioned just behind the knife edge (see Fig. 7 ). It was found necessary to insulate the copper feed, and the last 9 inches of the inner cylinder, lest the discharge be initiated there instead of at the knife edge. Those areas were wound with thin nylon strips and teflon tape, epoxied to the metal to insure a homogeneous seal.

To provide an experimental situation where one can vary the pressure of the pre-shocked gas in the shock tube a Cen-co type VMF 20, 20 l/s diffusion pump, backed by a Welch 2 CFM fore-pump is attached to the shock tube. This system gives a base pressure of approximately  $10\mu$  of mercury in the working region. This relatively high base pressure would seem to indicate a sizable leak in the system, but leak testing with a mass-spectrometer proved otherwise. The glass backup plate behind the knife edge so throttles pump-out that although a base pressure of  $5 \times 10^{-5}$  mm of mercury is obtained near the pump-out port, the vacuum system cannot reduce, in any reasonable time, the base pressure in the working area. The base pressure near the pump-out port is measured by a Veeco Cold Cathode Discharge Gauge while the pressure in the working region is monitored by a Veeco Thermocouple Gauge

attached to the far end of the shock tube. The thermocouple gauge is particularly useful because the system is generally filled with cold hydrogen to about 200 $\mu$  of mercury, and the thermocouple gauge can measure this quite easily.

The working length of the shock tube is approximately 75 centimeters long, and consists of that portion of the shock tube that is in a relatively homogeneous region of the longitudinal magnetic field (see Fig. 6 ).

### 3.1.2 The Magnetic Field

The magnetic field is provided by 36, 1.1" wide water-cooled, copper pancakes potted in epoxy. Designed by the Matterhorn thermonuclear group at Princeton University, these coils are structurally able to withstand peak fields of 50 kilogauss. They produce fields homogeneous to  $\pm .16\%$  over the central 25 cm inches, and  $\pm 1\%$  over the central 33 cms. A computer program, written at Columbia, was used to calculate the field produced. Fig. ( 6 ) shows the computer calculation of the axial and radial fields as a function of magnet length. Knife-edge position and shock tube working length are also indicated. The axial field was measured using a hall probe gauss-meter and agreement with the theoretical field strength was at least as good as the gauss meter accuracy of  $\pm 1\%$ .

The magnet is powered by a 200 kilowatt, three-phase, rectifier with less than 1% peak to peak ripple. The rectifier was designed for 10-second operation at 300% overload and in this mode of operation can deliver 2200 amperes. This enables the magnet to provide longitudinal field continuously variable from about 500 gauss to almost 13.8 kilogauss.

### 3.1.3 The Capacitor Bank

A shaped-pulse, 40,000 joule capacitor bank provides the energy to drive the "magnetic" piston in the shock tube. The bank consists of a total of 18 capacitors arranged in four parallel impedance meshes. Each mesh is equivalent to a capacitor and a series inductor. This particular configuration, called a Guillemin Type C network, was chosen because of design simplicity, ease of assembly and shaped-pulse capability. Fig. ( 8 ) is a schematic of the bank, and gives all the pertinent design facts. When charged to 50,000 volts, the bank is designed to deliver a 1.0  $\mu$ s rise-time pulse of 150,000 amperes into a matched load of .2 ohms for approximately 14 microseconds. However, any external inductance in the load badly degrades the ideal pulse shape. In practice we get a pulse shape more nearly sinusoidal. Figure ( 9 ) is a typical current pulse trace. Appendix (A) has been included to present a more detailed discussion of the theory behind all shaped-pulse capacitor banks, and to explain the motivation behind the Type C network.

The capacitor bank is charged to its operating voltage by a Del Electronics (TC series) 80kV, 5ma power supply. This power supply has been provided with automatic shutoffs to prevent overcharging the 50kV capacitors, and equipped with a special dump tank that will discharge the fully charged bank in under 10 seconds.

The capacitor bank is housed inside a sturdy, shielded, solid wooden enclosure (Fig. 10). The output end of the bank is a parallel plate transmission line whose high-voltage side is connected to an air gap switch.

### 3.1.4 Air-Gap Switch

The air-gap switch separates the capacitor bank from the  $\frac{1}{2}$ " copper feed-through attached to the knife-edge on the inner cylinder of the shock tube. The switch is most easily described by referring to Fig. (11). The solid brass anode attached to the charged capacitor bank is a flattened hemisphere adjusted to a distance,  $d$ , from the stainless steel cathode that is sufficient to hold off the capacitor bank voltage. It is important to note that some d.c. path must be established from cathode to ground or else the bank voltage divides across both switch and shock tube; making it difficult to fire the switch. This can be accomplished either by connecting a large ( $\sim 10$  Megohm) resistor between cathode and ground or by pre-ionization in the shock tube. The latter method is the one presently being employed because it serves a dual purpose. Discussion of this is deferred until later.

The switch is fired by establishing a secondary breakdown between the isolated teaser electrode and the cathode. The shock formed at this secondary breakdown carries ions and electrons to the anode and establishes a low impedance path between anode and cathode. The capacitor bank voltage now appears at the knife-edge on the inner conductor and electrical breakdown occurs there as desired.

The teaser circuit consists of a 10 kilovolt; .125  $\mu$ f capacitor charged by a 30 kilovolt, 5 ma supply through a charging resistor. A 25 kilovolt ignition switch holds the voltage until firing is desired. When the switch is to be

fired, a 1500 volt pulse is supplied through the pulse transformer between ignitor and cathode of the ignitron. The ignitron breaks down, the teaser rises to 10 kilovolts, the teaser breaks down to the cathode, and the anode then breaks down to the cathode. Figure ( 12 ) shows the air-gap switch in normal operating position.

Probably the most important and most difficult technical aspect of coaxial shock tube technology is to insure that after one fires the capacitor bank the discharge at the knife-edge on the inner conductor is uniform around the entire knife-edge. Only then can one produce the "magnetic" piston geometry which is the key to the production of strong ionizing shocks.

The method finally decided upon in this experiment was utilization of the strong, external, longitudinal magnetic field, and r.f. pre-ionization confined to the immediate neighborhood of the knife-edge.

### 3.1.5 Pre-ionization: Circuitry and Technique

A 30 Mc/sec, 150 watt, push-pull, tuned grid, tuned-plate oscillator was designed and built to couple symmetrically to the region around the knife-edge. Figure ( 13 ) gives the oscillator schematic and a detail of the coupling arrangement. Localized breakdown was initiated in hydrogen at a pressure of 200 microns of mercury by imposing a longitudinal magnetic field of greater than about 800 gauss, and then pulsing the oscillator into operation at about 1000 volts and 100 ma. After r.f. breakdown occurs the oscillator level is reduced to approximately 300 volts and 10 to 15 ma. The application

of the longitudinal magnetic field (i.e., the crossed-field configuration) was found necessary in producing uniform r.f. breakdown. Once uniform r.f. breakdown has been obtained, the main bank discharge can be initiated and it breaks down uniformly around the knife-edge.

Recalling the need for a d.c. path from air gap switch cathode to ground (Sec. 3.1.4), it is obvious that the pre-ionizer performs this service admirably.

### 3.1.6 Control Circuitry

The entire experiment is controlled from a single panel where one push button can fire the entire apparatus and initiate all necessary timing circuits. The basic timing circuit is a Pegram Electronics Laboratory Dual-Delay Module which is, simply, a variable positive or negative square pulse generator. Each unit triggers only from a negative going pulse, and this feature enables one to set up any number of separate pulses of either polarity. For example, trigger one unit and obtain a positive square pulse of duration  $\tau$  seconds. Feed this into the trigger of the second unit, and since this second unit only triggers on negative going pulses it will not trigger until the trailing edge of the first pulse arrives. Thus the second unit does not fire until  $\tau$  seconds after the first; at which time it produces an independent pulse of either polarity with any pre-set duration. Series operation in this manner with several modules thus allows the establishment of a well-defined time base with pulses at any given point after  $t = 0$ . The  $t = 0$  point is established from a simple blocking oscillator pulser which

provides a negative signal sufficient to trigger the first dual-delay module. Associated with the timing circuit are two high voltage pulsers. One is a fixed duration, transistorized pulser capable of delivering a .2 microsecond, 600 volt pulse into 30 feet of open circuited 50 ohm cable. The other is a thyatron circuit which discharges a 1500 volt capacitor into the 1:1 transformer in the air-gap switch circuit (Fig. 10).

### 3.1.7 Operation

The operation of the shock tube consists of leaking ultra-pure hydrogen into the annulus through a variable leak (see Fig. 5 ) until the desired operating pressure is obtained as monitored on the thermocouple gauge (Fig. 5 ). The magnetic field is then set at the desired value and pre-ionization established about the knife-edge. It has been observed that for reproduceable operation of the shock tube it is necessary that once pre-ionization has been effected, the power level into the r.f. oscillator be reduced to a minimum consistent with uniform pre-ionization (usually this is of the order of 3-5 watts plate power, whereas breakdown usually requires about 150 watts).

The capacitor bank is charged to the voltage that will give the desired drive current and the shock tube is then ready for firing. The firing sequence is initiated by a push button on the blocking oscillator circuit that produces a negative pulse. This pulse fires the first dual-delay module. The output from this module then triggers all the oscilloscope time bases so that a common time base is established. This first pulse also fires a second module whose output

triggers the 600 volt, fixed duration, high voltage pulser. Its 600 volt pulse is delivered to the the thyratron pulser, triggers it, and the thyratron output triggers the ignitron in the teaser circuit of the air-gap switch. The air-gap switch fires and the bank is discharged through the shock tube. After firing the system is flushed and made ready for another shot. The entire timing sequence is indicated in Fig. (14 ).

## 3.2 Shock Tube Instrumentation

### 3.2.0 Introduction

Shock tube instrumentation consists of; 1) a simple magnetic pickup coil for measuring total drive current delivered by the capacitor bank; 2) photomultipliers and associated circuitry for monitoring the velocity of the luminous ionizing front; 3) magnetic field probes for detecting the self-induced field in and behind the ionizing front; and 4) electric field probes for measuring the electric field ahead of and behind the shock.

#### 3.2.1 Current Monitoring Loop

The instantaneous current being delivered by the capacitor bank is determined by integrating the EMF ( $t$ ) observed between the terminals of a coil due to the change in flux produced by the time-varying current.

A single, square loop, carefully shielded, is positioned along the main feed into the shock tube. Its terminals are connected to a 50 ohm cable which is terminated in a 50 ohm, 10:1 attenuator. The output voltage is fed into a Tektronix, Type "0" Operational Amplifier plug-in unit operating as an integrating circuit. The output of the operational integrator is  $I(t)$  and is displayed directly on the scope. Figs. (15) and (16) show the loop, its construction, its position on the main current feed and the circuit used to measure  $I(t)$ . The theory of the probe is presented in Appendix B.

### 3.2.2 Photomultipliers and Associated Circuitry

Photomultipliers are used to monitor the light output from the shock tube at several different ports along the shock tube length. Light is delivered to a photomultiplier through a fiber optic light pipe. The light pipe is connected to a reflector mounted above a 1/16" hole drilled through the shock tube wall. Port details are shown in Fig. (17b). Figure (17a) shows a photomultiplier port in relation to the entire shock tube assembly.

RCA 931A photomultipliers were used with standard resistive divider networks to provide voltage to the 10 stages. The last few stages are provided with parallel capacitors to enhance the pulse response of the tubes.

The output of each photomultiplier is connected to an emitter-follower circuit which is capable of driving the terminated 50 ohm cable that brings the signal to an oscilloscope. Figure (18) is the complete photomultiplier circuit.

### 3.2.3 Magnetic Field Probes

The theory of ionizing shocks distinguishes three regions of interest differentiated by the value of the Alfvénic Mach Number,  $M_a$ . In the sub-Alfvénic region ( $M_a < 1$ ) and the trans-Alfvénic region ( $1 \leq M_a < \sim 2$ ) the drive current divides between the shock front and the current carrying rarefaction fan. In the super-Alfvénic region ( $M_a > \sim 2$ ) the drive current may or may not be completely confined to the rarefaction fan, depending upon whether or not all the  $\tilde{E} > 0$  solutions are inadmissible. Therefore, the sub-Alfvénic and trans-Alfvénic regions will exhibit switch-on behavior while for a super-Alfvénic wave we have no definite theoretical prediction.

It is apparent that measurement of the self-induced magnetic field holds the key to determination of switch-on like ionizing shocks. In the switch-on regime the magnetic field profile rises through the shock, remains constant in the post-shock gas, and then rises to a final value through the rarefaction fan. In the super-Alfvenic region, the magnetic field profile can give the dramatic evidence of separation of shock front and drive current that is necessary to support or disprove the argument about inadmissibility.

A complete theory of the measurement of self-induced magnetic fields in plasmas will be deferred to the next chapter and to an appendix. The probe is designed to utilize Faraday's law and hence, it consists of a number of turns of carefully insulated wire wound into a coil of known dimensions. The EMF generated by the sweeping of the magnetic field past the probe is monitored on an oscilloscope and is directly related to the magnetic field profile.

Since in cylindrical geometry the self-induced field is confined to the azimuthal or  $\theta$  direction, the probe must be inserted so that its surface lies in the  $\rho$ - $z$  plane (see Figs. 19 and 27). Figures 19 and 20 are, respectively, a schematic of the probe and probe circuit; and a photograph of an actual  $B_\theta$  probe (so-called from here on because it detects the magnetic field in the  $\theta$  direction).

The pulse transformer is used so that both ends of the probe may float. If one end were grounded breakdown might occur from the inner cylinder to the probe. The relatively large size of the probe and the square shape are the result of the probe theory presented in Appendix C.

### 3.2.4 Electric Field Probes

As discussed in Chapter 2, the radial electric field ahead of the shock is an important parameter in the theory of ionizing waves. Attempts were made to measure this electric field both ahead of and behind the shock front. Limited success was obtained in the latter case using a probe very similar to the  $B\theta$  probe. The idea is to insert two bare wires into the conducting flow and measure the potential difference between them. Ideally this is possible because in the shock front and post-shock gas the conductivity is very high and therefore, in the presence of an electric field the probe will draw a small amount of current and act, essentially, as a voltmeter.

The probe construction is shown in Fig. 21. The external circuitry is identical to the  $B\theta$  probe (i.e., the Cannon connector goes to a 5:1 pulse transformer and then into a length of 50 ohm cable terminated at an oscilloscope).

Measurement of the electric field ahead of the shock front, i.e., in the cold, pre-shock gas, was attempted by connecting a very high impedance voltage divider between inner and outer conductor and trying to measure the potential drop between them. As simple as this may sound, the problems are very complex. First, the voltage divider must be a very high impedance one to preclude any loading of the shock tube. Second, since, before breakdown, the total bank voltage appears between the cylinders, the voltage divider must be able to withstand upwards of 50,000 volts and also reduce this 50,000 volts to manageable proportions. (The divider must divide a few hundred to one, at least.) Third, since the maximum expected electric field after breakdown is only of the order of a

few tens of volts per centimeter, the divider, from the second consideration, reduces this to a very low level. Fourth, noise considerations require that all measurements be done in a screen room 20 to 30 feet from the shock tube. Hence, the voltage divider must feed a cathode-follower which can drive terminated 50 ohm cable without too much rise time degradation or loss of signal strength.

However, even after recognizing the problems, the actual measurement indicates what appears to be an excessively large potential in comparison with predictions from the theory and from results of bare wire probes. The source of this disparity is, as yet, not understood.

### 3.3 Data and Error Analysis

#### 3.3.0 Introduction

For a given axial magnetic field and pre-shock pressure, comparison with the theory presented in 2.2.1 requires the simultaneous measurement, at a specific distance from the knife-edge, of the shock velocity; the instantaneous total current delivered to the shock tube; the self-induced magnetic field, in the  $\theta$  direction, both behind the shock and behind the rarefaction fan that follows the shock; the length of the homogeneous gas sample between the shock and rarefaction fan; and the electric field ahead of and/or behind the shock.

The first two of these quantities are separately measured. The next three are all determined from  $B_{\theta}$  measurements (see Sec. 3.2.3), and the last is obtained from the electric field probe (see Sec. 3.2.4).

#### 3.3.1 Shock Velocity Measurement

Photomultiplier outputs were monitored at the 20, 25, 35, 50 and 75 centimeter ports along the shock tube length. For a specific initial pressure, longitudinal field, and capacitor bank voltage, the outputs were recorded on Polaroid film and analyzed in the following manner. The photomultiplier trace at each port was magnified and projected, using an overhead projector with pre-set magnification, onto a single sheet of graph paper. In this way all five ports could be presented on a single time base for easy examination. The time of arrival of the first luminous front at each port was

measured and recorded. Time zero was determined by projecting the current trace onto the same display and using the instant when current first began to flow as the  $t = 0$  point. For each set of initial conditions the shock tube was fired an average of 12 times. The arrival times at each port were tabulated and plotted on an  $x-t$  diagram and a curve was fitted to the data. The slope of the curve at any point gives the average shock velocity at that point. Figure 22 is one such typical  $x-t$  diagram. Data is best fitted by the heavy straight line drawn through the points, while the two dotted lines indicate the "steepest" and "least steep" curves that can be sensibly drawn through the data. The shock velocity is calculated as  $6.70 \times 10^6 \pm 10\%$  cm/sec, and the error is assigned by measuring the slope of the two dotted curves. This is the procedure that was followed in each series of shots and results similar to Fig. 22 were always obtained, i.e., between 20 and 75 centimeters the shock front was propagating steadily. (Though we are not sure the luminous front is coincident with the shock front, the fact that the velocity of the luminous front is steady enables us to use that velocity as the shock velocity.) In all cases the error was no more than  $\pm 12\%$  and no less than  $\pm 8\%$ . For ease in subsequent calculations,  $\pm 10\%$  has been accorded each velocity measurement. Figure 23(a) is a typical set of photomultiplier traces for a given set of conditions. Figure 23(b) shows a set of traces projected, with the current trace, onto a common time base.

Table I gives the experimentally measured shock velocity for the series of runs used as a basis for this experimental study. Note that the series covers the sub-Alfvenic, trans-Alfvenic, and super-Alfvenic regions. The ordinary sonic Mach number,  $M$ , has been included to give some perspective to the numbers.

### 3.3.2 Instantaneous Current Measurement

The instantaneous current monitored by the current monitoring loop (see Sec. 3.2.1) is displayed on an oscilloscope face and recorded on Polaroid film. As mentioned above, it is projected onto the common time base used for the shock velocity study. This serves a dual purpose. Not only does it immediately provide a time zero point for shock arrival measurements, but further one can easily determine the total amount of current flowing through the shock tube at the time the shock reaches any specific point. Since all magnetic probe studies (see Sec. 3.3.3) were conducted at the 45 centimeter point, all the current calculations, now to be discussed, give the total current through the shock tube for that instant when the shock had traversed 45 centimeters.

From the  $x-t$  diagram for a specific run (consisting of an average of 12 shots) the most probable arrival time of the shock at 45 centimeters is determined. Using this time the amplitude of each individual current trace, at that time, is tabulated and averaged. With the known conversion factor discussed in Appendix B, the average instantaneous current flowing through the shock tube is determined.

Table II gives the instantaneous current measured for the runs listed in Table I. The error associated with each measurement is a compromise between the square root of the sum of the squares of the individual errors involved in reading a value for  $I(t)$  from a single scope trace of finite thickness, and a standard deviation analysis, based on the average of all the shots, which gives a somewhat more precise value. The need for compromising lies in recognizing that the current measurement ultimately depends on exactly how the

probe is sitting at a given time, how well the capacitor bank voltage can be set and reset from shot to shot, and other conditions not amenable to conventional error and analysis.

Figure 9 shows a typical current trace obtained from the capacitor bank. One might argue that its shape leaves much to be desired, since it is not the desired square current pulse. In fact, however, the ultimate criterion for any current pulse shape in an electromagnetic shock tube is whether or not it gives steady shock propagation. Since this criterion is experimentally well established in our device little effort was made to improve the pulse shape.

### 3.3.3 Measurement of Switch-on and Drive Magnetic Field

In this section we turn our attention to the problem of measuring and mapping the self-induced magnetic field produced by the instantaneous current flowing through the electromagnetic shock tube. The field has two distinct components, each of which must be measured. The first is the "switch-on" field discussed in detail in Sec. 2.2.1. It is the magnetic field, predicted from an analysis of the ionizing shock jump conditions, that appears, in the  $\theta$  direction, directly behind the shock and results from some fraction of the total instantaneous current flowing through the shock itself. The second is the "drive" magnetic field that results because the remainder of the instantaneous current must flow through a simple, centered rarefaction fan, i.e. an expansive wave, traveling behind the shock. The rarefaction fan is not an intimate part of the problem of solving the jump equations, but rather it arises from the initial and boundary value problem associ-

ated with the coaxial electromagnetic shock tube. The rarefaction fan is needed to slow the gas down behind the shock so that it meets the boundary restriction of zero normal velocity at the end wall. (Actually, from a mathematical viewpoint one can have either zero normal velocity or a perfect vacuum at the end wall, but the former is probably the more realistic.)

The mechanics of coupling the simple, centered rarefaction fan to the shock jump problem and to the boundary conditions imposed by the device are best explained in Ref. 29 and 33. The former treats the problem for "classical" mhd shocks in a coaxial electromagnetic shock tube and the latter extends the analysis to the normal ionizing shock situation. Here it will be sufficient to note that across a rarefaction fan all fluid variables change continuously, as opposed to a shock wave where one assumes a finite jump in the fluid variables. The leading edge of the rarefaction fan propagates into the gas behind the shock at the characteristic velocity associated with that gas. If one plots one of the variables behind the shock, e.g. pressure, at a given time, as a function of distance, the profile appears as in Fig. 24(a). The  $x-t$  diagram for such a situation is shown in 24(b), the relation between 24(a) and 24(b) being obvious. In the same situation we may ask for the current and magnetic field distribution through shock and rarefaction fan. The qualitative features associated with each of these quantities is shown in Fig. 25, (b) and (c). Figure 25(a) is an  $x-t$  diagram showing a shock of finite thickness and relates 25(b and c) to a specific shock tube situation. Note that the total current divides between the shock and the rarefaction fan and that no current flows in region 1 ahead of the shock, or in region 2 behind

the shock, or in region 4 behind the rarefaction fan. As a result, the magnetic field in the azimuthal direction rises from zero in region 1 to a constant value in region 2, the switch-on field, hereafter denoted by  $B_{\theta}(SW)$ , and then rises again through the rarefaction fan, region 3, to a final value, the so-called drive field value, hereafter denoted by  $B_{\theta}(Drive)$ . It is this behavior of  $B_{\theta}$  that we will try and verify by analyzing the output of a  $B_{\theta}$  probe (see Sec. 3.2.3) located at the 45 centimeter position.

In Appendix C a detailed analysis of the method used in obtaining  $B_{\theta}$  from the observed EMF is presented. We will use the results of that analysis for the specific probes discussed in Sec. 3.2.3. However, a few words of introduction are in order. The essence of the discussion in Appendix C is that a large area probe can be effectively utilized for the point measurement of magnetic fields in moving media, for the case in which the field variation is known in two spatial directions and unknown in the third. For an infinitely large probe (effectively, large compared to any spatial changes in the magnetic field) the probe is equivalent to a single length of conductor along a direction of known field variation. If a magnetic field is moving across the probe, the potential difference, or the EMF, between the ends of the conductor is  $(\vec{V} \times \vec{B})l$  where  $\vec{V}$  is the velocity of the moving field with respect to the probe,  $\vec{B}$  is the magnetic field and  $l$  is the length of the conductor. The EMF is, then, proportional to  $\vec{B}$  directly and not to  $\frac{\partial B}{\partial t}$  as is often mistakenly adduced from a cursory examination of Faraday's law. For a finite sized probe the determination of  $\vec{B}$  from the observed EMF involves the use of a simple recursion formula developed in Appendix C, Eq. C15. An example of the use of that equation will now be reviewed.

Assume the geometry depicted in Fig. C1, Appendix C, and assume that the EMF ( $t$ ) observed between the terminals a and b of the probe is the heavy curve drawn in Fig. 26. For a given shock velocity  $U$  and a probe dimension,  $m$ , in the  $x$  direction, a recursion time,  $\tau_r$ , is defined:  $\tau_r \equiv \frac{m}{U}$ . Assume  $U$  and  $m$  such that  $\tau_r$  coincides with five divisions on the time scale in Fig. 26. The recursion formula says one must do the following. For  $0 < t \leq \tau_r$ ,  $B_\theta$  is identical to the EMF. For  $\tau_r < t \leq 2\tau_r$ , and in particular for point 6,  $B_\theta = [\text{EMF (at point 6)} + \text{EMF (at point 1)}]$ , where the proportionality constant is determined from the probe dimensions and the shock velocity. For  $2\tau_r < t \leq 3\tau_r$ , and in particular for point 11,  $B_\theta = [\text{EMF (at point 11)} + \text{EMF (at point 6)} + \text{EMF (at point 1)}]$ . In this way,  $B_\theta$  is mapped out point by point directly from the EMF observed. The circled points plotted above the EMF curve represent the  $B_\theta$  derived from the EMF for times  $t > \tau_r$ . The complete  $B_\theta$  map consists of the EMF trace from  $0 \rightarrow \tau_r$  and continues smoothly through the circled points. The EMF shown was constructed to produce a  $B_\theta$  such as would be produced by the electromagnetic shock tube and shows all the features we have discussed. To convert the  $B_\theta$ , derived as a function of laboratory time, to  $B_\theta$  as a function of its own spatial coordinate one need only multiply the times observed by the shock velocity  $U$ . One further point must be mentioned. From a purist's point of view, use of the recursion formula through the rarefaction fan is not justified. Why it is not is explained fully in Appendix C. However, for any of the experiments performed here the correction to the recursion formula is quite small so that in all actual cases, described below, as well as the example just discussed, the recursion formula was used to calculate  $B_\theta(\text{SW})$  and  $B_\theta(\text{Drive})$ . The advantage in the method just out-

lined is that, in principle, since it only involves counting, the frequency bandwidth of the measuring system is infinite. Further, of course, it eliminates any difficulties that develop from time integration of the EMF.

We now direct ourselves to the actual experimental situation. The probe used to detect the self-induced magnetic field consists of ten turns of carefully wound Formvar wire. The entire coil is inserted in the annulus of the shock tube and the output is coupled through a nominally 5:1 pulse transformer to a terminated 50 ohm cable (see Fig. 19). The exact probe geometry, size and position is shown in Fig. 27.

Equation C15 of Appendix C states that the proportionality factor between  $B_{\theta}$  and the EMF is just  $\frac{-1}{U\ell}$  where  $U$  is the shock velocity and  $\ell$  is the probe dimension in the radial direction. The derivation, however, assumes no variation of  $B_{\theta}$  in that direction. In the coaxial electromagnetic shock tube the field obviously varies as  $\frac{1}{r}$  and this can be simply introduced into Eq. C15 by replacing  $\ell$  by  $(\ln \frac{\rho_2}{\rho_1})\rho_{\text{mean}}$  (see Fig. 25). The proportionality constant then becomes  $^{-1}/U(\ln \frac{\rho_2}{\rho_1})\rho_{\text{mean}}$  and for the probe shown in Fig. 27 we get  $^{-1}/U(.00163)$ . Equation C15 for such a one turn probe becomes;

$$B_{\theta}(45, \rho_{\text{mean}}, t) \left[ \frac{\text{webers}}{\text{m}^2} \right] = \frac{-1}{U(.00163)} \sum \text{EMF}^* \quad (15)$$

where  $B_{\theta}(45, \rho_{\text{mean}}, t) \equiv$  the self-induced magnetic field in the  $\theta$  direction at time,  $t$ , at the axial position 45 centimeters from the knife-edge, and at the radial position,  $\rho_{\text{mean}}$  from the shock tube center line.

\* The summation term has been left purposely vague. Refer to Appendix C, Eq. C15 for its complete form.

For a ten turn probe and a pulse transformer whose transformer ratio is exactly 1:5.2, the relationship between the EMF observed across the terminated 50 ohm cable, called  $e_{out}$  in Fig. 19, and  $B_{\theta}(45, \rho_{mean}, t)$  becomes:

$$B_{\theta}(45, \rho_{mean}, t) = \frac{.52}{U(.00163)} \sum e_{out} \quad \text{or}$$

$$B_{\theta}(45, \rho_{mean}, t) \left[ \frac{\text{webers}}{\text{m}^2} \right] = \frac{3.19(10^2)}{U \left[ \frac{\text{m}}{\text{s}} \right]} \sum e_{out} \quad (16)$$

This is the formula used in all subsequent calculations.

For each shock tube firing the output of the  $B_{\theta}$  probe was monitored at the 45 centimeter point. The polaroid record was projected onto graph paper just as were the current and photomultiplier tracers. Each trace was reduced using the analysis described above. The values of  $B_{\theta}(SW)$ , and  $B_{\theta}(Drive)$ , and the length of the homogeneous gas sample were recorded. All shots at the same set of initial conditions, comprising a run, as listed in Tables I and II, were then tabulated and averaged to give an average  $B_{\theta}(SW)$ ,  $B_{\theta}(Drive)$ , and homogeneous gas sample length. The results are listed in Table III. The table is self-explanatory except for the last column, labeled  $X_e/X_s$ . At any time,  $t$ , after  $t = 0$ ,  $X_e$  represents the distance from the knife-edge of the leading edge of the rarefaction fan, while  $X_s$  represents the distance from the knife-edge to the shock front (see Fig. 25(a)). As is obvious from Fig. 25 (a) both  $X_e$  and  $X_s$  depend linearly on  $t$  and therefore the ratio  $X_e/X_s$  is time independent and represents a convenient way of specifying the length of the homogeneous gas sample (hgs). At any axial position along

the shock tube length, the length of the hgs is just

$$X_s - X_e = X_s \left(1 - \frac{X_e}{X_s}\right) . \quad (17)$$

The error associated with each of the measurements tabulated in Table III will now be discussed in detail. Figures 28, 29 and 30 show three different, but representative,  $B_\theta$  traces. The top trace in each figure is the actual EMF obtained for the conditions noted, while the bottom trace represents an enlargement of the actual EMF and the  $B_\theta$  derived from that EMF (cf with Fig. 26). The three derived  $B_\theta$ 's show distinct similarities and distinct differences. For convenience, we will refer to them as Types 28, 29 and 30, respectively. All types show a characteristic oscillatory structure, albeit in 28, that structure is more pronounced than in the others. Types 28 and 29 both show a distinct 2-level structure, exactly as we expect for a switch-on shock followed by a rarefaction fan (cf Fig. 26). Type 29 has an unambiguous switch-on regime while the switch-on region in 28 is apparent, but not as dramatic. In 30 the switch-on region is not well formed. We believe the slope change in the trace is diffusion of the magnetic field through the region between the shock and rarefaction fan. The dotted lines in each figure represent the average value of the switch-on and drive magnetic field for that shot. At the present time, it is believed that the oscillatory structure of the traces not part of the physics, but rather the result of the electrical characteristics of the probe circuit. In fact, an investigation of the circuit points to the pulse transformer as the element in the system responsible for the oscillations. To see why this is believed to be the case consider

Fig. 31. The heavy line represents an actual EMF obtained in a typical shot. The dotted curve represents the magnetic field obtained from the EMF. We note the oscillatory structure. If, now, we draw a smooth, monotonic curve (the dashed curve) through the derived  $B_{\theta}$  and re-derive the EMF that would give this dashed curve, we get the dashed EMF curve. It is apparent that some of the structure necessary to smooth out the oscillations in the  $B_{\theta}$  derived from the experimental EMF has been suppressed. The pulse transformer's response, in fact, does fall off significantly at the frequencies represented by the suppressed structure and for this reason the oscillatory behavior of the derived magnetic field is not thought to be indicative of actual magnetic field structure in the plasma.

For a given series of shots the error in the measurement of an average  $B_{\theta}(\text{SW})$  or  $B_{\theta}(\text{Drive})$ , or  $X_e/X_s$  is a combination of two factors. The first is the natural scatter that would be obtained in any experiment. Thus, even if all the  $B_{\theta}(\text{SW})$ 's looked like 29 we would expect to see a variation in the measured level from shot to shot. This kind of variation can be accounted for by a calculation of the standard deviation of the average measurement. The second source of error is the error associated with the assignment of some value to an individual  $B_{\theta}(\text{SW})$  or  $B_{\theta}(\text{Drive})$  when it is of the type 28 or 30. If the oscillatory structure is large, there is a large error in each individual measurement. Since in any series of shots there were several of each of the three different types of trace, it was impossible, a priori, to establish either error as the dominant one. Hence, the following rule was followed. All the individual average  $B_{\theta}$  values (switch-on and drive) were tabulated for a given series and each individual value was accorded its own error to account

for the oscillatory structure. A final average value was calculated. A standard deviation analysis was performed for this average value and an error obtained. Further, the square root of the sum of the squares of the individual uncertainties was computed and compared with the standard deviation. The larger of these two values was taken as the error in the derived  $B_0$ . In the final computation of the error we must also take into account the uncertainty in the shock velocity since it appears in the final reduction of the EMF to  $B_0$  (see Eq. 16).

The assignment of an error to the  $X_e/X_s$  measurement was done only on the basis of a standard deviation analysis. Examination of Figs. 28 and 30 shows that it is difficult to assign a specific uncertainty to each individual measurement of the hgs. And, since for all the cases just discussed the standard deviation error turned out to be the largest, our neglect to perform an error analysis on the individual errors is justified. In addition, the length of each hgs was so small that the natural scatter resulted in a large percentage error in the computed value of  $X_e/X_s$ . This is apparent in the tabulated values presented in Table III and this fact relegates the parameter  $X_e/X_s$  to a somewhat secondary role in the experimental study.

### 3.3.4 Electric Field Measurements

As already noted in 3.2.4, only limited success was obtained in the measurement of the electric field behind the shock and almost no success in the measurement of the electric field ahead of the shock. The major problems encountered were inductive pick-up due to the large currents and short times of

the experiment, and to noise generated by the air-gap switch and firing circuitry. Similar problems have been encountered by other investigators.<sup>42</sup>

Various methods were employed to eliminate the noise on the probes, all without significant success. A new approach is being investigated at the present time. For the purposes of this study, however, measurements of the electric field must be considered as unavailable.

### 3.4 Comparison with Theory

The theory of ionizing shocks, presented in 2.2.1 leaves one question completely unanswered. In its simplest form, the question is, for any given ionizing shock velocity, subject to the boundary conditions imposed by an electromagnetic shock tube, is there a unique set of downstream variables consistent with ionizing shock theory? If we refer to Fig. 3 the question can be rephrased. For the electromagnetic shock tube, is there a unique locus of points over the range  $0 < \tilde{u}_1 < \infty$  that describes the propagation of ionizing shocks?

An affirmative answer will help resolve the puzzling question posed by the multiple contours characterizing ionizing shock theory, i.e. which  $E > 0$  solution, if any, is appropriate to a given shock velocity. This question was hinted at, indirectly, in a discussion of the stability and evolutionarity of the classical, slow mhd shock (see page 20). A single locus of solutions provides a natural path of behavior for all ionizing shocks. And, because of the general nature of ionizing shock theory, the possibility of such a locus has broad implications in the many physical situations in which ionizing shocks occur. For example, pinch and inverse pinch experiments are two areas of current investigation where ionizing shocks play an important role.

It will now be shown that the experimental results presented in 3.3 fit one such locus, and in addition, the locus has a distinct physical basis deeply rooted in the theory of classical gas dynamics.

The relation of ionizing shocks to classical mhd shocks is analogous to the relationship between detonation - deflagra-

tion phenomena and ordinary gas dynamic shock phenomena. In detonation - deflagration theory, the internal energy of the gas behind a reaction front (the detonation - deflagration analog of a shock) is different from that of the gas ahead of the reaction front. This difference in chemical composition across the front gives rise to the well known and well verified Chapman-Jouguet hypothesis.<sup>22</sup> The hypothesis states that the entropy of the downstream gas assumes a stationary value, in particular, a maximum (minimum) for an expansive (compressive) reaction; the gas behind the reaction front moves with the small disturbance speed in that gas; and the velocity of the reaction front with respect to the upstream gas also assumes a stationary value with a maximum (minimum) for an expansive (compressive) reaction. Further, the theory does allow expansive reactions, since this is precisely what is meant by a deflagration. In ionizing shock theory we have seen that the energy equation has an electric field contribution added to the upstream energy in direct analogy with detonation-deflagration theory. The effect of this addition is, of course, the theory developed by Taussig.

In the context of this discussion we expand our outline of that theory to include the following features. The locus of all end points of the  $\tilde{E} > 0$  contours has remarkable properties. For any end point of any contour, Taussig proves:

- (a) that the entropy of the downstream gas assumes a stationary value,
- (b) that the velocity of the downstream gas is precisely the slow disturbance speed in that gas, and
- (c) that the shock velocity also assumes a stationary value.

These statements lead to the conclusion that the locus of all contour end points is a locus of Chapman-Jouguet points, with

the following exception. The class of end points labeled  $q_3$  (Fig. 3) correspond to maximum entropy and maximum shock velocity points whereas the Chapman-Jouguet point in an analogous reaction would have minima for both quantities. The other classes of end points, the  $q_1$ ,  $q_2$ , and  $q_4$  classes, satisfy all the Chapman-Jouguet restrictions.

In Fig. 3 the dotted curves represent the locus of the  $\tilde{E} > 0$  contour end points. In region ABC,  $\tilde{E}^*$  is the maximum value of the electric field discussed in 2.2.1. The class of  $q_3$  end points all lie to the "right" of  $\tilde{E}^*$  while the  $q_2$  end points all lie to its "left."

From the foregoing discussion, it would be natural to propose that the most probable path of ionizing shock propagation is along the locus of contour end points, starting at  $\tilde{u}_1 = 0$  and following the locus through point A and point  $\tilde{E}^*$  to point C. From C we do not expect the path to back track to B and follow the dashed curve from  $B \rightarrow \infty$ , for this, again, poses the difficulty that for  $1 < \tilde{u}_1 < 2$  there will be multiple solution points. More likely, there is a transition curve from point C to the upper locus, while for  $\tilde{u}_1 > 2$  the path follows the upper end-point locus exactly.

Two objections, however, suggest an alternative path which is a slight modification of this end point proposal. The first objection is that, for the contours characterized by  $\tilde{u}_2 > 1$ , the  $q_1$  class of end points are all entropy decreasing and therefore inadmissible as shock solutions. This is apparent from Fig. 3 which shows the entropy increasing solutions, for  $\tilde{E}_1$ , all to the "right" of  $q_4$ , beyond the "bracket" point. This leads us to the suggestion that for  $\tilde{u}_2 > 1$ , the locus parallels the end point locus, but stays below it, and connects the "bracket" points on each contour. These are points of

no entropy change across the shock and therefore are entropy minima with respect to all other admissible solutions on a contour. The second objection is that for the  $q_2$  and  $q_3$  classes of end points there is no uniform region of hot gas behind the shock, i.e.  $X_e/X_s = 1$ . But, experimentally  $X_e/X_s$  has been measured and therefore the conjecture is that, just as in the  $\tilde{u}_2 > 1$  situation, the locus of solutions is a path just off the end point locus and paralleling it. It is well to note that the proposal of off-end point behavior is not unreasonable. In early detonation-deflagration studies, attempts to verify the Chapman-Jouquet hypothesis indicated definite off end point behavior. This was later attributed to the fact that the sound speed calculation used in the theory was for a single species gas and not for a mixture of species as occurs in any detonation process. When multiple species gases were considered the off end point behavior was explained. A similar situation is probably responsible for such behavior in ionizing shock studies.

A basic aim of this report is the verification of the proposal that there is a unique locus of solution points to the normal ionizing shock theory and that the locus is one that parallels the contour end point locus. In so doing we will demonstrate unambiguous separation of the shock current from the drive current and the existence of a small, but distinguishable, uniform hot plasma sample. This switch-on behavior of the ionizing front will be shown to extend to slow and fast shocks as predicted by the normal ionizing shock theory.

Table IV is a comparison between experimental results and the result of restricting the normal ionizing shock theory to the proposal of off end point locus behavior. The "General Statistics" section is self-explanatory. The ex-

perimental tabulation has already been discussed. The theoretical tabulation will be discussed now. Theoretical values were obtained as follows. For each run, #1 - 11, the output of a computer program (designed to give all downstream variables for a given set of upstream variables and including a jump in  $\gamma$ ) was plotted over the entire range of the electric field, i.e. from  $E=0$  to the value of  $E$  at which a contour end point was reached. In reality, the exact contour end point can only be obtained with extraordinary labor or extraordinary luck since the program employs a successive approximation method. Hence, the electric field was actually swept from 0, not to the end point, but to within 1/2% of the end point, sufficient accuracy for our purposes. In addition, since the experimental error in the shock velocity was  $\pm 10\%$ , each run was supplemented by programs covering  $\pm 10\%$  around the central value. In this way the error in the theoretical values could be included in the analysis. Note that each theoretical value in the table is followed by two error figures. The upper one corresponds to  $M_a + 10\%$  and the lower to  $M_a - 10\%$ . In some cases both errors are of the same sign. This will be explained later on.

For the first seven runs (runs #8 - 11 will be examined separately), the following procedure was used to obtain theoretical values and theoretical errors. At the computer program end point, as opposed to the exact end point,  $X_e/X_s$  (theoretical) and  $X_e/X_s$  (experimental) were compared. In all cases, they were within 3%, in most less than 1%. The values of  $B_3(\text{SW})$ ,  $\vartheta_0(\text{Drive})$ ,  $I(t)$ , and  $X_e/X_s$  were then read from the plots, at the computer end point, and recorded with their respective errors. Since we propose that operation is, indeed, off end point we are within rights in using

as we did the computer program end point. And, in addition, as was verified in several cases, between computer end point and actual end point none of the variables vary significantly. In several cases, one example being  $B_{\theta}(SW)$  in run #6, both errors are negative. This simply means that, at this value of  $M_a$ ,  $B_{\theta}(SW)$  (theory) is a relative maximum. Varying the shock velocity  $\pm 10\%$  around the value gives smaller switch-n fields. The reasoning is exactly the same for two positive errors, only here the main value is a relative minimum (see run #8,  $B_{\theta}(SW)$  theory). When the errors are of opposite sign but of different magnitude it means that the main result is close to a stationary value.

In the first seven runs, agreement, though crude, is reasonably good. In only one run (run #4) is there more than one value that is beyond the range of experimental and theoretical error. In addition, in runs #1, 2, 4, and 5 a variation of less than 3% in the off end point position brings all values within experimental error. A disparity of 3% is not unreasonable when viewed in the context of the early detonation-deflagration studies where a 5% error was common. In run #2 a 12% shift in end point is needed to bring  $B_{\theta}(SW)$  into agreement and a 31% shift is needed for  $B_{\theta}(SW)$ , run #3. These last two points are distinctly out of line. For runs #6 and #7,  $B_{\theta}(Drive)$ , in each case, is outside the bounds of experimental error. Variation in the end point position cannot account for the error and these two individual measurements must be viewed with suspicion.

Runs #8 and #9 are borderline runs. In each case  $M_a$ , and  $M_a - 10\%$  are trans-Alfvenic, but  $M_a + 10\%$  is super-Alfvenic, and in the super-Alfvenic region the magnitudes of the downstream variables are quite different from the magnitudes in the trans-Alfvenic region. This is immediately

apparent from the errors assigned to the theoretical values for the runs. The enormous range available for the switch-on fields makes the measurement almost pointless unless the shock velocity error can be reduced to less than 5%. In any event it is comforting that the measured values of  $B_{\theta}(SW)$ , in both cases, lie above the main theoretical value, as they must if they are to fit the theory in any sense. The drive fields on the other hand are not within the experimental error and variation of the end point position cannot bring them into line. In the total picture runs #8 and #9 must be viewed as suggestive, at best. Only the  $B_{\theta}(Drive)$  measurement does not agree with experiment, but even so until the shock velocity error can be reduced the range of switch-on error and  $X_e/X_s$  error will remain disconcertingly large.

Runs #10 and #11 are both super-Alfvenic runs. We cannot go immediately to the contour end points for our theoretical values because, as we have seen, they are entropy decreasing points. We must first find the "bracket" points where the entropy begins to go positive. However, in the computer program developed for the determination of theoretical values, we have used a jump in  $\gamma$  across the shock front and it is not apparent how to calculate the entropy jump for such a situation. All that can be proved from examination of the steady state shock theory is that, even if  $\gamma$  jumps across the shock, the  $q_4$  class of end points is always entropy decreasing. The exact numerical value cannot be simply computed. The best that can be done is to return to the steady state theory where  $\gamma$  does not jump and find the value of  $\tilde{E}$  at which the bracket point occurs. With this as a guide, a guess can be made as to where the bracket point occurs for the case where  $\gamma$  jumps. In fact, this procedure is perfectly acceptable because the numerical values of the downstream variables do not differ by more

than .1% between the case where  $\gamma$  is constant across the shock and the case where  $\gamma$  is assumed to jump across the shock.

For the runs under consideration it turns out that the bracket point in each case is no more than .5% from the contour end point. Using the value of  $\tilde{E}$  appropriate to the bracket point the theoretical values for  $B_{\theta}(\text{SW})$ ,  $B_{\theta}(\text{Drive})$ ,  $X_e/X_s$ , and  $I(t)$  are listed in their respective columns.

Agreement between theory and experiment in run #10 is fair.  $B_{\theta}(\text{Drive})$  and  $I(t)$  are within the error bounds while  $X_e/X_s$  and  $B_{\theta}(\text{SW})$  are not. However, a shift of 6% in the bracket point will bring all quantities into agreement. In run #11  $B_{\theta}(\text{SW})$  and  $I(t)$  are beyond the bounds of the assigned errors, while  $B_{\theta}(\text{Drive})$  and  $X_e/X_s$  are well within the tabulated uncertainties. A shift of 7% in the bracket point will make  $B_{\theta}(\text{SW})$  consistent with the other results, but such a shift merely accentuates the disparity in  $I(t)$ . We are therefore forced to view run #11 as somewhat anomalous.

### 3.5 Conclusions

Using a co-axial electromagnetic shock tube we have been able to propagate, record, and analyze steady, plane switch-on ionizing shocks in the sub-Alfvénic, trans-Alfvénic and super-Alfvénic regimes. The results are in confirmation of the theory of normal ionizing shocks. The experimental existence of the super-Alfvénic switch-on front is strong evidence that a recent argument suggesting that such shocks have no structure may be in error.

We have presented a proposal, modeled on the Chapman-Jouquet theory of detonations, to describe the behavior of such ionizing shocks. It has been shown that the data obtained is in tentative agreement with such a theory, except for the region in the immediate vicinity of the transition point from trans-Alfvénic to super-Alfvénic propagation.

Existence of a small, but definite, homogeneous gas sample has been demonstrated and shown to fit into the proposed scheme.

In conclusion, the experiment described in this report, gives new insight into the behavior of an important class of magnetohydrodynamic phenomena - the normal ionizing shock front.

No attempt was made to propagate expansive (sub-sonic) ionizing shocks even though their existence is predicted by the theory. It is well known, from conventional shock studies, that such shocks do not produce significant ionization of the post-shock gas and thus, they would not be covered by the ionizing shock theory. The theory cannot be expected to explain phenomena in this velocity range.

#### 4. REFERENCES

- 1) Riemann, B., Gesammelte Werke, p. 144(1876).
- 2) Earnshaw, S., Trans. Roy. Soc. 150, 133(1860).
- 3) Vieille, P., Compt. Rend. 129, 1228(1899).
- 4) Payman, W., and others, Proc. Roy. Soc. A 132, 200(1931) etc.
- 5) de Hoffman, F., Teller, E., Phys. Rev. 80, 692 (1950).
- 6) Fowler, R. G., Goldstein, J. S., Clothfelter, B. E., Phys. Rev. 82, 879 (1951).
- 7) Liubimov, G. A., Doklady, Akad. Nauk. S.S.S.R. 126, 291(1959).
- 8) Liubimov, G. A., Kulikovskiy, A. G., Doklady. Akad. Nauk. S.S.S.R. 129, 52(1959).
- 9) Liubimov, G. A., Kulikovskiy, A. G., Doklady. Akad. Nauk. S.S.S.R. 129, 525(1959).
- 10) Gross, R. A., Kunkel, W. B., "Hydromagnetic Ionizing Waves," Plasma Hydrodynamics, Stanford Univ. Press, 1962, pp. 58-82.
- 11) Helliwell, J. B., Pack, D. C., Phys. Fluids 5, 738(1962).
- 12) Bazer, J., Ericson, W., "Hydromagnetic Shocks," N.Y.U. Institute of Mathematical Sciences, Research Report No. MH-8, January 1958, and Phys. Fluids 3, 631 (1960).
- 13) Friedrichs, K. O., "Non-Linear Wave Motion in Magneto-hydrodynamics," Los Alamos Report, LAMS 2105 (1954).
- 14) Friedrichs, K. O., Kranzer, H., "Notes on Magneto-hydrodynamics VIII, Non-Linear Wave Motion," N.Y.U. Institute of Mathematical Sciences, NYO - 6486, July 31, 1958.
- 15) Lust, R., Zeitschrift Fur Naturforschung 8a, 277, (1953).
- 16) Lundquist, S., Arkiv Fur Fysik, Band 5, (1952).

- 17) van de Hulst, H. C., "Interstellar Polarization and Magneto-hydrodynamic Waves in Problems of Cosmical Aerodynamics," Int. Union of Theor. and Appl. Mech. and Int. Astr. Union, Proc. Symposium Paris, 1949.
- 18) Herlofson, N., *Nature* 165, 1020 (1950).
- 19) Jeffrey, A., Taniuti, T., Nonlinear Wave Propagation with Applications to Physics and Magnetohydrodynamics, Academic Press, 1964.
- 20) Longmire, C. L., Elementary Plasma Physics, Interscience, 1963, pp. 21-24.
- 21) Kantrowitz, A. R., Petschek, H. E., "MHD Characteristics and Shock Waves," Avco Everett Research Report 185, July, 1964.
- 22) Courant, R., Friedrichs, K. O., Supersonic Flow and Shock Waves, Interscience, 1948, pp. 110f.
- 23) Ludford, G.S.S., *J. Fluid Mech.* 5, 67(1959).
- 24) Gardner, C. S., Kruskal, M.D., *Phys. Fluids* 7, 700 (1964).
- 25) Kolb, A. C., *Phys. Rev.* 107, 345 (1957).
- 26) Patrick, R. M., *Phys. Fluids* 2, 589(1959).
- 27) Garwin, R., Rosenbluth, M., Los Alamos Scientific Laboratory Report LA-1850, (1954).
- 28) Wright, J. K., Black, M. C., *J. of Fluid Mech.*, 6, 289(1959).
- 29) Kemp, N. H., Petschek, H. E., *Phys. Fluids* 2, 599(1959).
- 30) Camac, M., Patrick, R. M., "Experimental Investigations of Collision-Free Shocks and Plasmas," Avco-Everett Research Report 122, Sept. 1961.
- 31) Heiser, W. H., *Phys. Fluids* 7, 143(1964).
- 32) Heywood, J. B., "Diagnostic Experiments in a Magnetically Driven Shock Tube," M.I.T. Fluid Mechanics Laboratory Publication No. 65 - 1, January 1965.
- 33) Taussig, R., "Normal Ionizing Shock Waves," Columbia University Plasma Laboratory Rept. 12, July 1964.

- 34) Chu, C. K., Phys. Fluids 7, 1349(1964).
- 35) Taussig, R., "Normal Ionizing Shock Waves - The Effects of Equilibrium, Dissociation and Ionization," Columbia University Plasma Laboratory Rept. 14, August, 1964.
- 36) Brennan, M. H., Brown, I. G., Millar, P. P., Watson-Munro, C.N., J. Nuclear Energy, Part C, Plasma Physics 5, 229 (1963).
- 37) Brennan, M. H., Lehane, J. A., Millar, D. D., Watson-Munro, C.N., Australian J. Phys. 16, 340(1963).
- 38) Sharp, L., Watson-Munro, C. N., Phys. Rev. Letters 11, 39(1964).
- 39) Vlases, G. C., J. Fluid Mech. 16, 82(1963).
- 40) Vlases, G. C., Phys. Fluids 7, 1358(1964).
- 41) Patrick, R. M., Pugh, E. R., Phys. Fluids 8, 636(1965).
- 42) Lovberg, R., Phys. Fluids 7, 557(Nov. 1964, Part 2).

## 5. ACKNOWLEDGEMENTS

It is a pleasure to extend my thanks to the following people for their help in bringing this study to fruition.

To Professor Robert A. Gross - my sincere appreciation for everything, in particular, for your never failing encouragement and advice.

To Professor C.K. Chu - many thanks for the discussions that shed light on many difficult problems.

To Leslie Levine - without your patient and unselfish help this work could not have been completed.

To Robert Taussig - whose theory is the basis of this study. Thank you for the hours you spent in helping me understand it.

To Maurice Cea - my very deepest appreciation for all your work in designing, re-designing, building and re-building the shock tube.

To the members of the Plasma Laboratory - thank you for the fond memories of an association that I will always cherish.

And, finally, to my long-suffering wife, Pat, and my daughter, Beth-Ann (age 1 year) - your patience and your love kept me going when all else failed.

## 6. FIGURES AND TABLES

<u>Figures</u>	<u>Page</u>
1 "Classical" MHD Shock Geometry	73
2 $\bar{u}_2$ Plotted as Function of $\bar{u}_1$	74
3 $\bar{u}_2$ vs. $\bar{u}_1$ for Ionizing Shocks	75
4 The Magnetic Piston in Coaxial Geometry	76
5 Schematic Cross-Section Through Shock Tube	77
6 Longitudinal Magnetic Field Plot	78
7 Detail of Knife Edge Assembly	79
8 Shaped-Pulse Capacitor Bank	80
9 Current Pulse from Capacitor Bank	81
10 Capacitor Bank and Enclosure	82
11 Air-Gap Switch and Firing Circuit	83
12 Air-Gap Switch in Operating Position	84
13 R.F. Pre-Ionizer Circuit	85
14 Timing and Firing Circuits	86
15 Current Monitor	87
16 Current Monitor Circuit	88
17 Photomultiplier Port Details	89
18 Photomultiplier Circuit	90
19 $B_\theta$ Probe: Schematic and Circuit	91
20 $B_\theta$ Probe: Construction	92
21 Electric Field Probe: Construction	93
22 X - t Diagram for Determination of Shock Velocity	94
23 Analysis of Photomultiplier Data	95
24 Ideal Shock Tube Behavior	96
25 Current and Magnetic Field Distribution in Ideal Shock Tube	97

<u>Figures</u>	<u>Page</u>
26 Sample EMP and $B_{\theta}$ Derived from It	98
27 Single Turn $B_{\theta}$ Probe Geometry	99
28 $B_{\theta}$ Analysis (1)	100
29 $B_{\theta}$ Analysis (2)	101
30 $B_{\theta}$ Analysis (3)	102
31 $B_{\theta}$ Structure Study	103
 Table I Shock Velocity vs. Alfven Mach Number, $M_a$	 104
Table II Current Through Shock Tube For Runs in Table I	105
Table III Experimental Data for $B_{\theta}(SW)$ , $B_{\theta}(Drive)$ , and $X_e/X_s$	106
Table IV Comparison Between Theory and Experiment	107

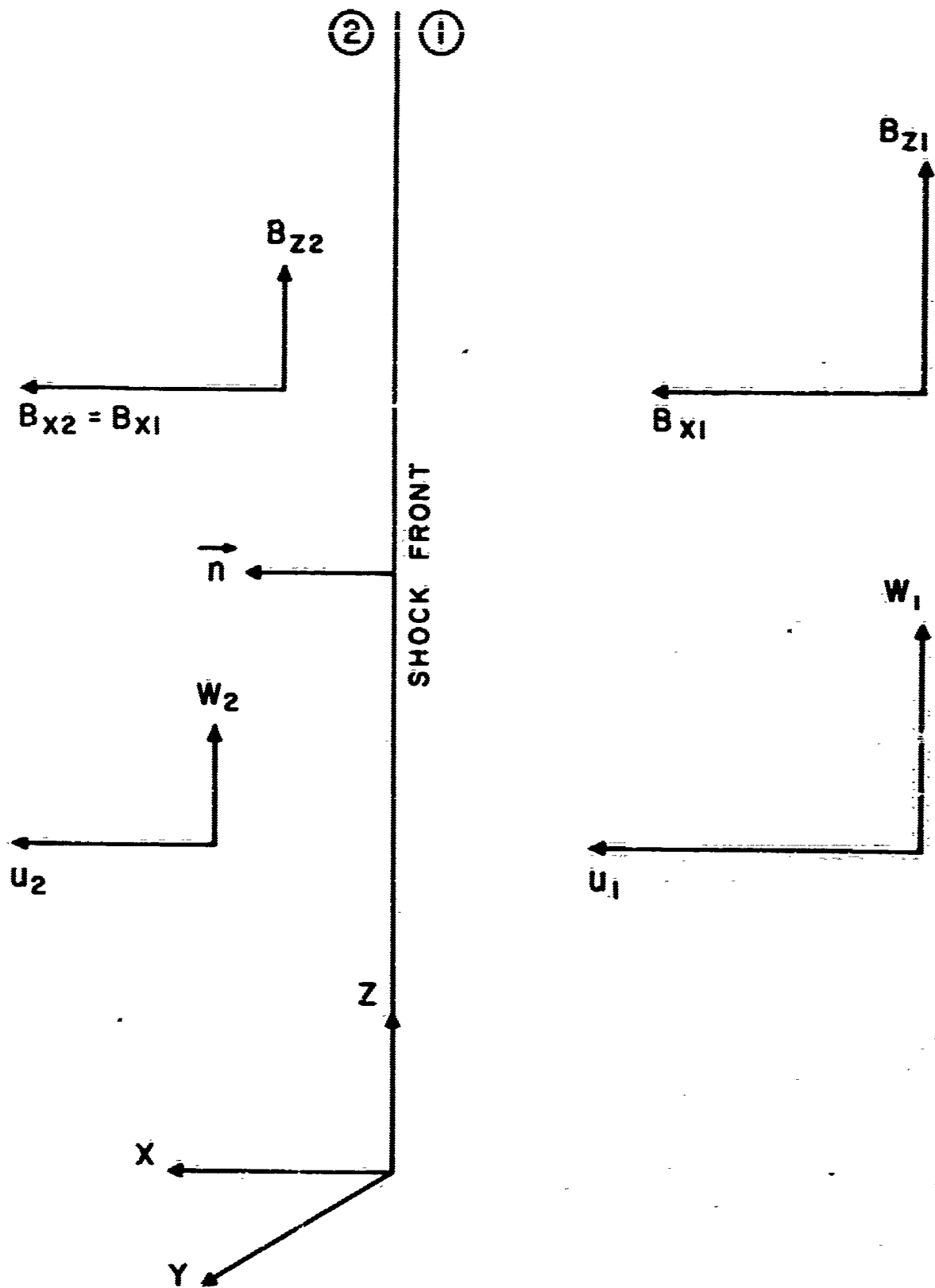


FIG. 1 "CLASSICAL" MHD SHOCK GEOMETRY.





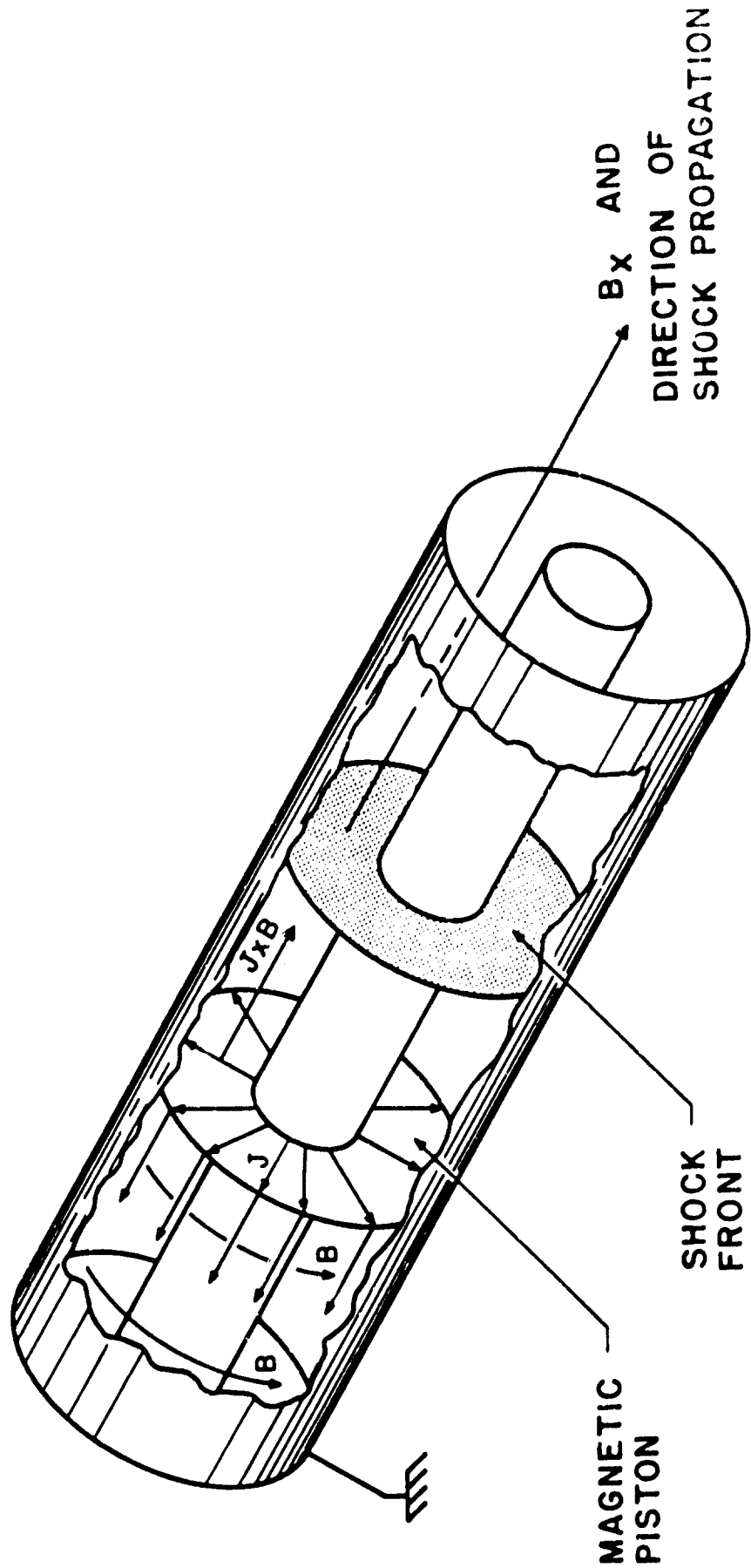


FIG. 4 THE MAGNETIC PISTON IN CO-AXIAL GEOMETRY .

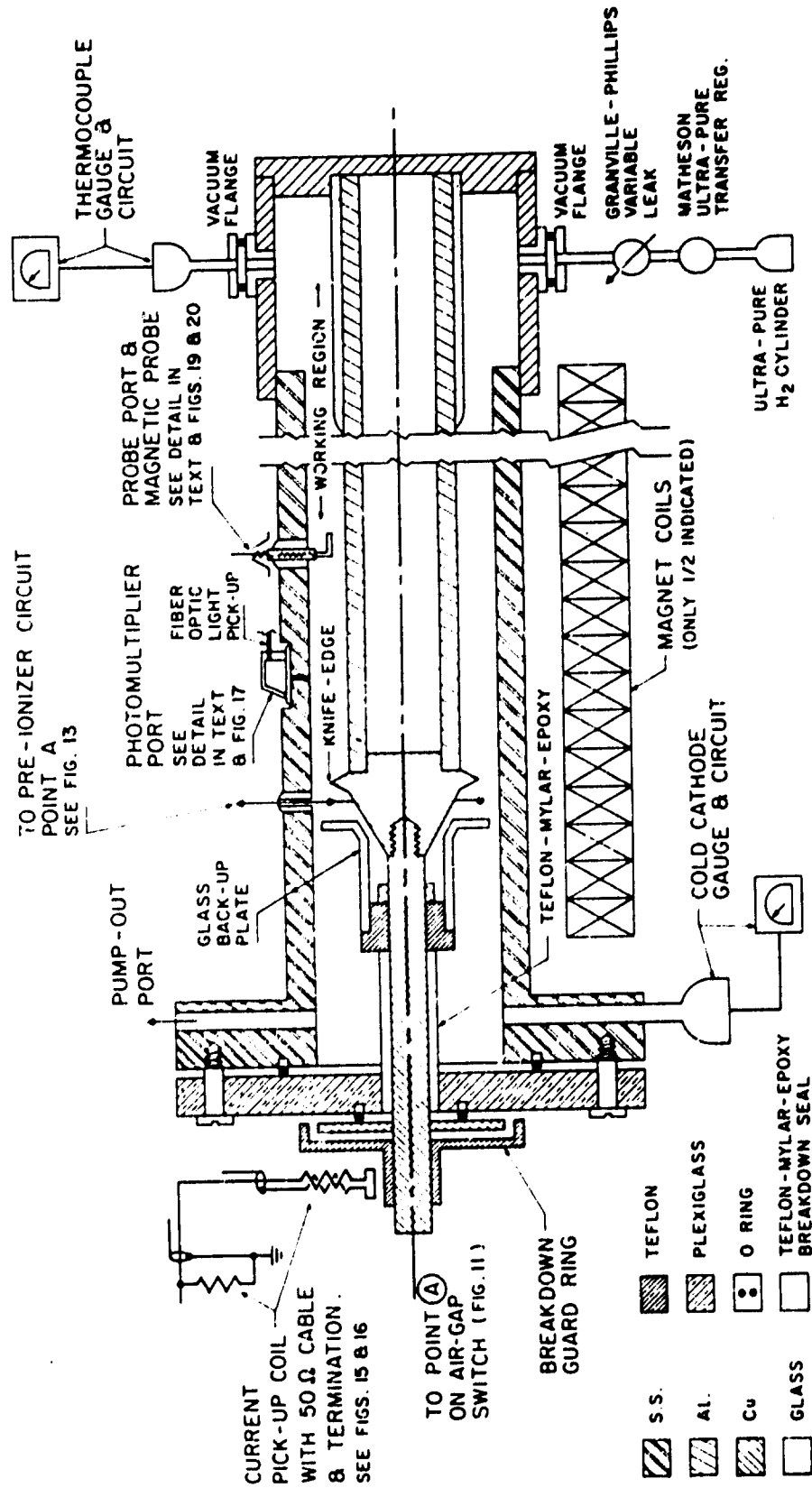


FIG. 5 SCHEMATIC CROSS-SECTION THROUGH SHOCK TUBE . ( NOT TO SCALE )

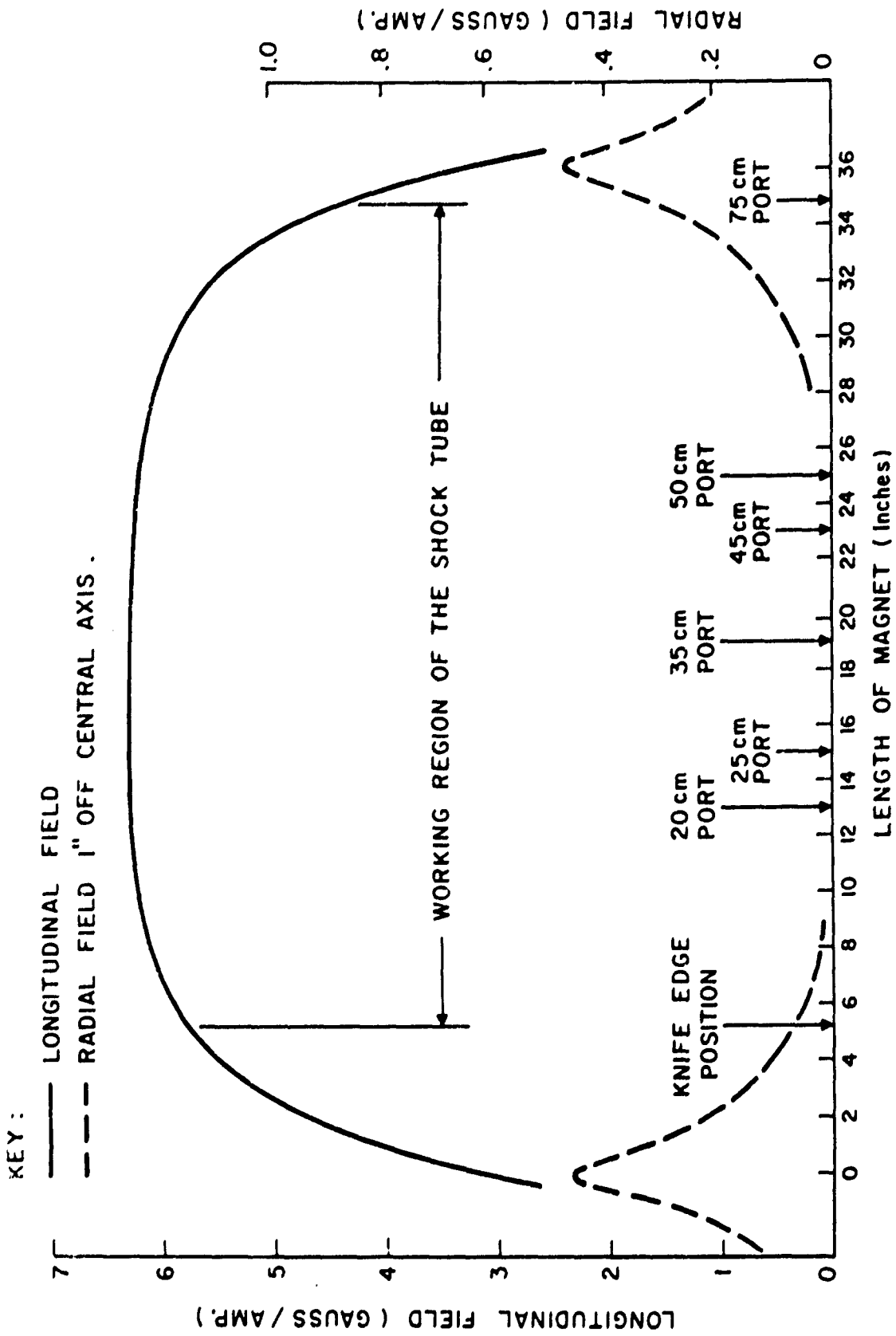
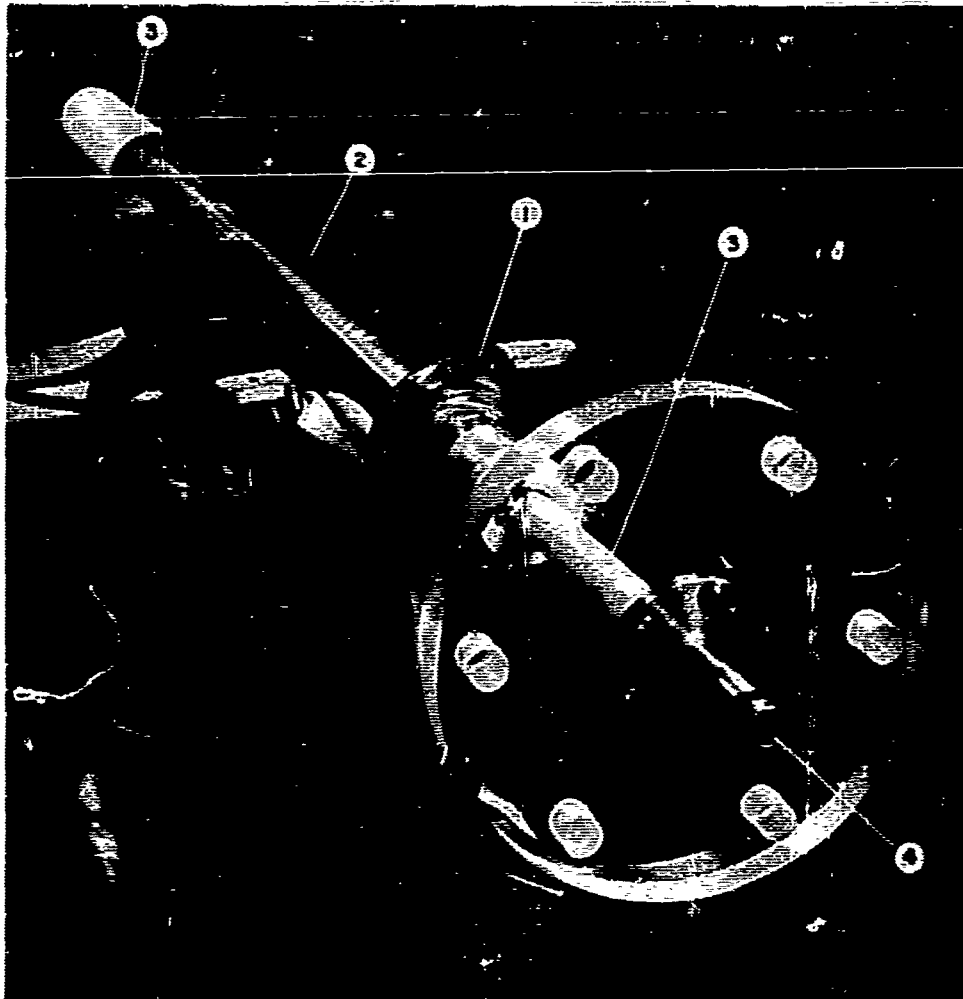
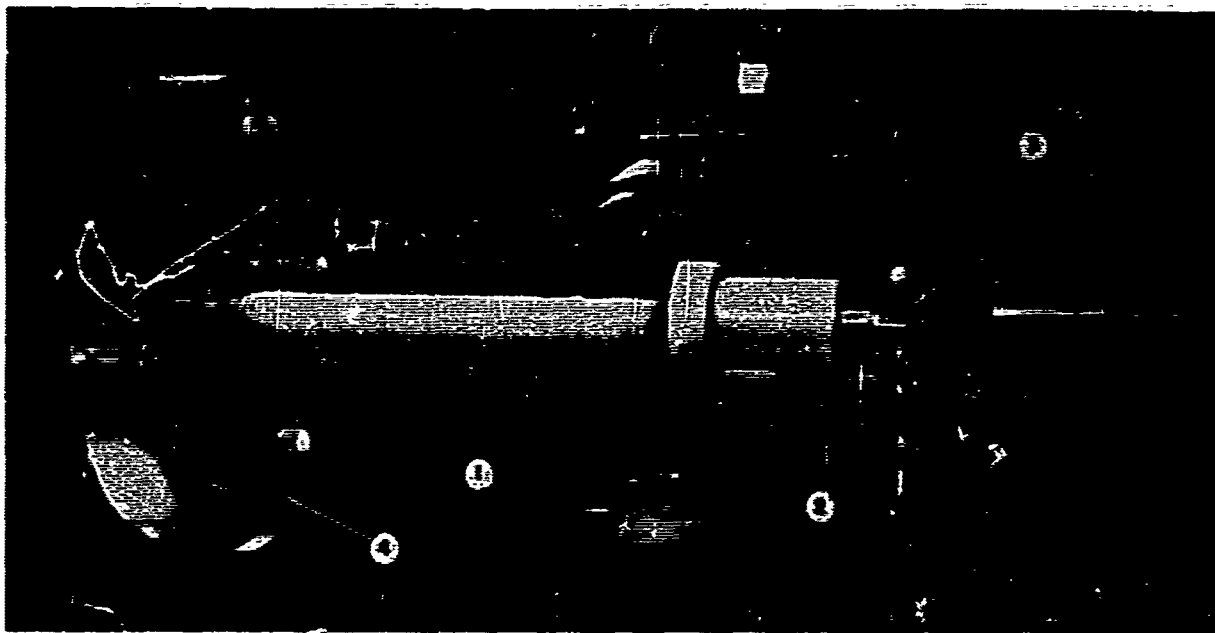


FIG. 6 LONGITUDINAL MAGNETIC FIELD PLOT AND ITS RELATION TO SHOCK TUBE .

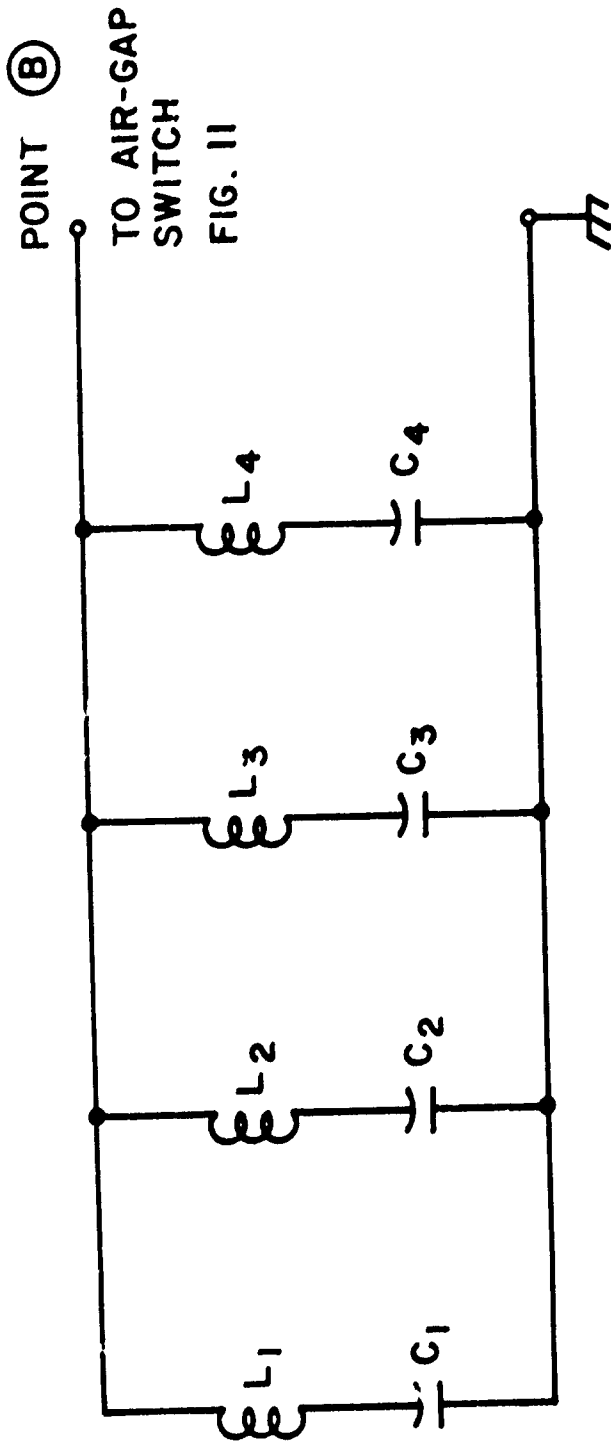


- (a)
1. Glass Back-up Plate
  2. Inner Conductor
  3. Teflon-Mylar Epoxy Breakdown Seal
  4. Copper Feed-Through



- (b)
1. Teflon-Mylar Epoxy Breakdown Seal
  2. Glass Back-up Plate
  3. Knife-Edge
  4. Plexiglas End Piece

FIG. 7 DETAIL OF KNIFE EDGE ASSEMBLY



- $C_1 : 14 - 2 \mu f , 50,000 \text{ WVDC} = 28 \mu f$        $L_1 = .496 \mu h$
- $C_2 : 2 - 1.35 \mu f , 50,000 \text{ WVDC} = 2.70 \mu f$        $L_2 = .568 \mu h$
- $C_3 : 1 - .72 \mu f , 50,000 \text{ WVDC} = .72 \mu f$        $L_3 = .764 \mu h$
- $C_4 : 1 - .22 \mu f , 50,000 \text{ WVDC} = .22 \mu f$        $L_4 = 1.326 \mu h$

FIG. 8 SHAPED - PULSE CAPACITOR BANK

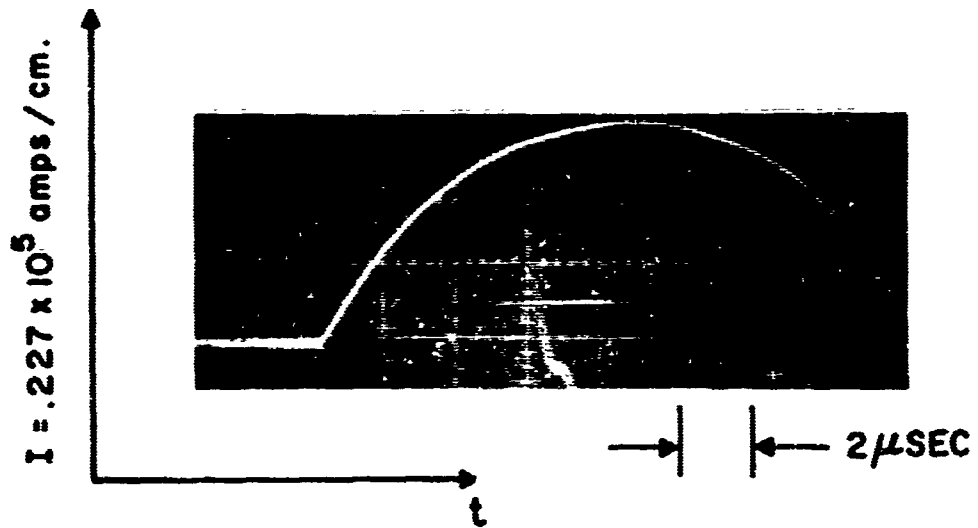
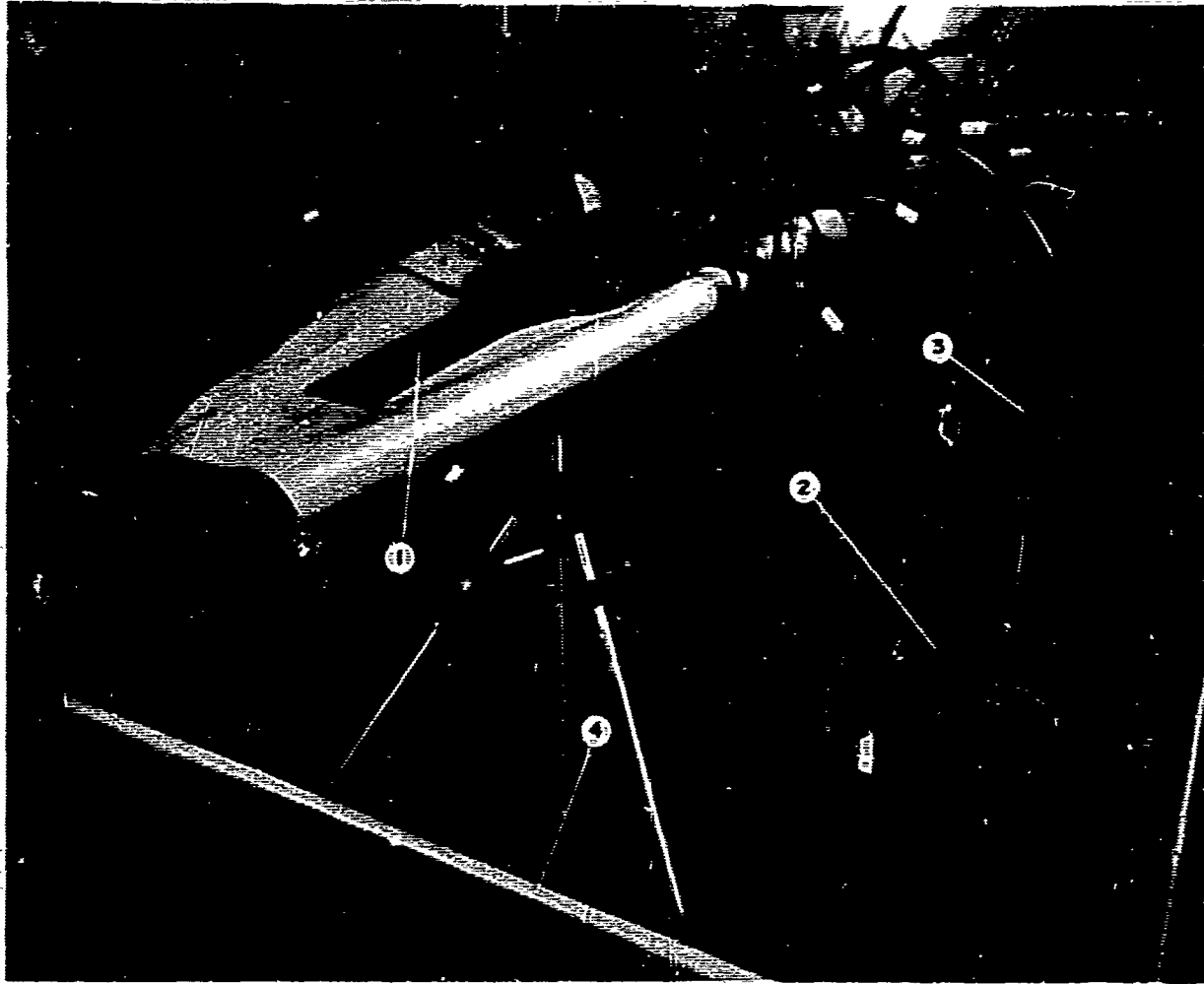


FIG. 9 CURRENT PULSE FROM CAPACITOR BANK



1. Top Plate of Parallel Plate Transmission Line
2. Representative Capacitor
3. Series Inductor
4. Enclosure

**FIG. 10 CAPACITOR BANK AND ENCLOSURE**

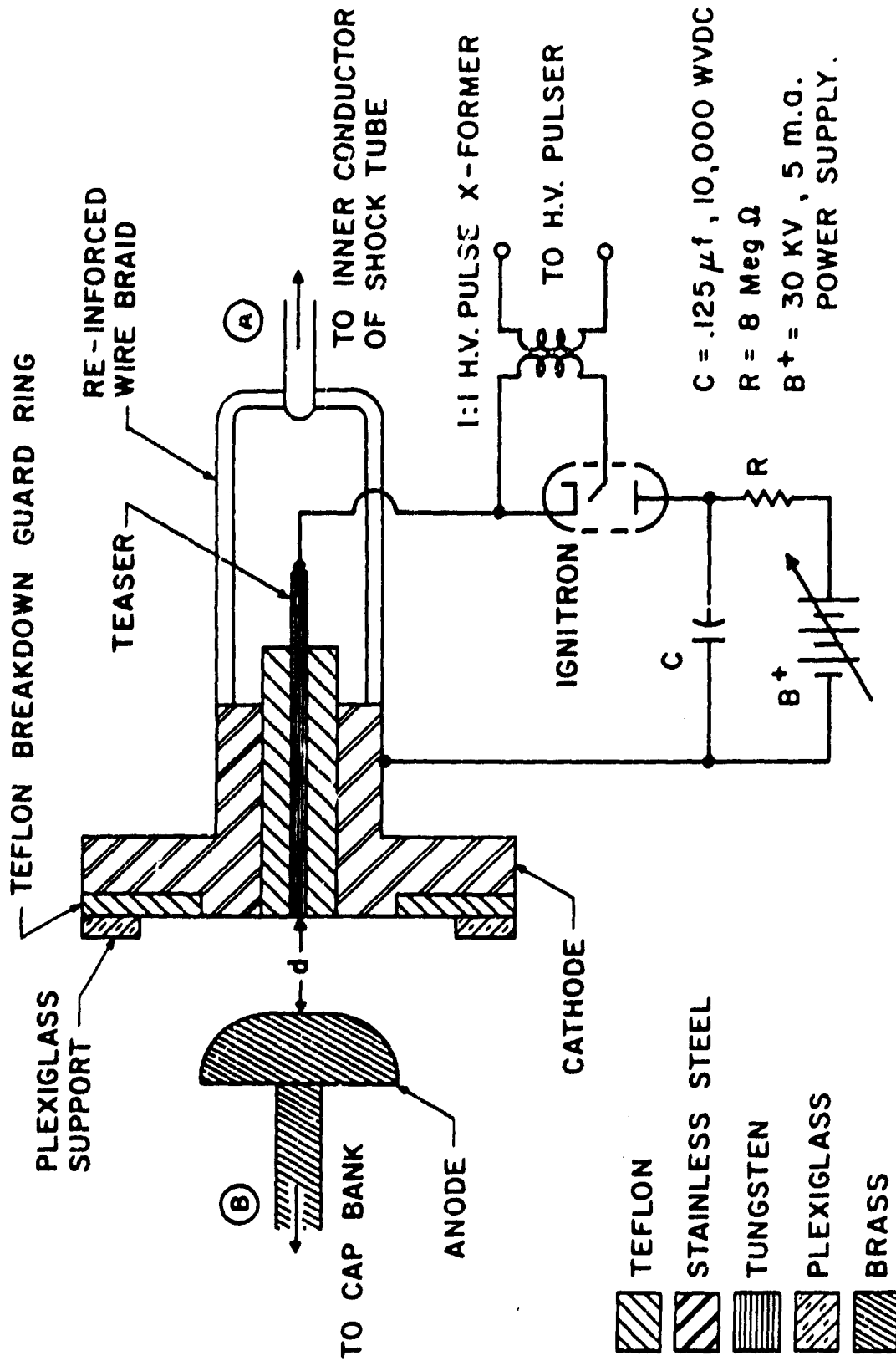
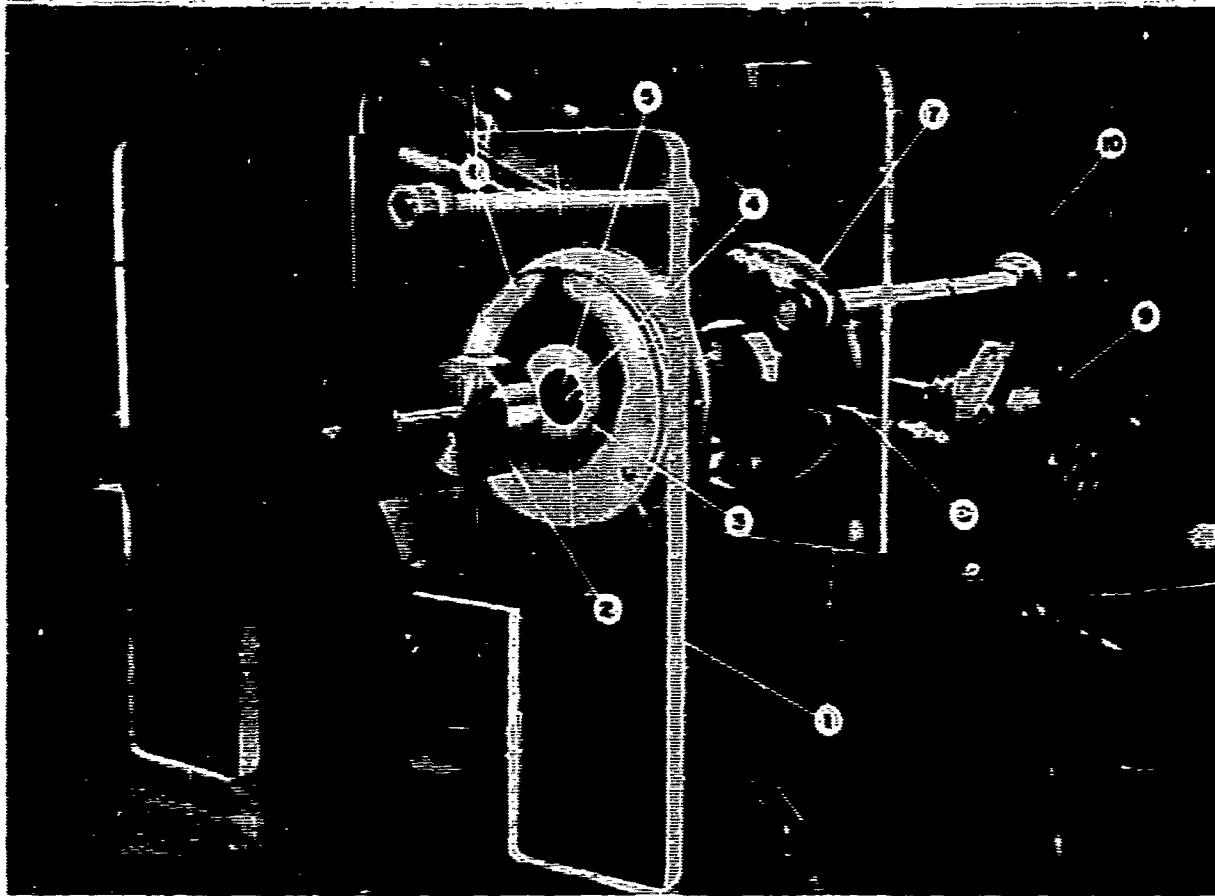


FIG. 11 AIR-GAP SWITCH AND FIRING CIRCUIT.



1. Switch Support Plates
2. Anode
3. Teflon Breakdown Guard Ring
4. Teaser
5. Cathode
6. Plexiglas Support
7. Main Body of Shock Tube
8. Current Monitor Probe (See Fig. 15)
9. Cold Cathode Gauge
10. Magnet Coils

**FIG. 12 AIR GAP SWITCH IN OPERATING POSITION**

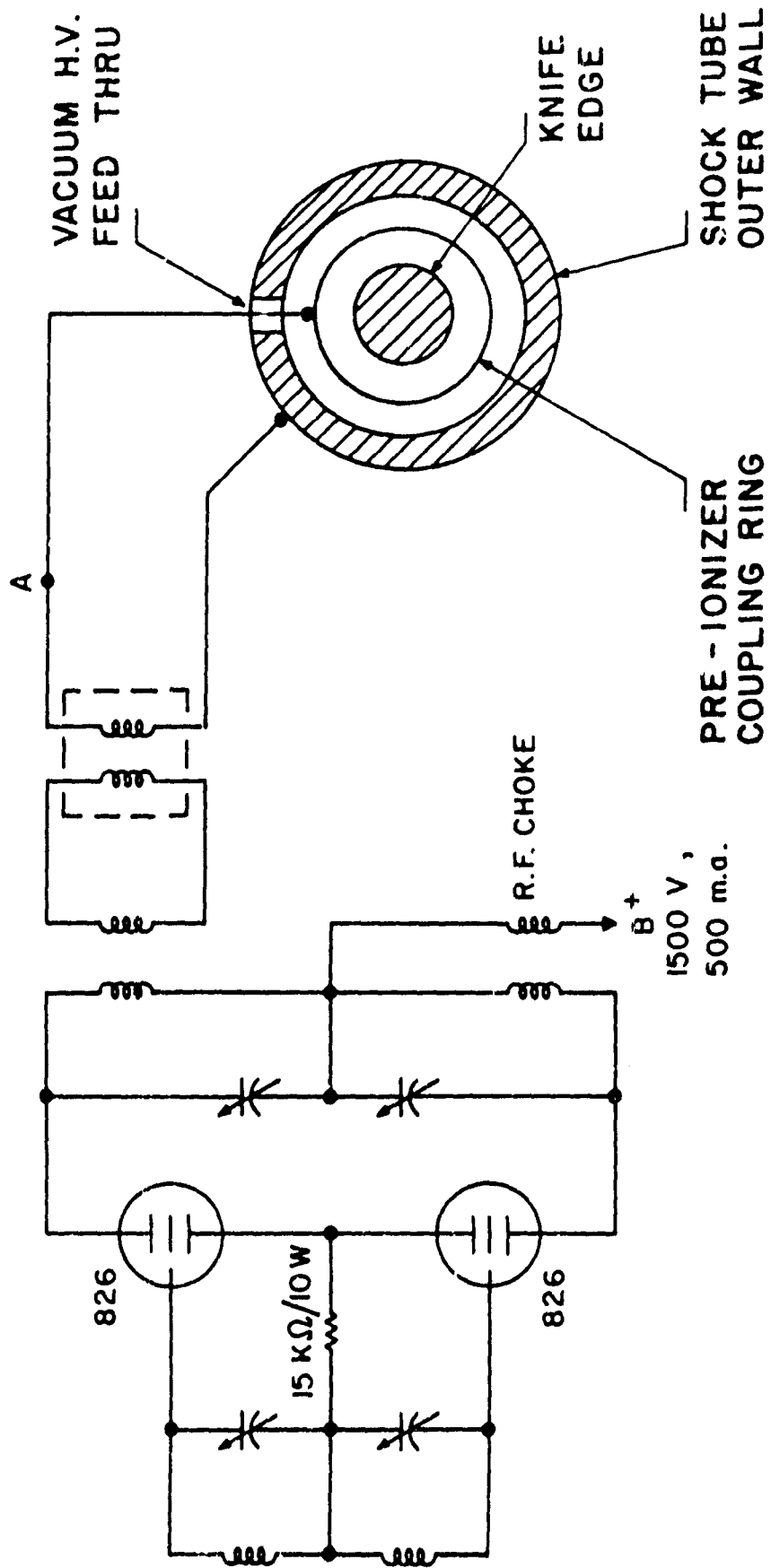
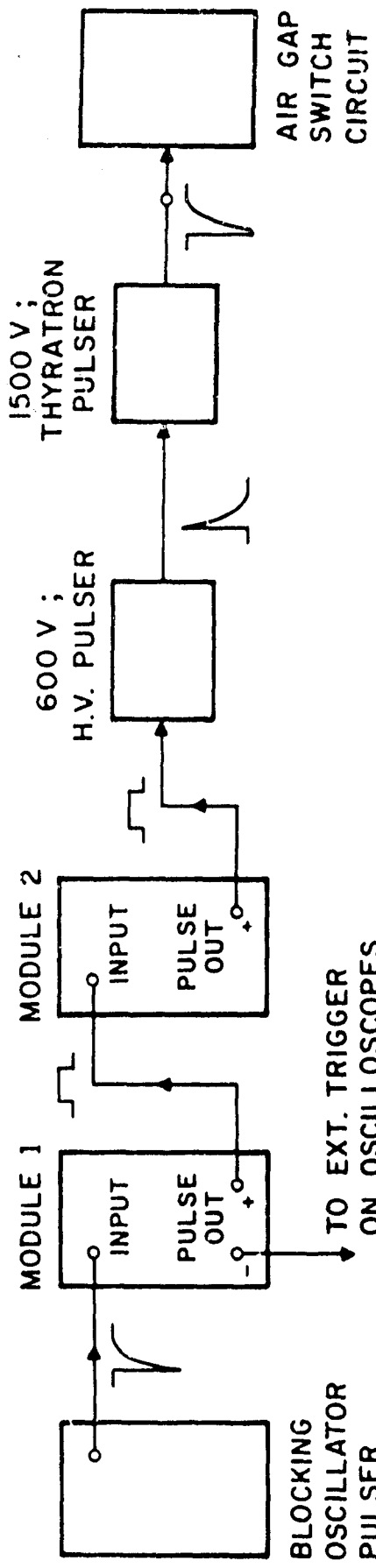


FIG. 13 30 Mc/s, R.F. PRE - IONIZER CIRCUIT .



TIME SEQUENCES :

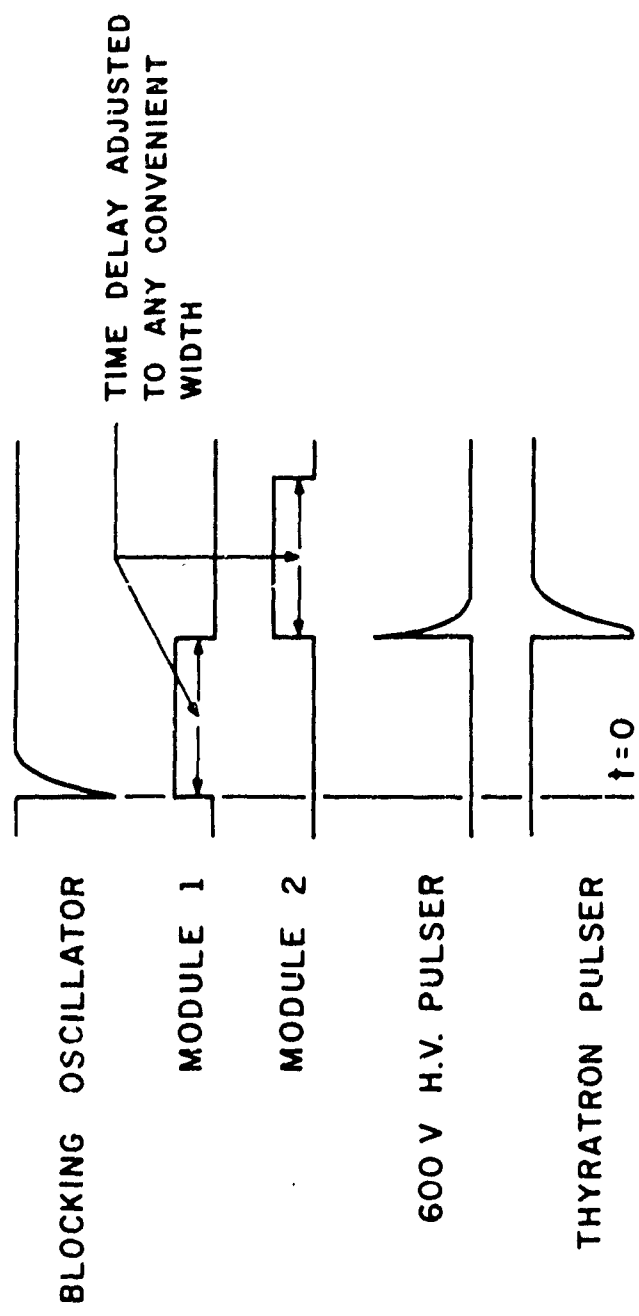
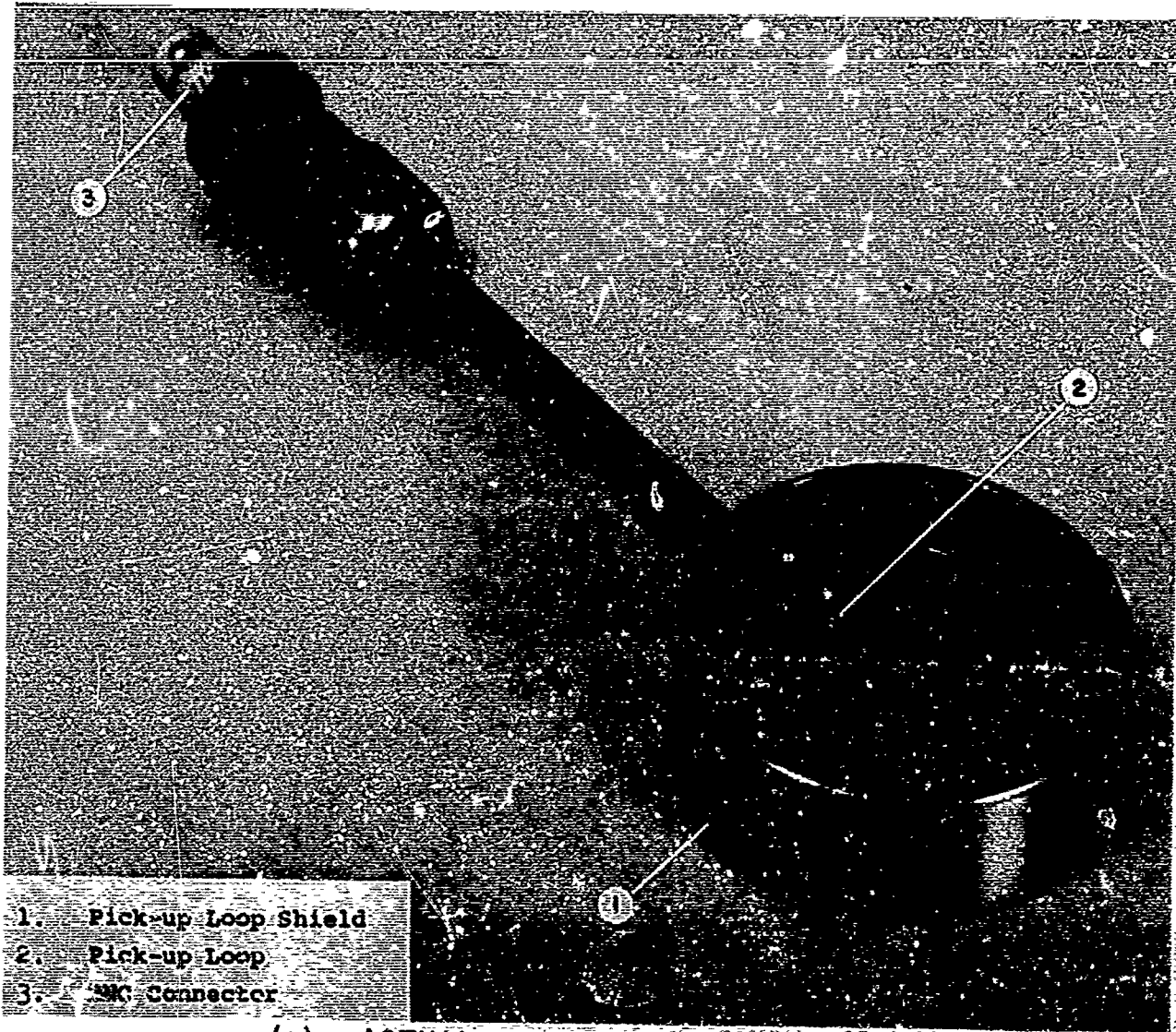
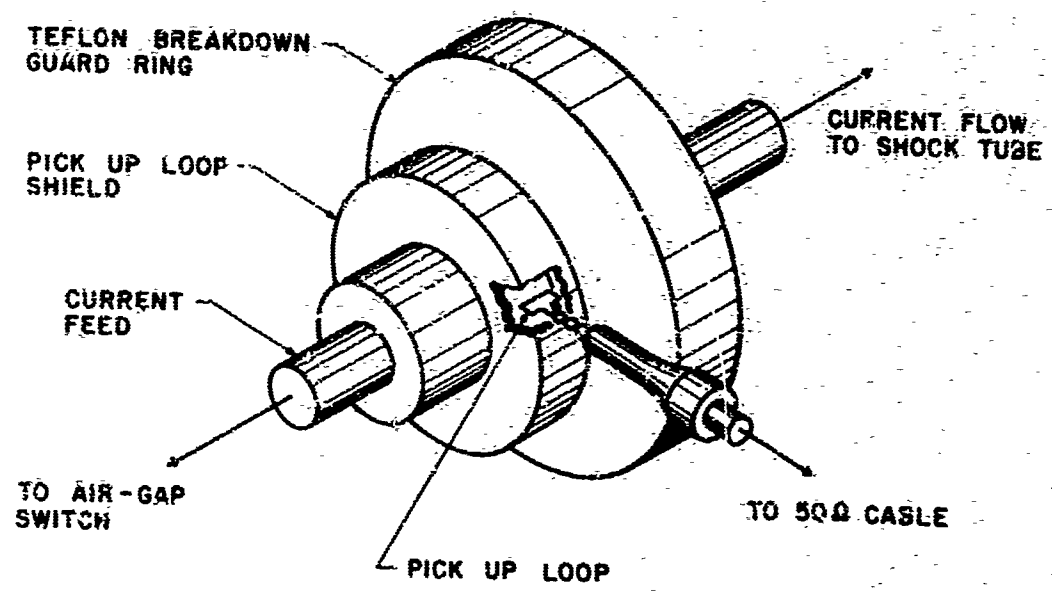


FIG.14 TIMING AND FIRING CIRCUITS .



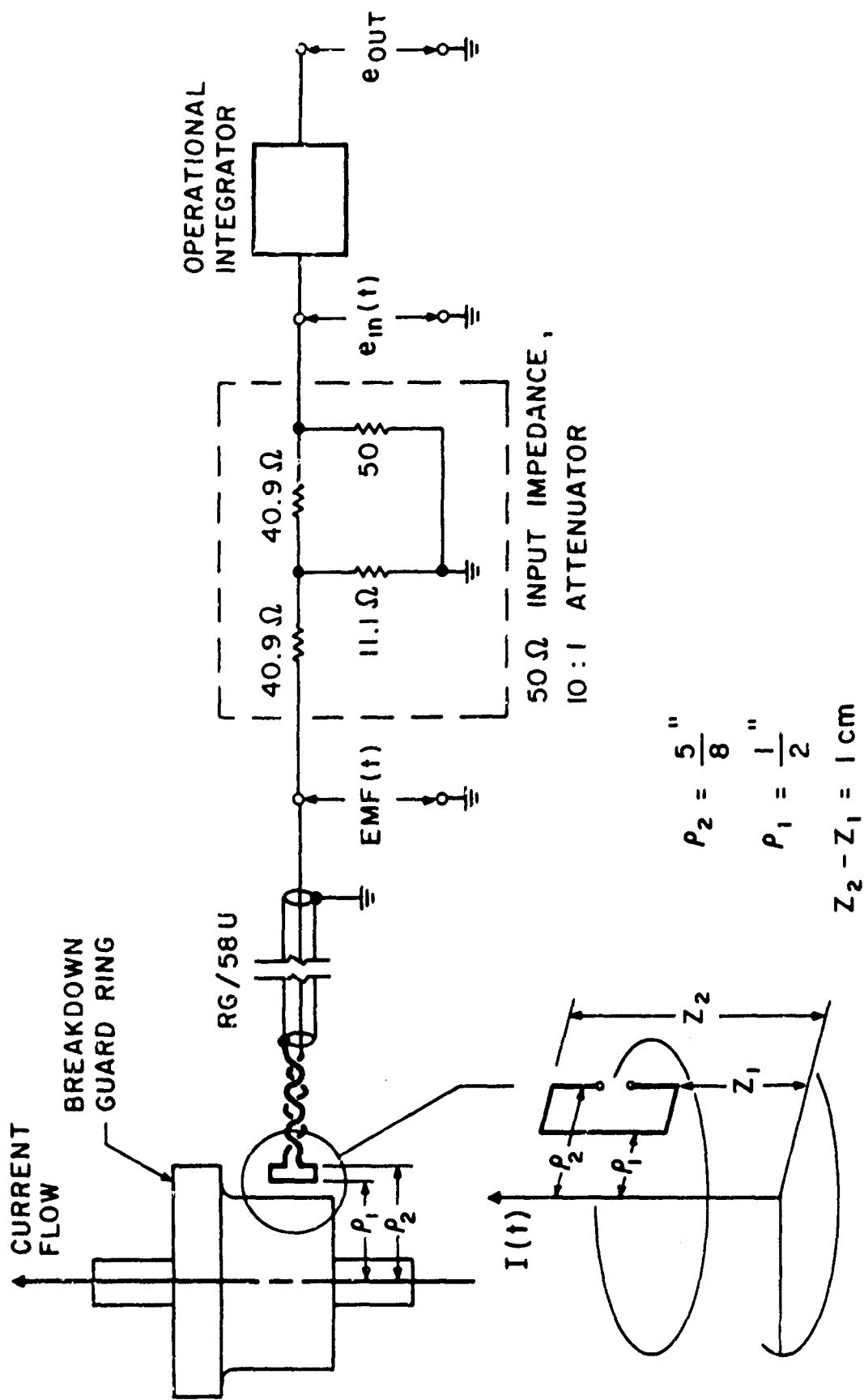
- 1. Pick-up Loop Shield
- 2. Pick-up Loop
- 3. MC Connector

(a) ACTUAL PROBE



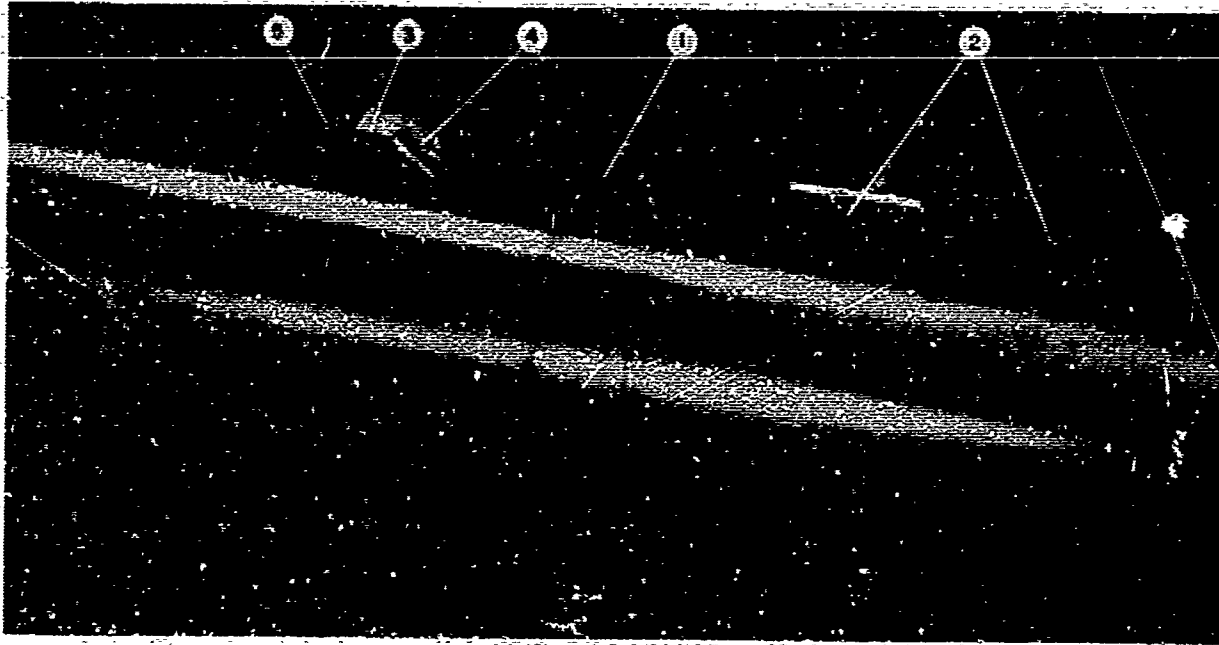
(b) SCHEMATIC OF PROBE ARRANGEMENT

FIG. 15 CURRENT MONITOR



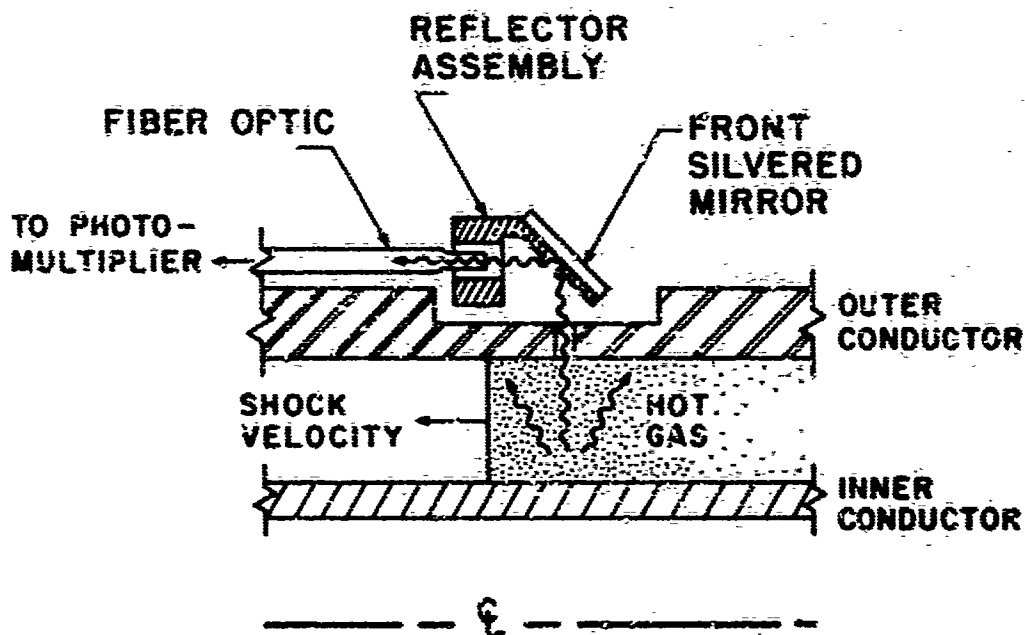
GEOMETRY & DIMENSIONS

FIG.16 CURRENT MONITOR CIRCUIT AND DIMENSIONS



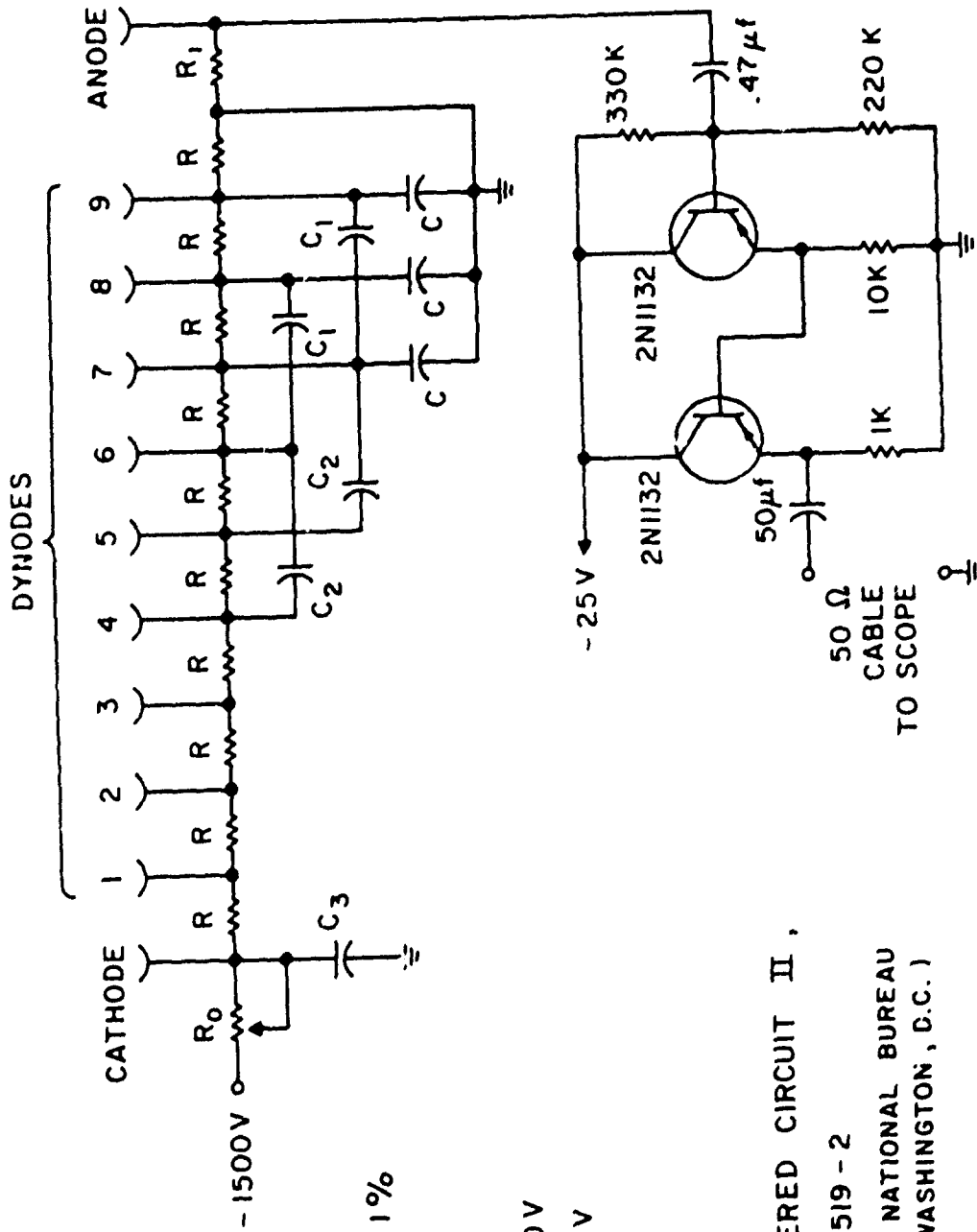
1. Shock Tube Body
2. Photomultiplier Port showing 1/16" hole
3. Reflector Assembly
4. Front Silvered Mirror
5. Fiber Optic

(a) ACTUAL ASSEMBLY



(b) SCHEMATIC

FIG. 17 PHOTOMULTIPLIER PORT DETAILS



- $R_0 = 1 \text{ meg} / 2 \text{ W}$
- $R = 100 \text{ K} / 1/2 \text{ W} / 1\%$
- $R_1 = 2 \text{ K}\Omega / 1/2 \text{ W}$
- $C = .1 \mu\text{f} / 600 \text{ V}$
- $C_1 = 1000 \mu\text{f} / 600 \text{ V}$
- $C_2 = 100 \mu\text{f} / 600 \text{ V}$
- $C_3 = .01 \mu\text{f} / 2 \text{ KV}$

DESIGN NOTES :  
 HANDBOOK PREFERRED CIRCUIT II ,  
 NAVWEPS 16 - 1 - 519 - 2  
 ( AVAILABLE FROM NATIONAL BUREAU  
 OF STANDARDS , WASHINGTON , D.C. )

FIG. 18 PHOTOMULTIPLIER CIRCUIT

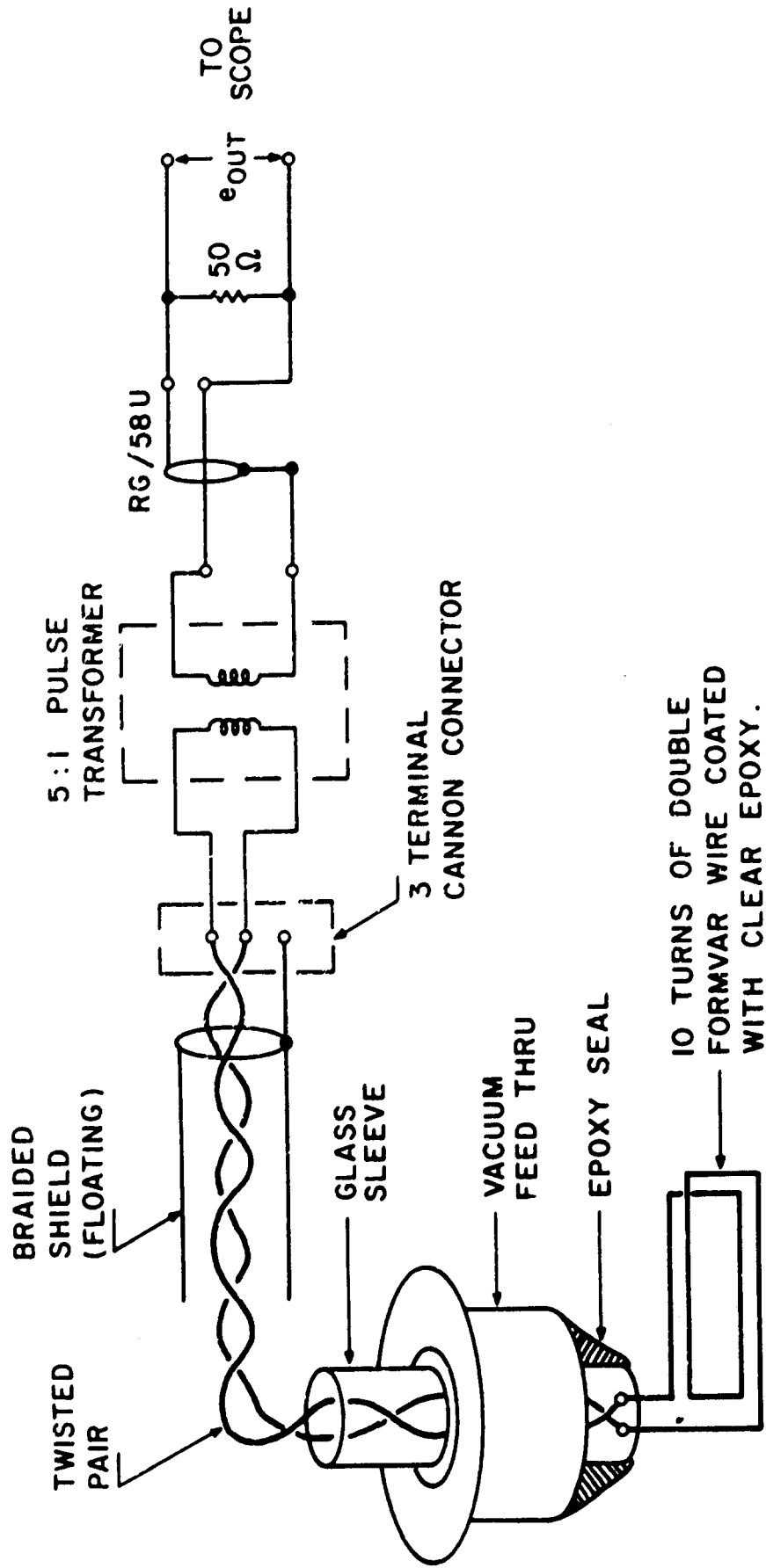
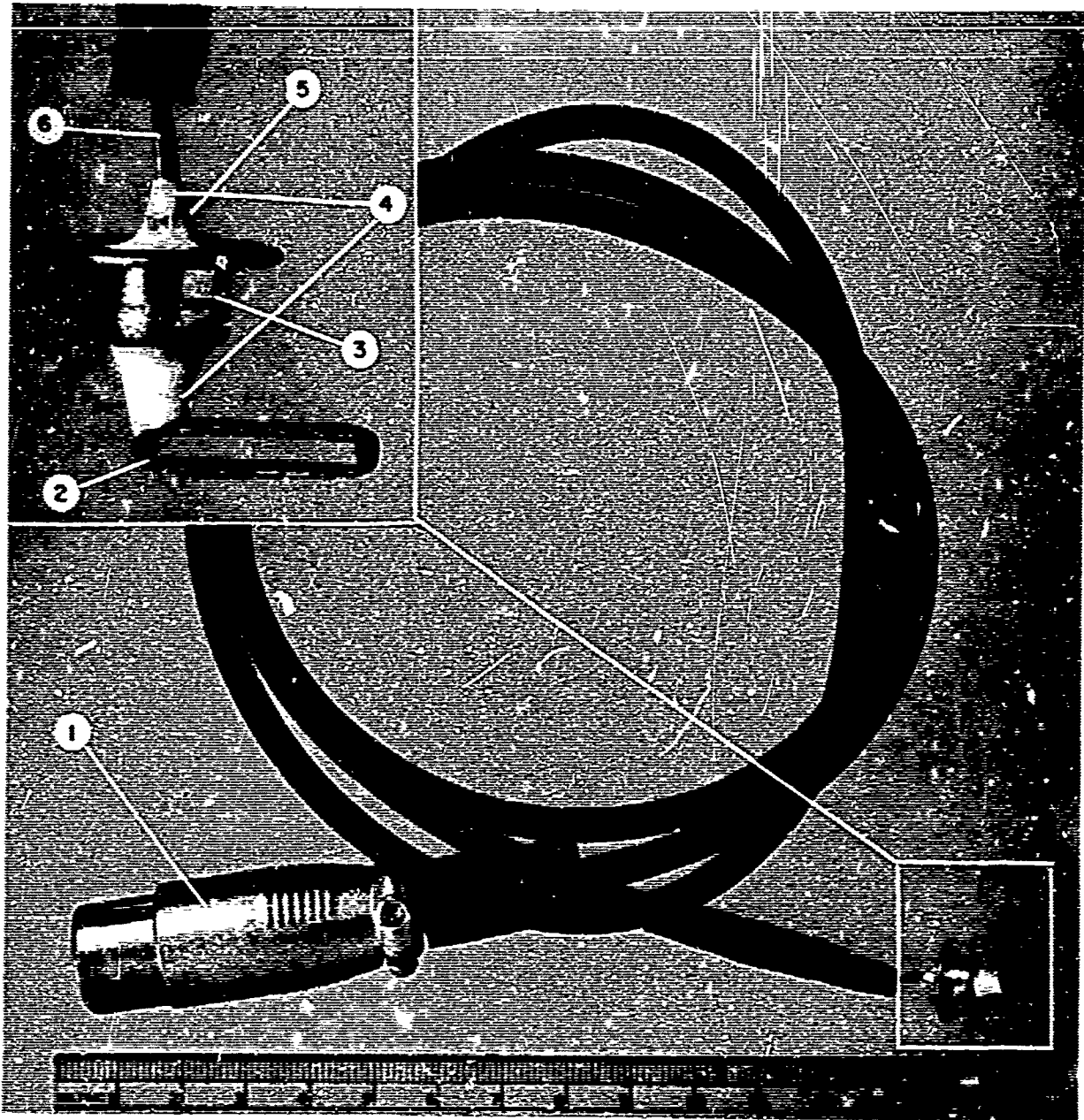
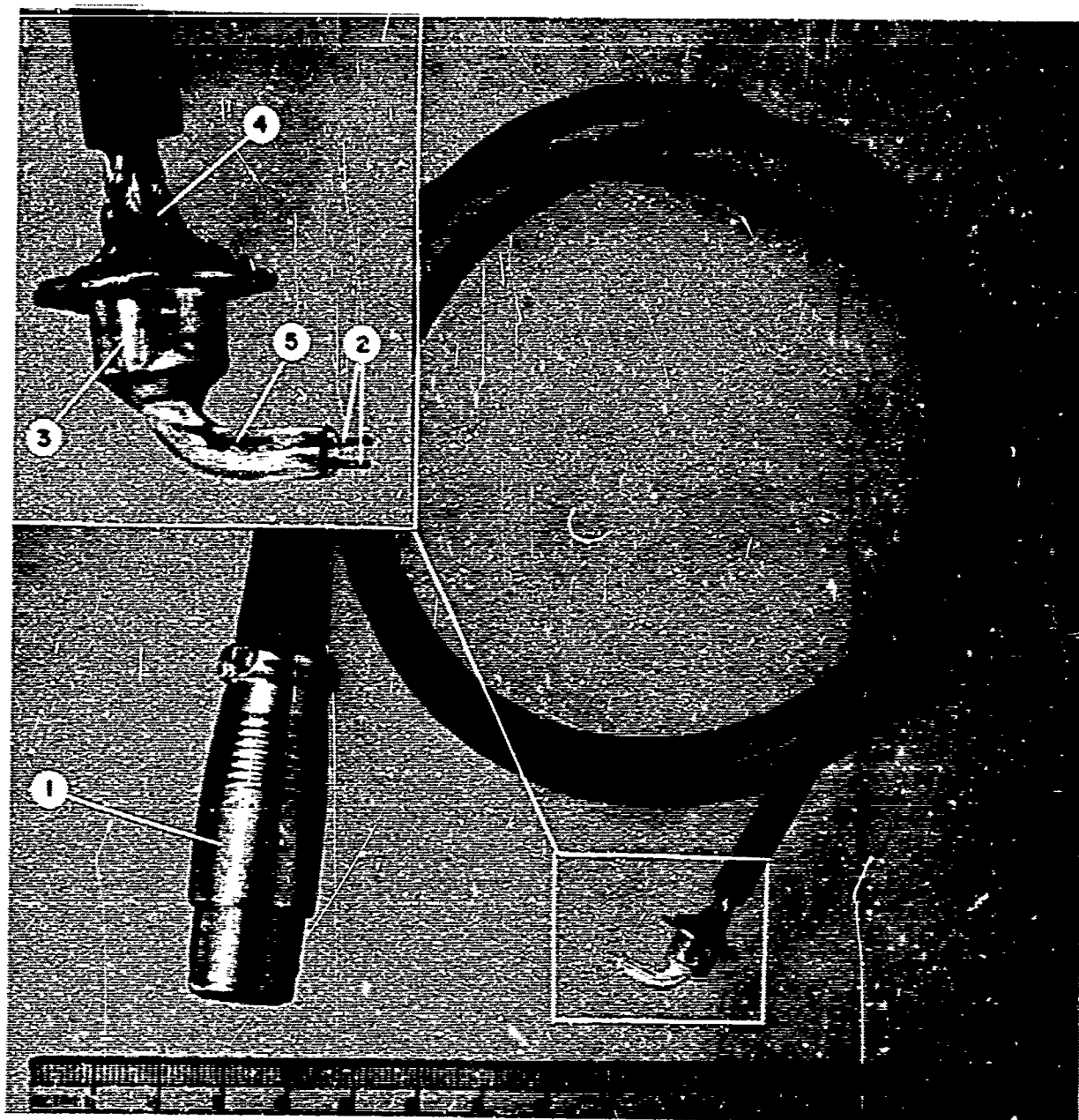


FIG.19 Bθ PROBE : SCHEMATIC AND CIRCUIT .



1. Cannon Connector
2. 10 Turn Probe-Epoxy Coated
3. Vacuum Feed Thru
4. Epoxy Seal
5. Glass Sleeve
6. Twisted Pair

FIG. 20 B<sub>9</sub> PROBE: CONSTRUCTION



1. Cannon Connector
2. Bare Wire Probe
3. Vacuum Feed Thru
4. Floating Braided Shield
5. Glass Sleeve

FIG. 21 ELECTRIC FIELD PROBE: CONSTRUCTION

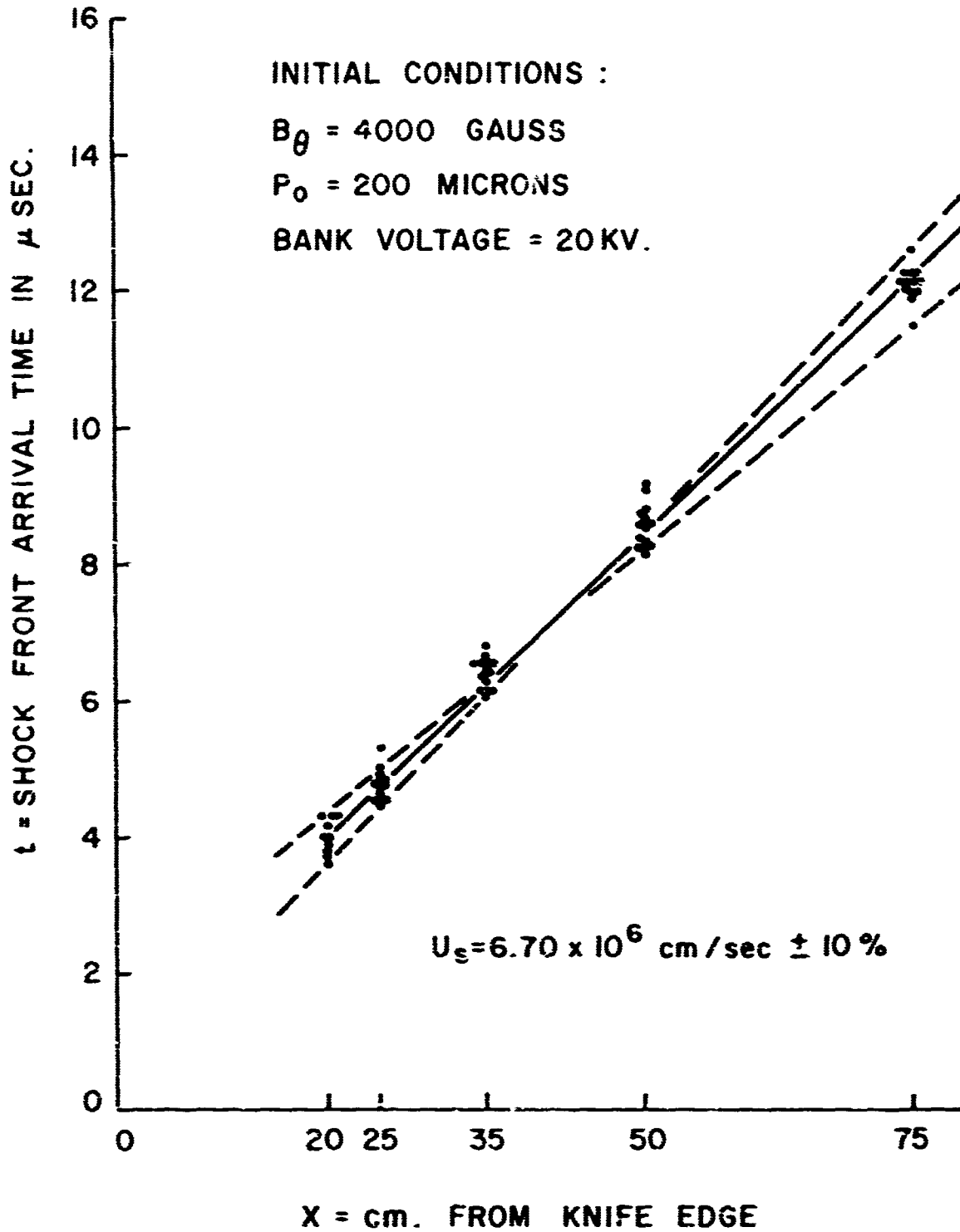
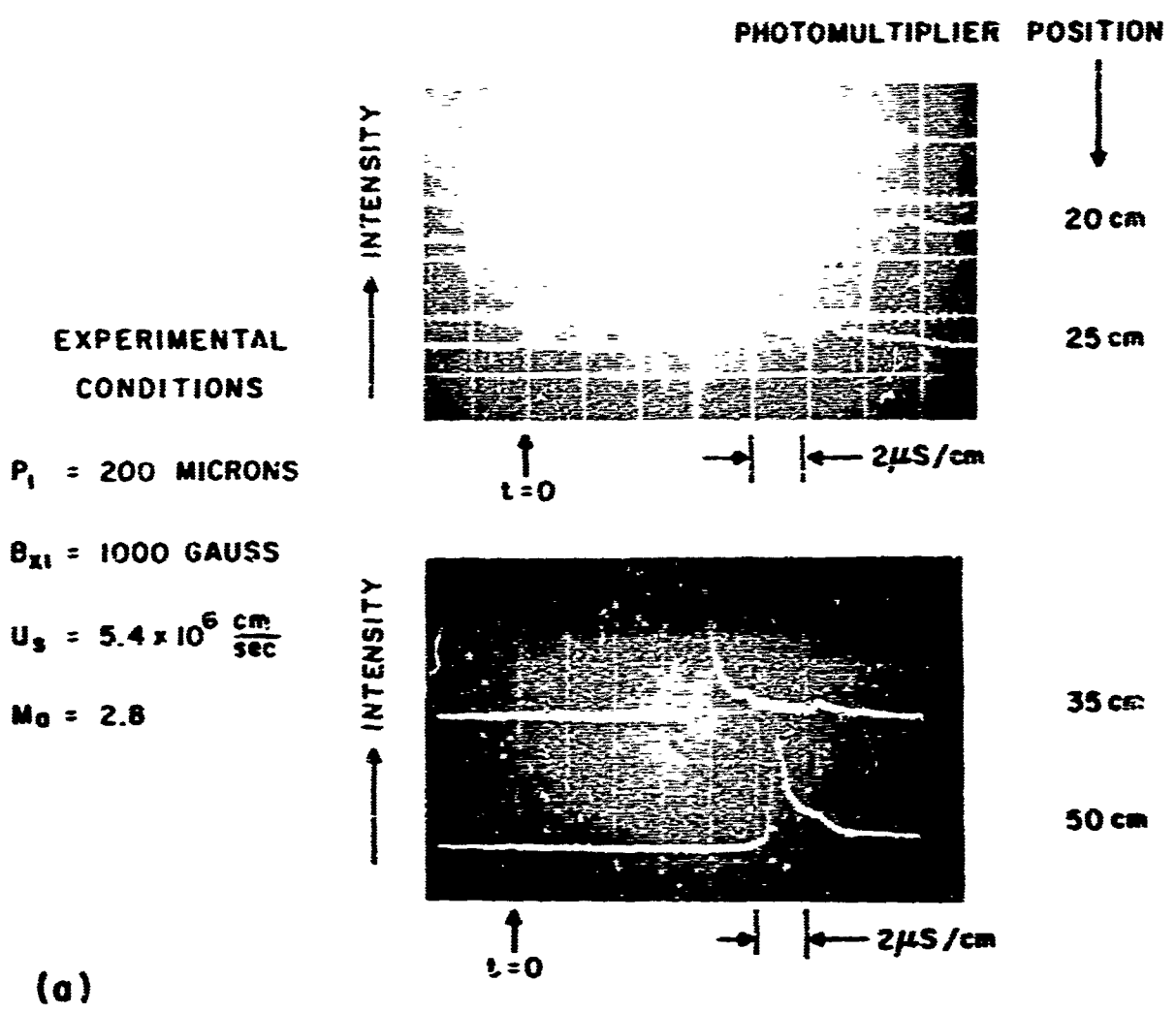
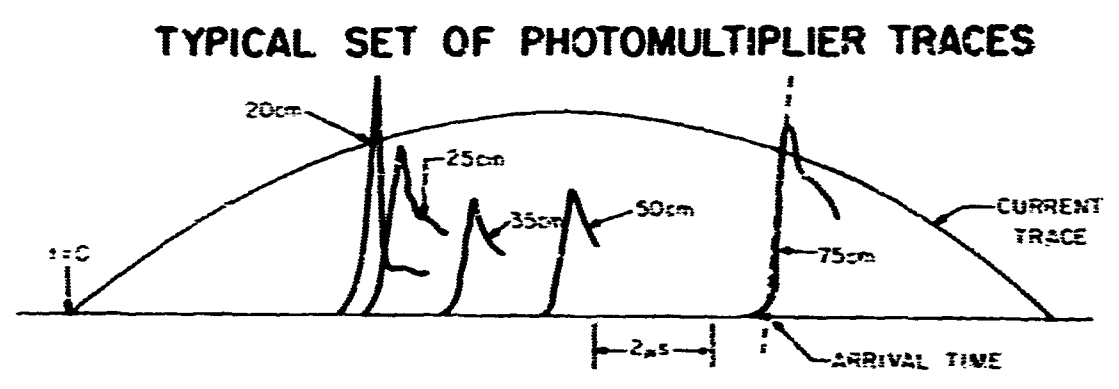


FIG. 22 X-t DIAGRAM FOR DETERMINATION OF SHOCK VELOCITY .

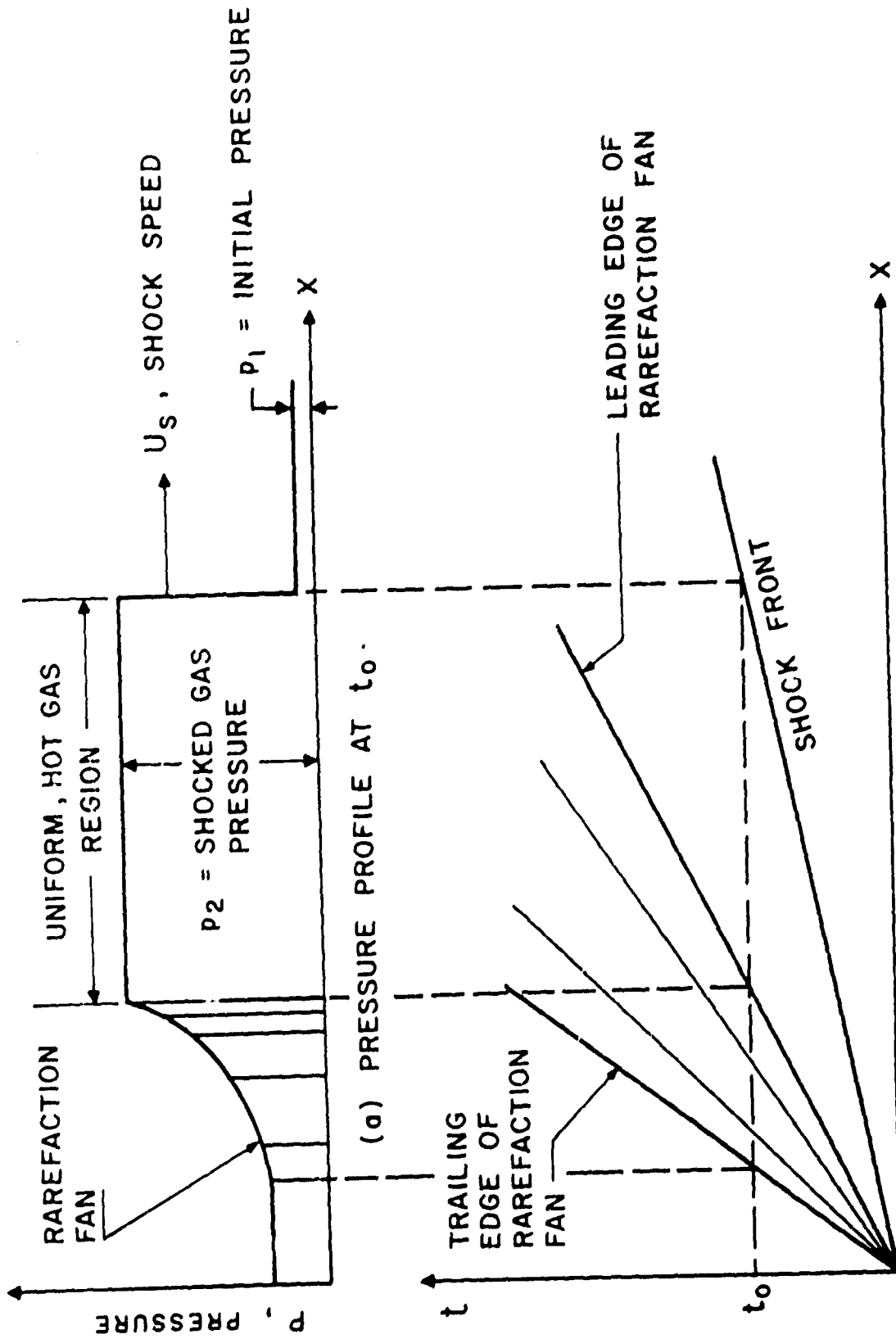


(a)



(b) CURRENT AND PHOTOMULTIPLIERS PROJECTED ON A COMMON TIME BASE

FIG. 23 ANALYSIS OF PHOTOMULTIPLIER DATA



(b) X - t DIAGRAM OF ELECTROMAGNETIC SHOCK TUBE

FIG. 24

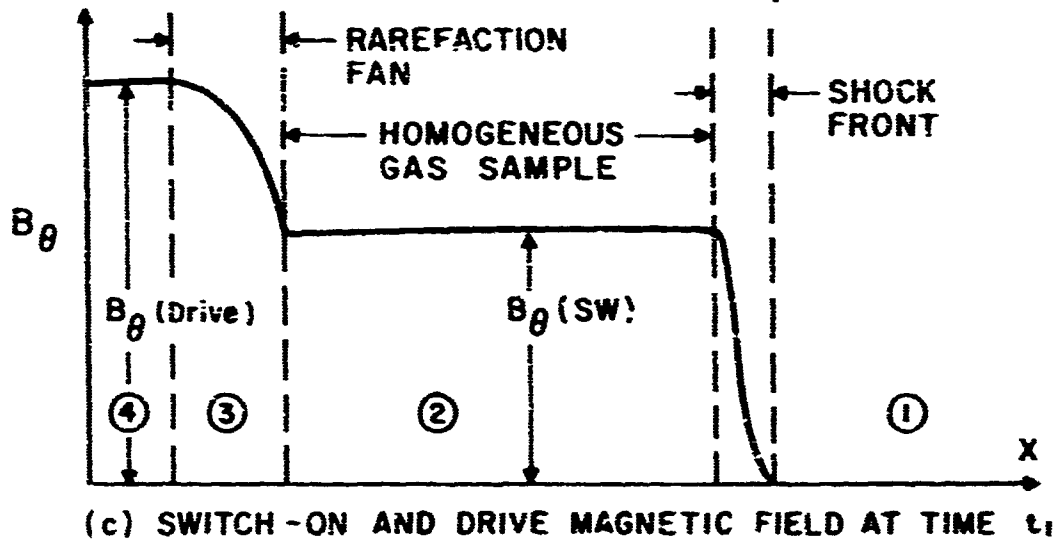
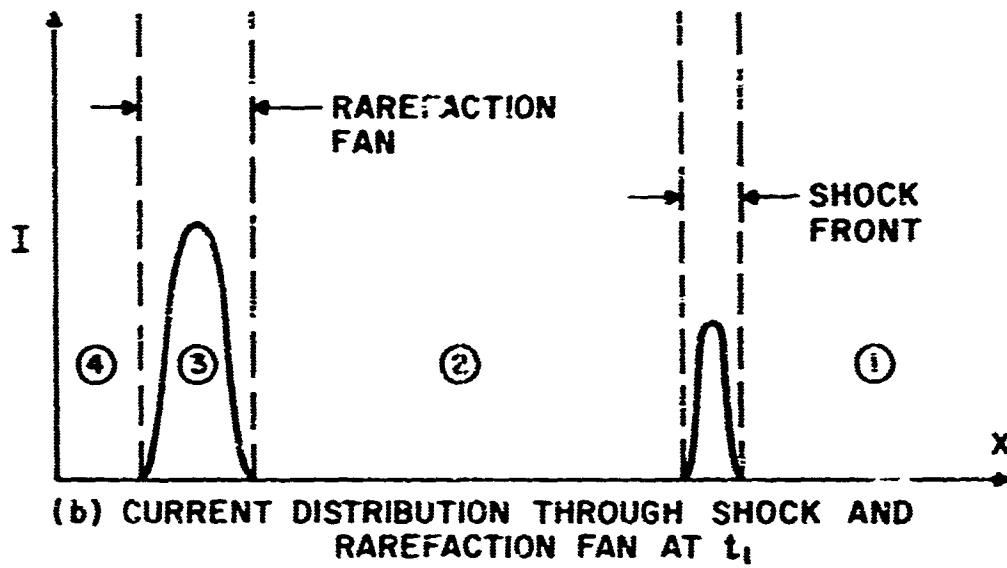
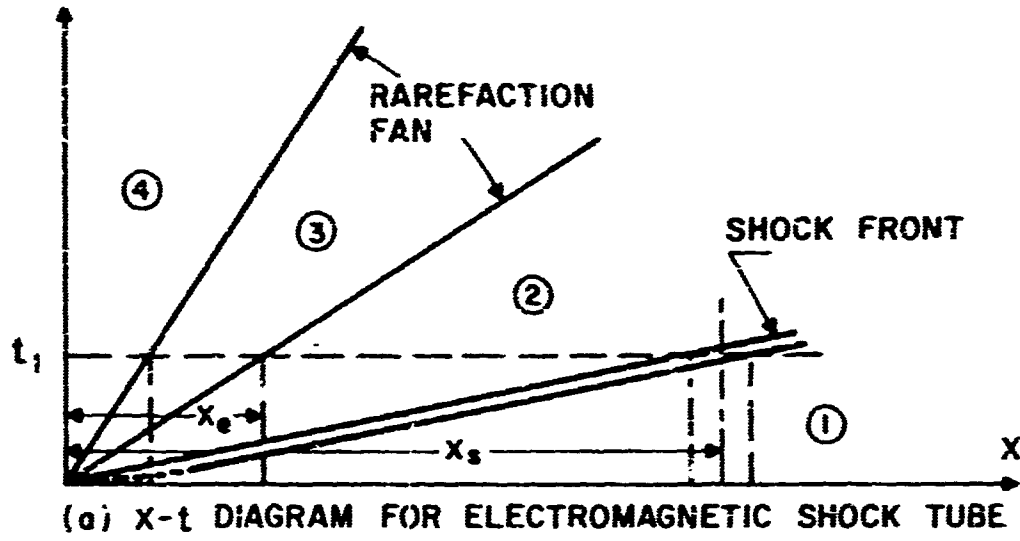


FIG. 25

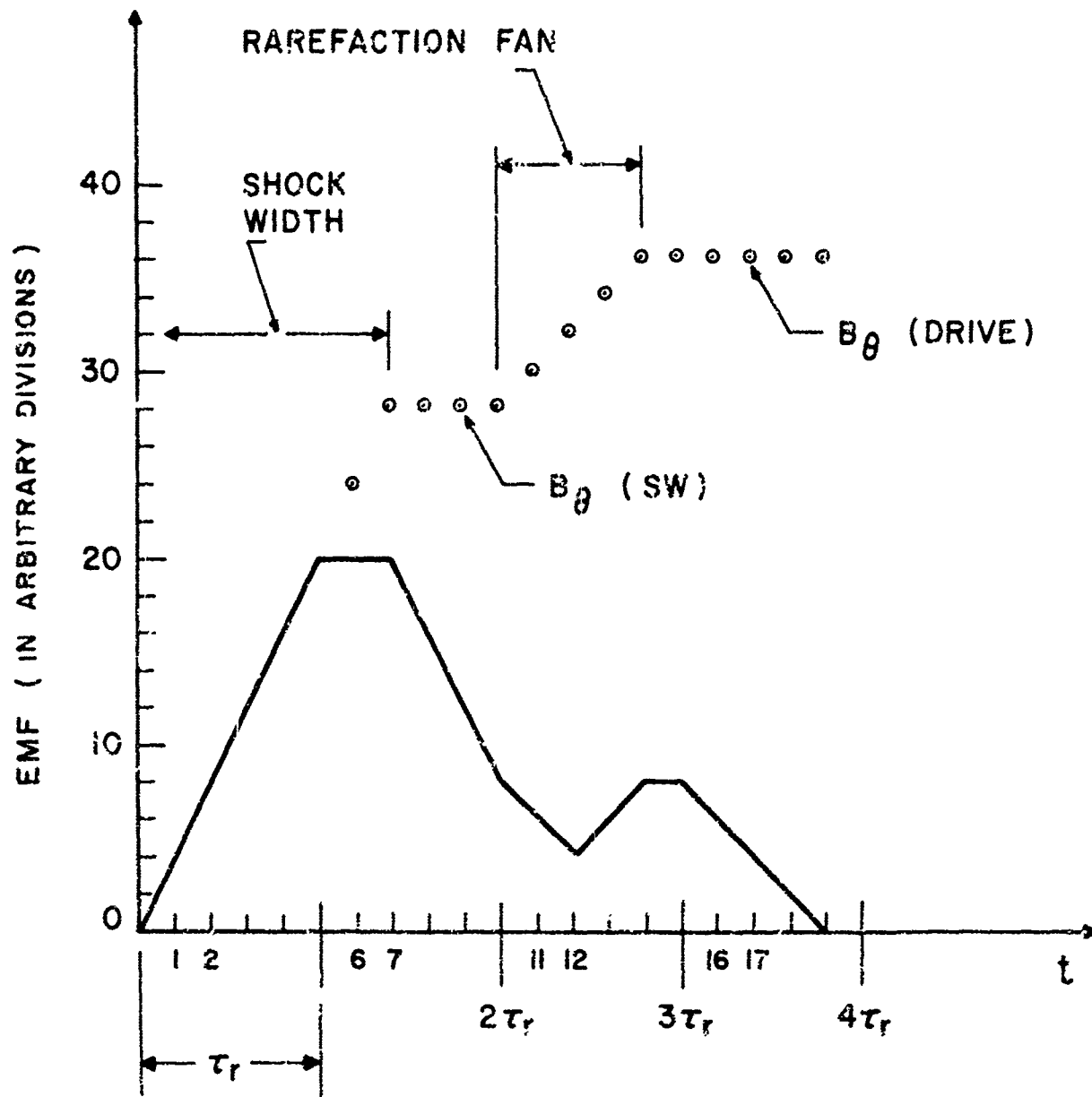
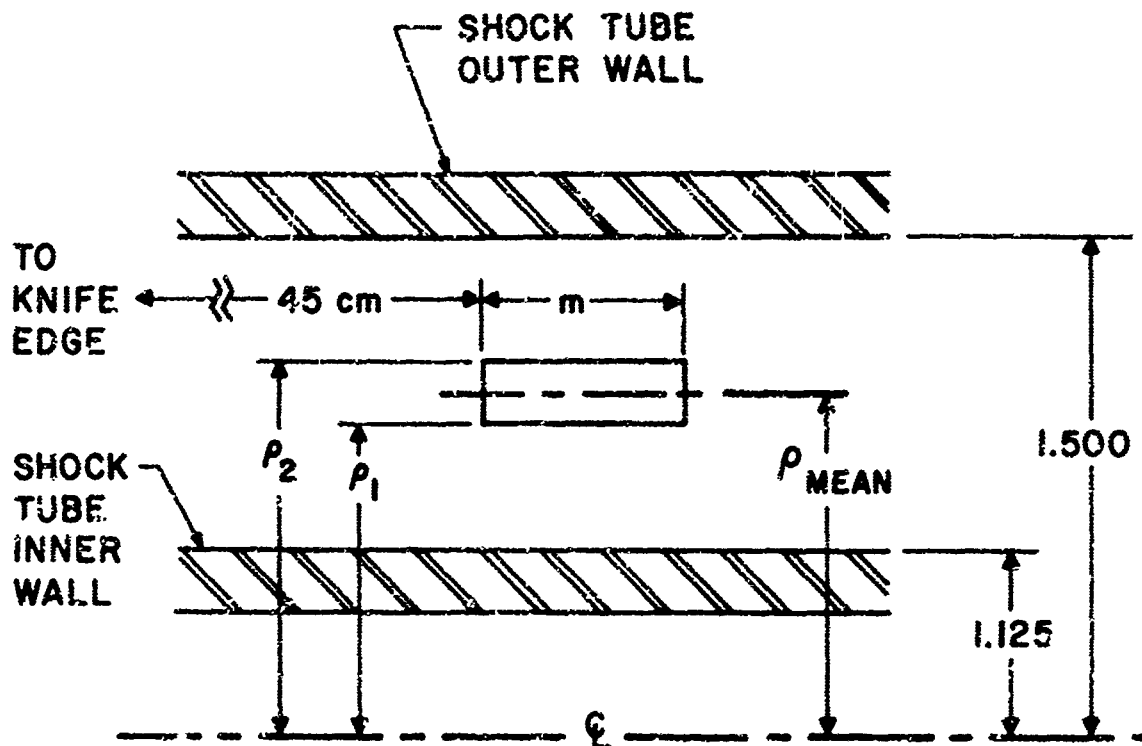


FIG.26 SAMPLE EMF &  $B_{\theta}$  DERIVED FROM IT



$$\rho_1 = 1.282 \text{ inches}$$

$$\rho_2 = 1.344 \text{ inches}$$

$$\rho_{MEAN} = .0334 \text{ meters.}$$

$$\ln \frac{\rho_2}{\rho_1} = .0486$$

$$\ln \left( \frac{\rho_2}{\rho_1} \right) \rho_{MEAN} = .00163 \text{ meters}$$

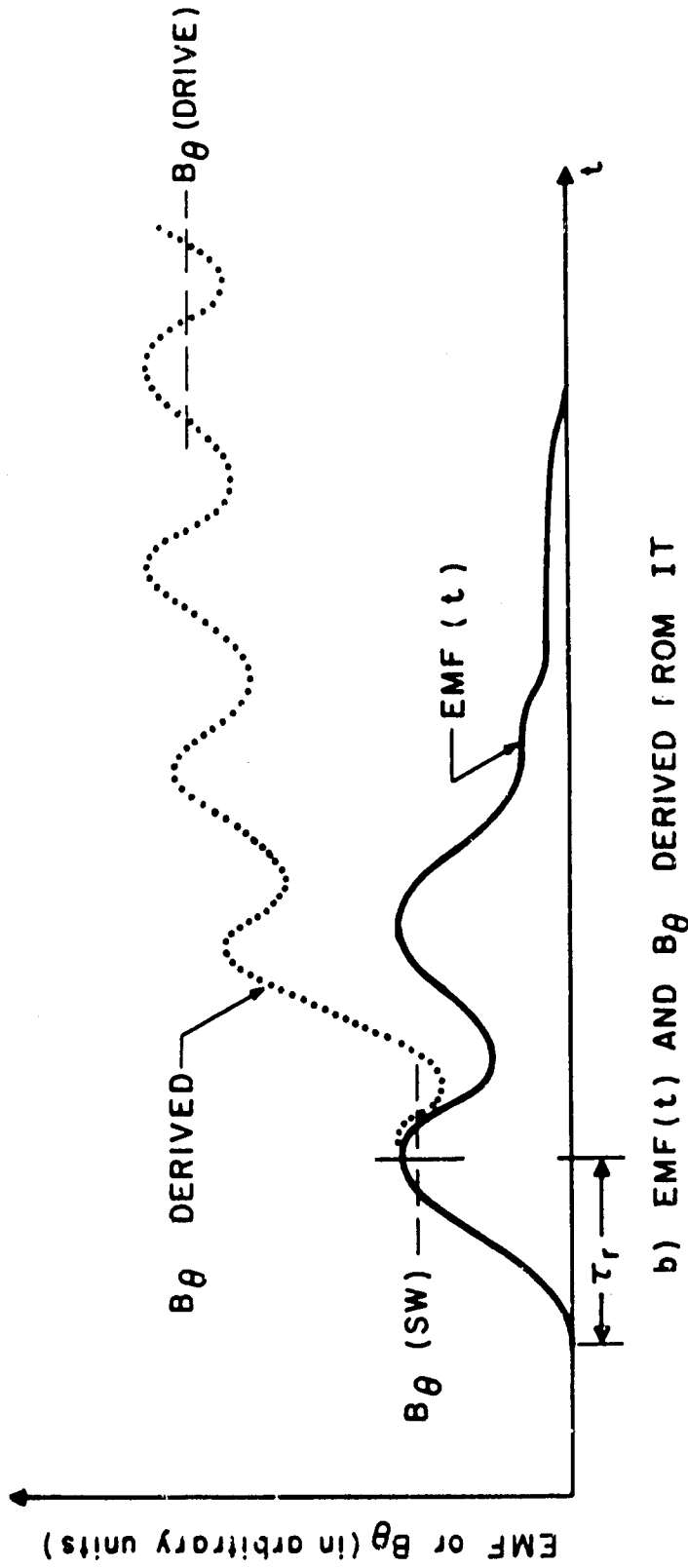
$$m = .01208 \text{ meters}$$

FIG.27 SINGLE TURN  $B_\theta$  PROBE GEOMETRY.

→ | ← .2 μSEC.



a) EXPERIMENTALLY OBSERVED EMF ( t )



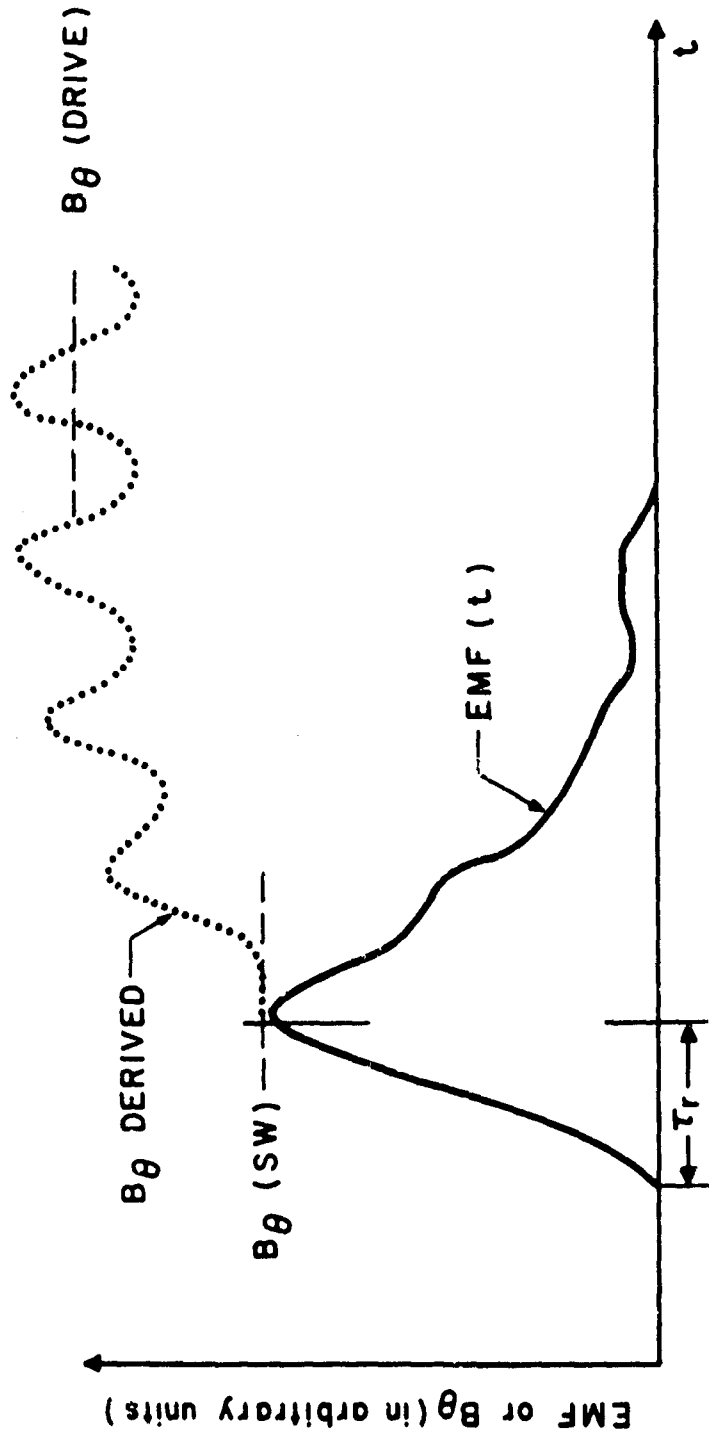
b) EMF(t) AND Bθ DERIVED FROM IT

FIG. 28 Bθ ANALYSIS: B<sub>XI</sub> = 4,000 gauss,  
 p<sub>I</sub> = 200μ, U<sub>S</sub> = 5.87 x 10<sup>6</sup> Cm/Sec



→ | ← .2 μSEC

a) EXPERIMENTALLY OBSERVED EMF (t)



b) EMF(t) AND  $B_\theta$  DERIVED FROM IT

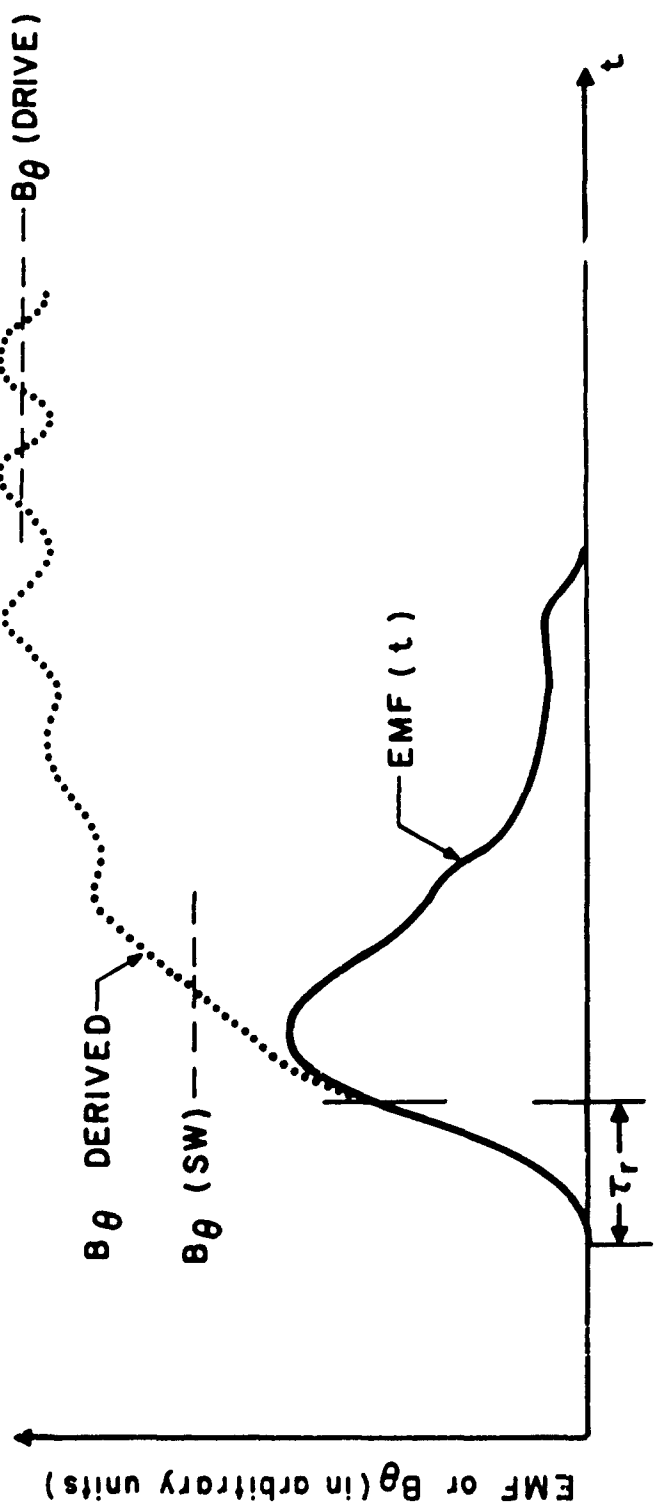
FIG. 29  $B_\theta$  ANALYSIS:  $B_{x1} = 1,500$  gauss,

$p_1 = 200\mu, U_s = 7.27 \times 10^6$  Cm/Sec



a) EXPERIMENTALLY OBSERVED EMF (t)

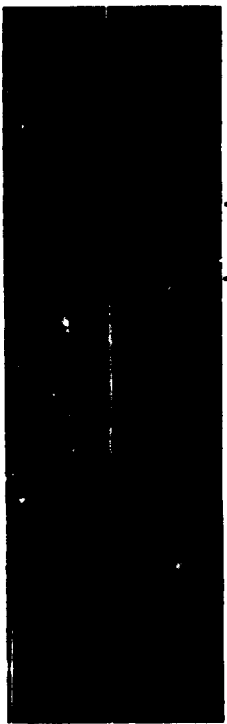
← .2 μSEC



b) EMF(t) AND  $B_\theta$  DERIVED FROM IT

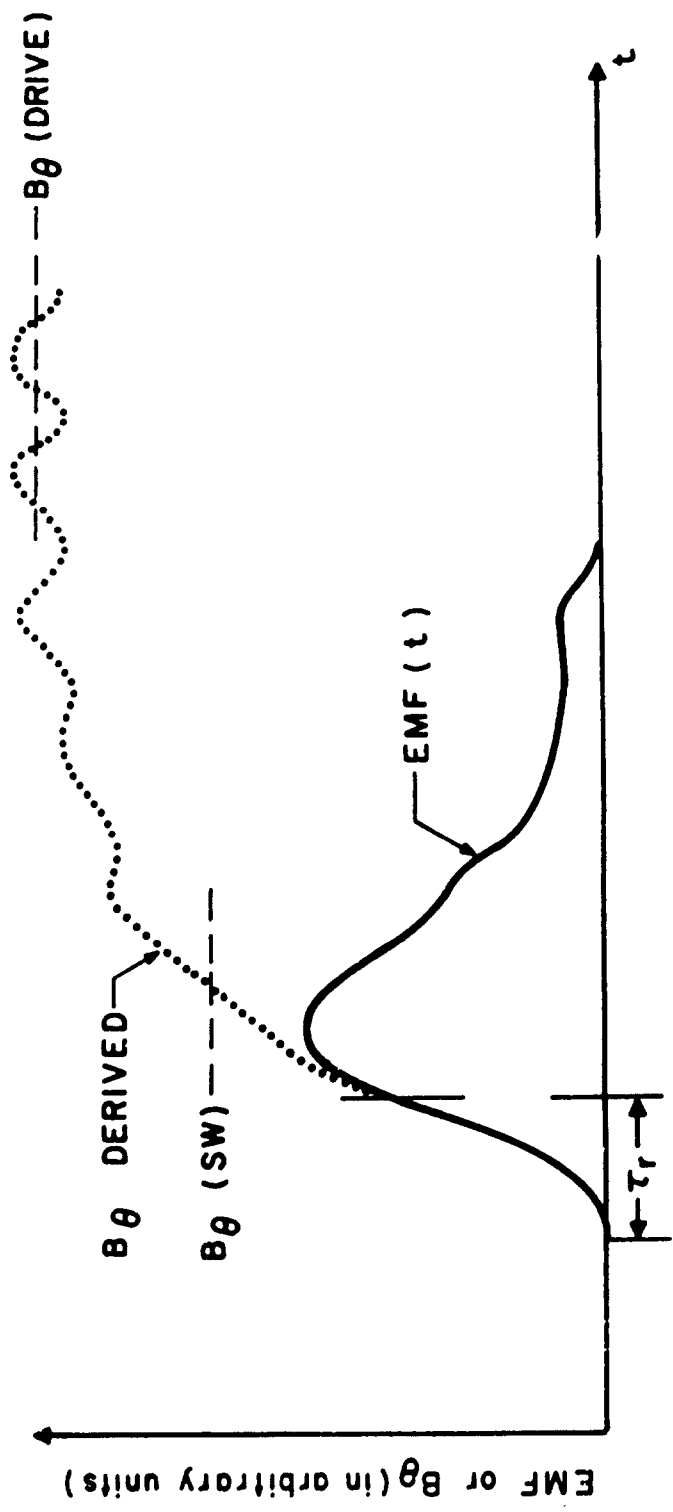
FIG. 30  $B_\theta$  ANALYSIS:  $B_{x1} = 1,500$  gauss,

$p_1 = 200\mu, U_s = 7.80 \times 10^6$  Cm/Sec



→ | ← .2 μSEC

a) EXPERIMENTALLY OBSERVED EMF (t)



b) EMF(t) AND B<sub>θ</sub> DERIVED FROM IT

FIG. 30 B<sub>θ</sub> ANALYSIS: B<sub>XI</sub> = 1,500 gauss,

p<sub>I</sub> = 200 μ, U<sub>S</sub> = 7.80 x 10<sup>6</sup> Cm/Sec

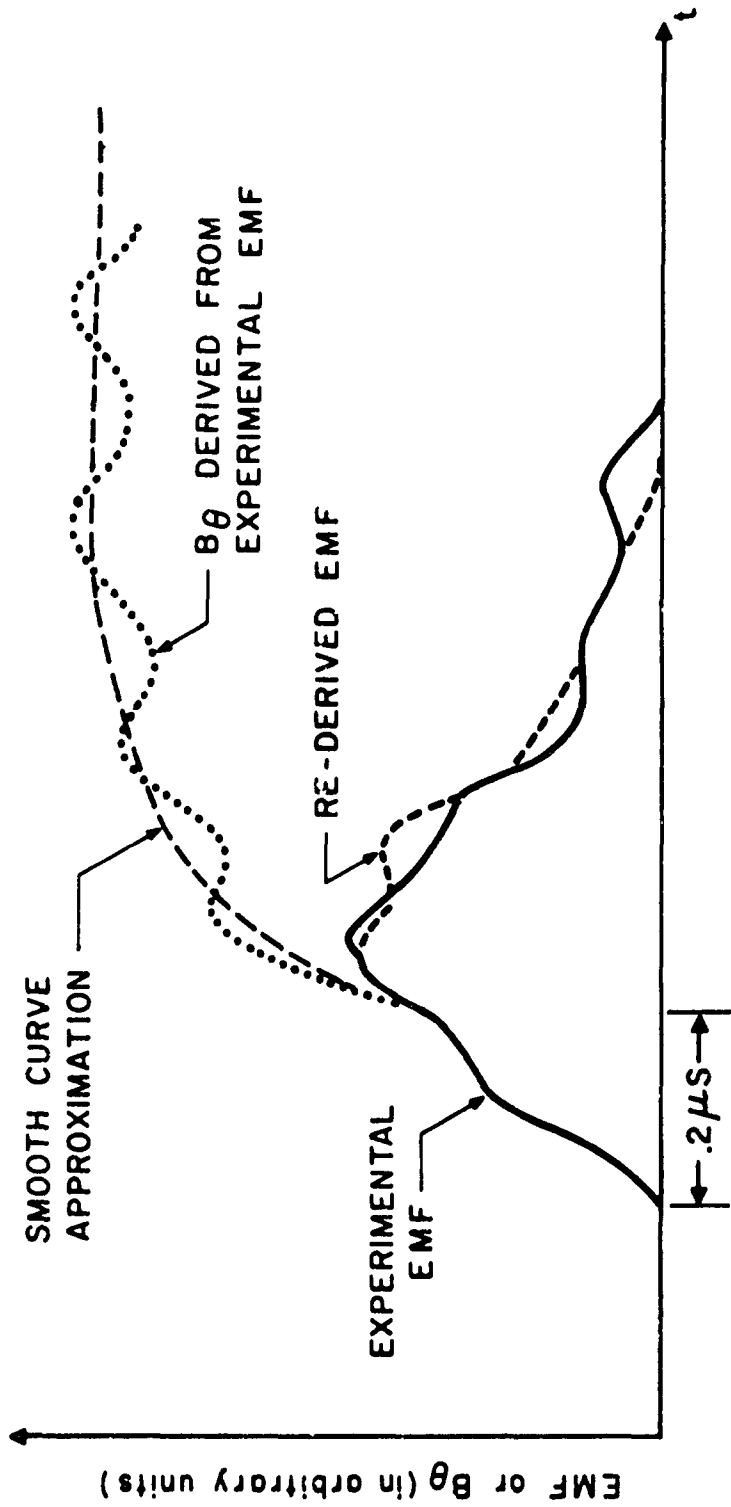


FIG.31  $B_\theta$  STRUCTURE STUDY

TABLE I

Run #	Capacitor Bank Voltage in Kilovolts	Initial Pressure, $P_1$ , in Microns of Hg of H <sub>2</sub>	Initial Axial Magnetic Field, $B_{x1}$ , in Gauss	Measured Shock Velocity, $U_s$ , in cm/ $\mu$ sec.	Alfven Mach Number, $M_a$	Sonic Mach Number, $M$
1	10	200	4000	5.60 $\pm$ 10%	.73	40
2	10	200	4000	5.87 $\pm$ 10%	.76	42
3	17	200	4000	6.70 $\pm$ 10%	.87	48
4	20	200	3000	7.05 $\pm$ 10%	1.22	50
5	20	200	2750	7.35 $\pm$ 10%	1.39	53
6	20	200	2750	7.90 $\pm$ 10%	1.50	56
7	20	200	2500	7.70 $\pm$ 10%	1.60	55
8	20	200	1900	6.90 $\pm$ 10%	1.89	49
9	20	200	2250	8.25 $\pm$ 10%	1.91	59
10	20	200	1500	7.27 $\pm$ 10%	2.52	52
11	20	200	1500	7.80 $\pm$ 10%	2.71	56

TABLE II

Instantaneous Total Current Through Shock Tube at the Time That the Shock Reaches the 45 Centimeter Port.

Run #	Capacitor Bank Voltage in Kilovolts	Initial Pressure, P <sub>1</sub> , in Microns of Hg of H <sub>2</sub>	Initial Axial Magnetic Field, B <sub>x1</sub> , in Gauss	Current, I(t), Through Shock Tube in amperes × 10 <sup>5</sup>
1	10	200	4000	.341 ± .03
2	10	200	4000	.335 ± .03
3	17	200	4000	.578 ± .03
4	20	200	3000	.675 ± .03
5	20	200	2750	.714 ± .03
6	20	200	2750	.701 ± .03
7	20	200	2500	.706 ± .03
8	20	200	1900	.708 ± .03
9	20	200	2250	.679 ± .03
10	20	200	1500	.665 ± .03
11	20	200	1500	.681 ± .03

L

TABLE III

Run #	Capacitor Bank Voltage in Kilovolts	Initial Pressure, P <sub>1</sub> , in Microns of Hg of H <sub>2</sub>	Initial Axial Magnetic Field, B <sub>x1</sub> , in Gauss	Alfven Mach #, M <sub>a</sub>	B <sub>θ</sub> (SW) in Gauss	B <sub>θ</sub> (drive) in Gauss	$\frac{X_e}{X_s}$
1	10	200	4000	.73	811 ± 280	1700 ± 410	.984 ± .310
2	10	200	4000	.76	714 ± 180	1630 ± 260	.983 ± .180
3	17	200	4000	.87	644 ± 160	2080 ± 370	.987 ± .360
4	20	200	3000	1.22	1520 ± 260	2320 ± 370	.984 ± .400
5	20	200	2750	1.39	2100 ± 420	3040 ± 400	.988 ± .440
6	20	200	2750	1.50	1830 ± 400	2620 ± 500	.991 ± .390
7	20	200	2500	1.60	1960 ± 260	2500 ± 530	.988 ± .320
8	20	200	1900	1.89	1814 ± 540	2102 ± 357	.988 ± .270
9	20	200	2250	1.91	2530 ± 350	3570 ± 390	.990 ± .330
10	20	200	1500	2.52	2920 ± 350	3800 ± 530	.986 ± .260
11	20	200	1500	2.71	3150 ± 500	3980 ± 560	.987 ± .450

TABLE IV

GENERAL STATISTICS			COMPARISON BETWEEN THEORY AND EXPERIMENT				ELECTRIC FIELD AT FOUR END POINT (BRACKET POINT FOR RUNS 10 and 11) in volts/cm				
Run #	Capacitor Bank Voltage in Kilovolts	Initial Axial Magnetic Field in Gauss	$B_z$ (SW) in Gauss	$B_p$ (Drive) in Gauss	$X_c/X_s$	$I(t)$ in amperes $\times 10^5$					
			Experiment	Theory*	Experiment	Theory*					
1	10	4000	811 $\pm$ 280	1430 $\pm$ 260	1700 $\pm$ 410	1680 $\pm$ 350	.984 $\pm$ .310	.940 $\pm$ .040	.341 $\pm$ .03	.325 $\pm$ .070	108 $\pm$ 2
2	10	4000	714 $\pm$ 180	1540 $\pm$ 280	1630 $\pm$ 260	1840 $\pm$ 400	.983 $\pm$ .180	.970 $\pm$ .001	.335 $\pm$ .03	.356 $\pm$ .080	109 $\pm$ 1
3	17	4000	644 $\pm$ 160	1900 $\pm$ 280	2080 $\pm$ 370	2400 $\pm$ 480	.987 $\pm$ .360	.950 $\pm$ .001	.578 $\pm$ .03	.465 $\pm$ .093	106 $\pm$ 3
4	20	3000	1520 $\pm$ 260	2130 $\pm$ 150	2320 $\pm$ 370	3360 $\pm$ 570	.984 $\pm$ .400	.986 $\pm$ .006	.675 $\pm$ .03	.650 $\pm$ .100	46.0 $\pm$ 7.5
5	20	2750	2100 $\pm$ 420	2080 $\pm$ 60	3040 $\pm$ 400	3740 $\pm$ 550	.988 $\pm$ .440	.990 $\pm$ .002	.714 $\pm$ .03	.724 $\pm$ .106	29.4 $\pm$ 7.2
6	20	2750	1830 $\pm$ 400	2120 $\pm$ 70	2620 $\pm$ 500	4180 $\pm$ 600	.991 $\pm$ .390	.995 $\pm$ .002	.701 $\pm$ .03	.808 $\pm$ .120	23.1 $\pm$ 8.7
7	20	2500	1960 $\pm$ 260	1900 $\pm$ 75	2500 $\pm$ 530	4150 $\pm$ 550	.988 $\pm$ .320	.995 $\pm$ .002	.706 $\pm$ .03	.803 $\pm$ .110	14.3 $\pm$ 7.3
8	20	1900	1810 $\pm$ 540	933 $\pm$ 437	2100 $\pm$ 360	3920 $\pm$ 80	.988 $\pm$ .270	.995 $\pm$ .001	.708 $\pm$ .03	.756 $\pm$ .016	1.32 $\pm$ 76.2
9	20	2250	2530 $\pm$ 350	1010 $\pm$ 740	3570 $\pm$ 390	4700 $\pm$ 600	.970 $\pm$ .330	.995 $\pm$ .001	.679 $\pm$ .03	.910 $\pm$ .015	1.36 $\pm$ 110.
10	20	1500	2920 $\pm$ 350	3990 $\pm$ 470	3900 $\pm$ 530	4010 $\pm$ 480	.986 $\pm$ .260	.573 $\pm$ .008	.665 $\pm$ .03	.772 $\pm$ .092	81.0 $\pm$ 22.0
11	20	1500	3150 $\pm$ 500	4320 $\pm$ 540	3940 $\pm$ 560	4380 $\pm$ 500	.997 $\pm$ .450	.618 $\pm$ .047	.681 $\pm$ .03	.944 $\pm$ .094	95.0 $\pm$ 28.0

\* The error assigned to each theoretical value was obtained by varying the central theoretical value by  $\pm 10\%$ . This was done to account for the  $\pm 10\%$  uncertainty in the measured shock velocity.

## 7. Appendices

### 7.1 APPENDIX A

#### ANALYSIS OF THE CAPACITOR-INDUCTOR BANK WHEN USED AS A SQUARE-PULSE CURRENT GENERATOR

To generate an MHD shock wave in a co-axial shock tube, it is desirable to have a source of electrical energy capable of producing a square, high-current pulse of 10-20  $\mu$ sec duration.

The simplest arrangement consists of capacitors and inductors arranged in a low-pass filter geometry (Fig. A1).

This set-up simulates an open-ended transmission line with an input-impedance of  $\sqrt{\frac{L}{C}}$  and a characteristic discharge time  $\tau = 2n\sqrt{LC}$ .

To see how this design is related to the desired square-pulse shape, we first investigate the transient properties of transmission lines and the properties of the pulse-forming networks derived from them.

The usual approach to this problem is from the Laplace transform viewpoint.

Consider first the circuit in Fig. A2. Kirchoff's Law requires that at any time after the switch, S, is closed

$$i(t)Z_N + iR_L + \frac{\int i dt}{C_N} = 0 \quad (A1)$$

Multiplying (1) by  $e^{-pt}$  and  $\int_0^{\infty} (\quad) dt$  we get

$$Z_N \int_0^{\infty} i(t) e^{-pt} dt + R_L \int_0^{\infty} i(t) e^{-pt} dt + \frac{1}{C_N} \int_0^{\infty} \left( \int_0^t i dt \right) e^{-pt} dt = 0. \quad (A2)$$

Defining:  $i(p) \equiv \int_0^{\infty} i(t) e^{-pt} dt$ , we get

$$i(p)R_L + i(p)Z_N + \frac{1}{C_N} \int_0^{\infty} \int_0^t i dt e^{-pt} dt = 0. \quad (A3)$$

From Goldman, Transf. Calc. and Elec. Trans., Prentice-Hall, Inc., 1949, pg. 61, we have

$$\int_0^{\infty} \int_0^t f dt e^{-pt} dt = \frac{F(s)}{s} + \frac{f^{-1}(0^+)}{s}$$

where

$$F(s) \equiv \int_0^{\infty} f(t) e^{-st} dt$$

$$f^{-1}(t) \equiv \int_0^t f(t) dt.$$

We now have (3) in the form

$$\left( R_L + Z_N + \frac{1}{C_N p} \right) i(p) = - \frac{q(0^+)}{C_N p} \quad (A4)$$

where  $q(0^+)$  is the charge on the capacitor  $C_N$  before the switch is closed. Since  $-\frac{q(0^+)}{C_N} = -V_N =$  initial potential drop across the capacitor we can write (4) as

$$\left( R_L + Z_N + \frac{1}{C_N p} \right) i(p) = - \frac{V_N}{p} = \frac{V_0}{p} \quad (A5)$$

where

$$V_0 \equiv -V_N,$$

and  $Z_N$  is the network impedance (which will be a function, as yet unknown, of the Laplace parameter  $p$ ).

Let us now require that the discharge current-pulse shape be a single square-pulse of duration  $\tau$  and magnitude  $I$ , i.e.,

$$\begin{aligned} i(t) &= I & 0 \leq t \leq \tau \\ i(t) &= 0 & t < 0; \tau < t < \infty. \end{aligned}$$

From the definition of the Laplace transform for  $i(t)$  we get

$$i(p) = \frac{I}{p}(1 - e^{-p\tau}).$$

Substituting this expression into (5) and solving for  $(Z_N + \frac{1}{C_N p})$

$$Z_N + \frac{1}{C_N p} = R_L \frac{[\frac{V_0}{IR_L} - 1 + e^{-p\tau}]}{(1 - e^{-p\tau})} \quad (A6)$$

which can be put into the form

$$Z_N + \frac{1}{C_N p} = R_L \left[ \coth \frac{p\tau}{2} + \frac{\frac{V_0}{IR_L} - 2}{e^{\frac{p\tau}{2}} - e^{-\frac{p\tau}{2}}} \right] \quad (A7)$$

by multiplying (6) through by  $e^{\frac{p\tau}{2}}$  in the numerator and denominator.

If we now choose  $V_0 = 2IR_L$  then

$$Z_N + \frac{1}{C_N p} = R_L \coth \frac{p\tau}{2} \quad (A8)$$

which is just the Laplace impedance function for an open-ended

lossless transmission line of characteristic impedance  $Z_0 = R_L$ , and one way transmission time  $\delta = \frac{\tau}{2}$ .

Thus if we want a square voltage (or current) pulse of duration  $\tau$  developed across the resistor  $R_L$  we can replace  $Z_N + \frac{1}{C_N p}$  by an open-ended transmission line with  $Z_0 = R_L$ .

Utilizing this result we return to (5) and substitute  $Z_N + \frac{1}{C_N p} = Z_0 \coth p\delta$ , hereby hoping to investigate the effects of a transmission line discharging through a resistor where  $Z_0$  may or may not match  $R_L$ .

From (5) we solve now for  $i(p)$  and get

$$i(p) = \frac{V_0}{p(R_L + Z_0 \coth p\delta)} \quad (A9)$$

Expanding the expression,

$$i(p) = \frac{V_0 (1 - e^{-2p\delta})}{p(Z_0 + R_L)} \left[ 1 - \frac{(Z_0 - R_L)}{(Z_0 + R_L)} e^{-2p\delta} + \left( \frac{Z_0 - R_L}{Z_0 + R_L} \right)^2 e^{-4p\delta} - \dots \right] \quad (A10)$$

and inverting this (from tables)

$$i(t) = \frac{V_0}{Z_0 + R_L} \left\{ 1 - U(t - 2\delta) - \left[ \frac{Z_0 - R_L}{Z_0 + R_L} \right] [U(t - 2\delta) - U(t - 4\delta)] + \left[ \frac{Z_0 - R_L}{Z_0 + R_L} \right]^2 [U(t - 4\delta) - U(t - 6\delta)] - \dots \right\} \quad (A11)$$

where  $U(\Delta t) = 1$  for  $\Delta t > 0$   
 $U(\Delta t) = 0$  for  $\Delta t < 0$  and  $\Delta t = (t - n\delta)$ .

For  $R_L = Z_0$  we get contributions to  $i(t)$  from only the first two terms of (11) and

$$i(t) = \frac{V_0}{2R_L} \left[ 1 - U(t-2\delta) \right] \quad (A12)$$

which is a simple rectangular pulse of duration  $\tau = 2\delta$ . Mismatching the load gives rise to contributions from succeeding terms in (11) and therefore, effectively, we get reflections at the load (see Glascoe and Lebacqz, Pulse Generators, McGraw-Hill, 1948, p. 178).

Recognizing the advantages inherent in the transmission line approach we inquire if we can design a line to generate a 20  $\mu$ sec pulse. For  $\tau = 20 \mu$ sec,  $\delta = \frac{\tau}{2} =$  transmission time = 10  $\mu$ sec. For a representative signal velocity on the line of 500 ft/ $\mu$ sec we would need a line of length  $L = 500 \text{ ft}/\mu\text{sec} \times 10 \mu\text{sec} = 5000 \text{ ft}$ , an unweildy laboratory dimension.

It is apparent that we can only shorten the line length needed if we use a lumped-parameter network, where we get high-voltage stability and can use large circuit parameters. In this process we will lose our precision square pulse characteristic and the departure from "squareness" will be larger the more we make our network depart from the distributed parameter model.

Our discussion will now be centered upon analyzing the network of Fig. A1. If we connect our "bank" to a battery we have Fig. A3.

Solving this for the mesh currents, we get  $n$  difference transform equations, the general one (except first and last) being of the form:

$$-\frac{i_{r-1}(p)}{C_p} + (L_p + \frac{2}{C_p}) i_r(p) - \frac{i_{r+1}(p)}{C_p} = 0. \quad (A13)$$

The general solution to this equation is

$$i_r(p) = Ae^{r\theta} + Be^{-r\theta} \quad (A14)$$

where A and B are arbitrary constants. Substitution back into (i3) yields the condition

$$\cosh \theta = 1 + \left(\frac{LC}{2}\right)p^2. \quad (A15)$$

If we solve for A and B by considering the first and last mesh, we can derive the input impedance transform for the network which is

$$Z_i(p, n) = \frac{V_N}{pi_1(p)} = \frac{1}{Cp} \left[ \frac{\sinh(n+1)\theta}{\sinh(n\theta)} - 1 \right]. \quad (A16)$$

If we now include a resistor  $R_L = \sqrt{\frac{L}{C}}$  in the circuit of Fig. C between the battery and the first inductor we will have the general case of a lumped-parameter line terminated in a matching impedance. The input impedance transform for such a circuit is simply  $\sqrt{\frac{L}{C}} + Z_i(p, n)$  and we get immediately from the form of (16) that in this case

$$\begin{aligned} i_1(p) &= \frac{V_N/p}{\sqrt{\frac{L}{C}} + \frac{1}{Cp} \left[ \frac{\sinh(n+1)\theta}{\sinh(n\theta)} - 1 \right]} \\ &= \frac{CV_N}{p\sqrt{LC} + \left[ \right]}. \end{aligned} \quad (A17)$$

But from  $\cosh \theta = 1 + \left(\frac{LC}{2}\right)p^2$  we have

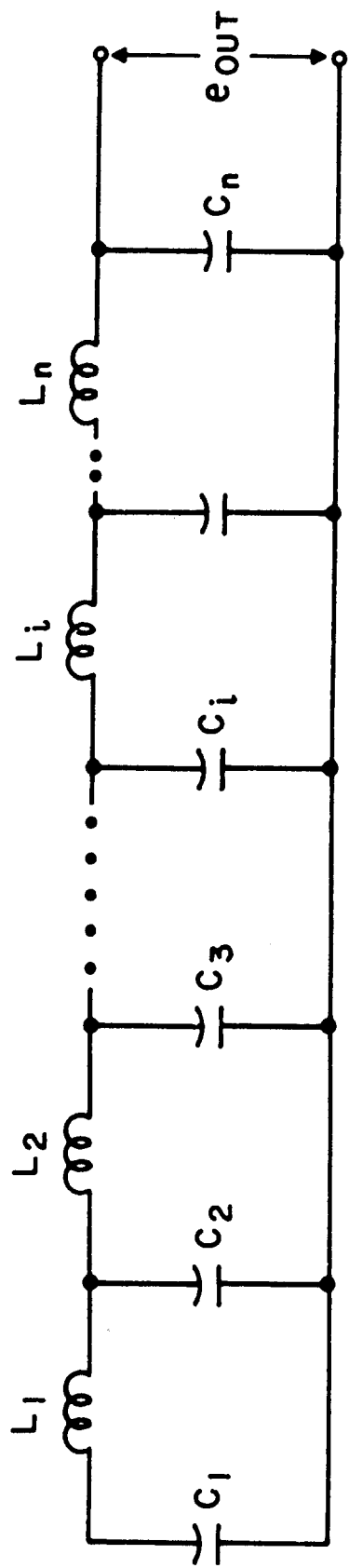
$$p = \frac{2}{\sqrt{LC}} \sinh \frac{\theta}{2} \quad (A18)$$

and substituting this into (17) we get the general current transform through a matched load connected to a lumped parameter transmission line,

$$i_1(p) = CV_N \frac{\sinh n\theta}{\sinh(n+1)\theta + (2 \sinh \frac{\theta}{2} - 1) \sinh n\theta} \cdot \quad (A19)$$

When inverted this gives  $i_1(t)$  as the desired result. However, in general, this is difficult to do and usually requires machine calculations. When  $n = 5$  and  $R_L = \frac{L}{C}$  this has been done and is discussed by Glascoe and Lebacqz, op. cit. p. 183, along with oscilloscope traces showing the square character of the charging pulse.

Although  $n = 5$  does not give a particularly good pulse shape the principle when extended to larger  $n$  will give increasingly better results. If now, instead of restricting the bank geometry to the low pass filter form, one looks for systems that give overall better performance in terms of rise-time and flatness, one finds that the Type C Guillemin network strikes an excellent balance between performance, simplicity and ease of assembly. Without belaboring the point (all the details can be found in Glascoe and Lebacqz), it is sufficient to note that the capacitors in the four meshes are not identical. As Fig. ( 8 ) shows,  $C_1 > C_2 > C_3 > C_4$ . Physically this means that when a switch between bank and load is "closed" most of the energy in  $C_4$  discharges immediately, giving a sharp rise to the pulse, then  $C_3$ ,  $C_2$ , and  $C_1$  are used to provide the flat-top and high current capacity.



$$C_1 = C_2 = \dots = C_i = \dots = C_n = C$$

$$L_1 = L_2 = \dots = L_i = \dots = L_n = L$$

FIG. A1 LOW-PASS FILTER TYPE PULSE NETWORK .

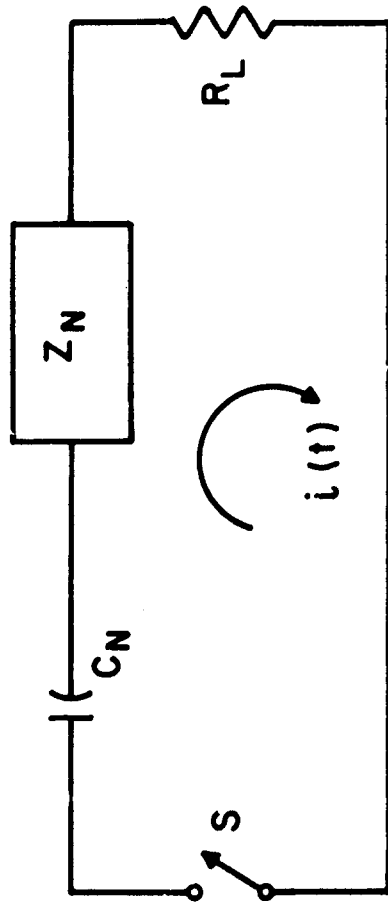


FIG. A2 PULSE - GENERATING CIRCUIT

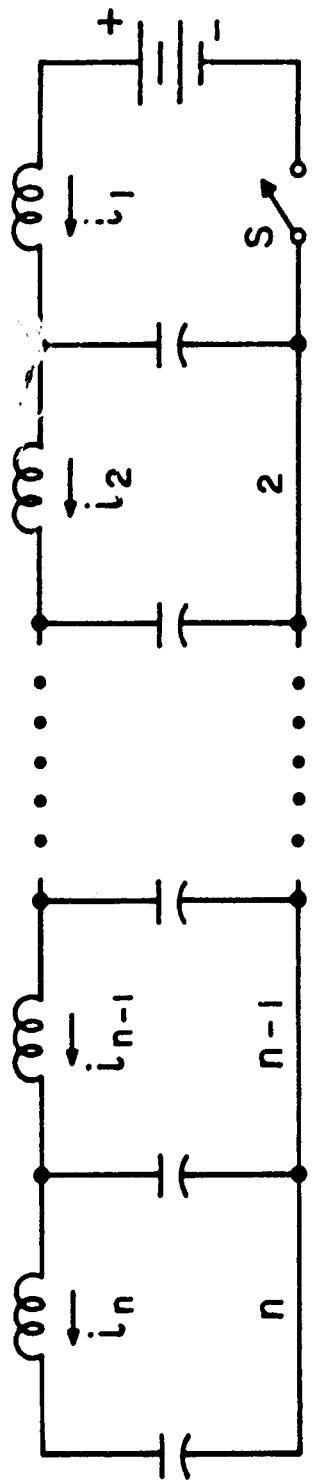


FIG. A3 LOW - PASS FILTER ANALYSIS.

## 7.2 APPENDIX B

### THEORY OF OPERATION OF THE CURRENT MONITOR PROBE

In the cylindrical geometry shown in Fig. (16) we have from Ampere's Law (using m.k.s. units),

$$\oint \frac{\vec{B}}{\mu_0} \cdot d\vec{l} = I(t) . \quad (B1)$$

Cylindrical symmetry implies

$$\frac{B(\rho, t)}{\mu_0} 2\pi\rho = I(t) \quad (B2)$$

or

$$B(\rho, t) = \frac{\mu_0 I(t)}{2\pi\rho} = 2 \times 10^{-7} \frac{I(t)}{\rho} \quad (B3)$$

The EMF(t) generated in the loop due to the time variation of B(ρ,t) is

$$EMF(t) = - \frac{d}{dt} \int_{loop} \vec{B}(\rho, t) \cdot d\vec{A} . \quad (B4)$$

From (3)

$$EMF(t) = - \frac{dI(t)}{dt} (2 \times 10^{-7}) \int_{\rho_1}^{\rho_2} \frac{1}{\rho} d\rho \int_{z_1}^{z_2} dz .$$

Whence

$$EMF(t) = - \frac{dI(t)}{dt} (2 \times 10^{-7}) \ln \frac{\rho_2}{\rho_1} (z_2 - z_1) . \quad (B5)$$

From Fig. (16)

$$\frac{\rho_2}{\rho_1} = 1.250; \quad \ln \frac{\rho_2}{\rho_1} = .22$$

$$z_2 - z_1 = 10^{-2} \text{ meters.}$$

Therefore

$$\text{EMF}(t) = - \frac{dI}{dt} (2 \times 10^{-7})(.22)(10^{-2}) . \quad (\text{B6})$$

At the input to the operational integrator (6) is reduced by a factor of 10 due to the 10:1 attenuator.

Therefore

$$e_{in}(t) = - \frac{dI}{dt} (.44)10^{-10} \quad (\text{B7})$$

The output of the integrator is

$$e_{out}(t) = - \frac{1}{R_i C_f} \int^t e_{in}(t) dt \quad (\text{B8})$$

where  $R_i$  is the input resistance to the integrator and  $C_f$  is the feedback capacitance around the operational amplifier. For  $R_i = 10^4 \Omega$  and  $C_f = .001 \mu f$  (values appropriate for integration of approximately 10  $\mu s$  pulses) we get

$$\begin{aligned} e_{out}(t) &= - \frac{1}{10^{-3}} \int^t - \frac{dI}{dt} (.44)10^{-10} dt \\ &= .44 \times 10^{-5} I(t) \end{aligned} \quad (\text{B9})$$

$$\text{Therefore: } I(t) = \frac{1}{4.4} \times 10^{-6} e_{out} = .227 \times 10^5 e_{out}$$

or finally,

$$I(t)(\text{amperes}) = 2.27 \times 10^5 \left( \frac{\text{amperes}}{\text{volt}} \right) e_{out}(\text{volts}) .$$

### 7.3 APPENDIX C

#### MEASUREMENT OF MAGNETIC FIELDS IN MOVING MEDIA

A fundamental physical quantity in many plasma studies is the self-induced magnetic field produced by plasma currents. The proper interpretation of the voltage generated in a simple coil probe by a magnetic field contained in a plasma which is moving with respect to the probe is often complex. An important physical example, the use of magnetic field probes in an electromagnetically driven shock tube, is examined here.

In a shock produced plasma with  $c \gg 0$  the magnetic field is assumed to be frozen in the moving hot gas and the problem of mapping the magnetic field's structure is reduced to the problem of correctly interpreting the effects produced by a magnetic field sweeping past a stationary monitoring instrument. The central idea behind the measurement is Faraday's Law, i.e. to measure the EMF induced in a coil of known dimensions due to the changing magnetic field. Once obtained, this EMF must be related to the magnetic field structure in the plasma. However, the relation of the observed EMF (which is a function of time) to the actual magnetic field requires careful analysis of Faraday's Law in moving media.

There is a general tendency to oversimplify the problem by incorrectly reasoning that since Faraday's Law predicts an EMF proportional to  $\frac{d\phi}{dt}$  straightforward integration of the EMF will yield  $\phi(t)$  and hence  $B(t)$ , since the area of the pick-up coil is fixed. The following discussion should help

temper this tendency by showing specifically under what conditions such time integration is valid.

Consider a magnetic field frozen into a high conductivity plasma which is moving with a constant velocity  $U\hat{i}$  in the + x direction with respect to the laboratory coordinate system. A prime on any quantity means that quantity is to be considered in the frame fixed in the moving plasma while unprimed quantities refer to the lab frame. Let the magnetic field be directed in the + z' direction (or, what is equivalent, the + z direction since the relative motion between the frames is only in the x direction) and let it be a function of x' only.

Consider a one turn rectangular coil of x dimension m and y dimension l, (i.e. Area = lm) at z = 0 with one leg at x = 0 (call this the left leg) and the other at x = m (call this the right leg). This situation is depicted in Fig. C1.

As the magnetic field  $B(x')$  moves across the coil there will be an EMF generated between the probe coil ends, a and b. How can we relate this observed EMF to  $B(x')$ ?

In the unprimed frame we have from Faraday's Law

$$EMF(t) = - \frac{d}{dt} \iint \vec{B} \cdot \vec{dA} \quad (C1)$$

which, applied to the coil geometry depicted in Fig. C1 implies,

$$EMF(t) = - \frac{d}{dt} \int_{x=0}^m \int_{y=0}^l B(x,t) dx dy \quad (C2)$$

The integrand in (C2) is a function of both x and t (unprimed) because of the relative motion of the two reference frames.

Since  $B(x,t)$  is independent of  $y$  we get,

$$EMF(t) = -l \frac{d}{dt} \int_{x=0}^{x=m} B(x,t) dx \quad (C3)$$

and since the limits of integration in (C3) are time independent, we can write

$$EMF(t) = -l \int_{x=0}^{x=m} \frac{\partial B}{\partial t} (x,t) dx \quad (C4)$$

We now inquire as to the nature of  $\frac{\partial B}{\partial t} (x,t)$ . Transform  $\frac{\partial B}{\partial t} (x,t)$  into the primed frame via the Galilean transformation ( $(\frac{v}{c})^2 \ll 1$ ):

$$x' = x - Ut \quad (C5a)$$

$$t' = t \quad (C5b)$$

Then

$$\frac{\partial}{\partial t} = \frac{\partial}{\partial x'} \frac{\partial x'}{\partial t} + \frac{\partial}{\partial t'} \frac{\partial t'}{\partial t} = \frac{\partial}{\partial t'} - U \frac{\partial}{\partial x'} \quad (C6)$$

and we note for later use that,

$$\frac{\partial}{\partial x} = \frac{\partial}{\partial x'} \frac{\partial x'}{\partial x} + \frac{\partial}{\partial t'} \frac{\partial t'}{\partial x} = \frac{\partial}{\partial x'} \quad (C7)$$

since  $\frac{\partial x'}{\partial x} = 1$  and  $\frac{\partial t'}{\partial x} = 0$ .

Equation (C4) now becomes

$$EMF(t) = -l \int_{x=0}^m \frac{\partial B(x')}{\partial t'} - U \frac{\partial B(x')}{\partial x'} dx \quad (C8)$$

But by the original frozen flux assumption\*  $\frac{\partial B(x')}{\partial t'} = 0$ . Using this and noting that  $\frac{\partial}{\partial x'} = \frac{\partial}{\partial x}$  we get.

$$EMF(t) = -U \ell \int_{x=0}^m \left[ -\frac{\partial B}{\partial x} \right] dx \quad (C9)$$

Integration gives

$$EMF(t) = -U \ell [B(0,t) - B(m,t)] \quad (C10)$$

Equation (C10) shows, immediately, that even for this idealized case the  $EMF(t)$  is not, in general, proportional to the time derivative of  $B$ , but is rather proportional to the difference between the field at the left and the field at the right hand side of the coil. It is only in the appropriate small probe limit that one can validly approximate (C9) by a time derivative of  $B$ . An exact discussion of this is deferred until later.

We now inquire as to how Eq. (10) can be used to map out the magnetic field in the plasma. The key to this lies in noting that, since  $B$  is a function of  $x'$  only, the field maintains its profile in moving across the coil.

Thus, the field at time  $t_1$  that exists at  $x = 0$  will be at  $x = m$  at

$$t_2 = t_1 + \frac{m}{U} \quad (C11)$$

---

\* The physical conditions required for frozen flux in shock produced plasmas have been examined by A. Kantrowitz, AVCO AERL RR 141 Oct. 1962. Also, 15th Solvay Conf. Belgium 1962. Essentially, the magnetic Reynolds number should be large compared to one.

For simplicity assume that  $t = 0$  when  $B(x')$  just impinges on the left leg of the probe. Then,

$$\text{for } 0 < t_1 < \frac{m}{U}$$

$$\text{EMF}(t_1) = -U \ell B(0, t_1) \quad (\text{C12})$$

since  $B(m, t_1) = 0$  until  $t_1 = \frac{m}{U}$  when  $B(x')$  first reaches  $x = m$ .

$$\text{For } \frac{m}{U} < t_2 < \frac{2m}{U},$$

$$\text{EMF}(t_2) = -U \ell [B(0, t_2) - B(m, t_2)] \quad (\text{C13})$$

But from (C11)

$$B(m, t_2) = B(0, t_2 - \frac{m}{U}) = B(0, t_1).$$

Therefore,

$$\text{EMF}(t_2) = -U \ell [B(0, t_2) - B(0, t_1)] \quad (\text{C14})$$

But, from (C12)

$$-U \ell B(0, t_1) = \text{EMF}(t_1) \quad \text{whence we}$$

get

$$\text{EMF}(t_2) + \text{EMF}(t_1) = -U \ell B(0, t_2).$$

Generalizing,

$$B(0, t_n) = \frac{\sum_{i=1}^n \text{EMF}(t_i)}{-U \ell} \quad (\text{C15})$$

where  $t_i$  is related to  $t_1$  by

$$t_i = t_1 + (i - 1) \left( \frac{m}{U} \right) \quad i = 1, \dots, n \quad (\text{C16})$$

and

$$0 < t_1 < \frac{m}{U} .$$

Equation (C15) allows us to map out  $B(0,t)$  for all times  $t > 0$ . In practice, the  $EMF(t)$  and  $U$  are observed experimentally, while  $m$  and  $l$  are known dimensions of the probe.

Before discussing the refinements of the above theory necessary for the interpretation of magnetic probes in situations where  $B = B(x',t')$ , let us return to the question of whether one is ever justified in simply integrating the  $EMF(t)$  to get  $B(0,t)$ . Assume that  $B(x')$  rises from an initial value of 0 to some constant value  $B_1$  over some distance measured in its own frame. If  $\frac{\partial B}{\partial x}$  is essentially constant over the probe width we may approximate Eq. (C9) by,

$$\begin{aligned} EMF(t) &= + U l \left( \frac{\partial B}{\partial x} \right) \left\{ \int_{x=0}^m dx \right\} \\ &= + U l m \left( \frac{\partial B}{\partial x} \right)_{x=0} \\ &= + U \left( \frac{\partial B}{\partial x} \right)_{x=0} A \end{aligned} \tag{C17}$$

where  $A$  is the area of the coil.

But we have already seen that

$$-U \frac{\partial B}{\partial x} = \frac{\partial B}{\partial t} \quad \text{whence}$$

$$EMF(t) = -A \frac{\partial B}{\partial t} (0,t) \tag{C18}$$

or

$$B(0,t) = - \frac{1}{A} \int^t EMF(t) dt \tag{C19}$$

The error involved in the approximation (C17) is  $O \left| \frac{\partial^2 B}{\partial x^2} \right| m^2$  where  $\left| \frac{\partial^2 B}{\partial x^2} \right|_{\max}$  is the maximum value of the absolute value of the second spatial derivative of B, and m is, as before, the probe width. Thus the small probe limit is only justified when  $\frac{m}{a} \ll 1$  where a is the distance over which  $\frac{\partial^2 B}{\partial x^2}$  has a significant value.

The above discussion has centered on the situation where one can transform from the lab frame to a reference frame in which the magnetic field is a function of  $x'$  only. In a magnetically-driven shock tube, however, there is a region in which the magnetic field is distributed throughout a rarefaction fan and consequently there is no reference frame in which B is totally time independent. An analysis will illustrate how one can recover  $B(x,t)$ , when we have a time dependence in the fluid frame. This is done for the special, but important, case of a rarefaction fan which is a simple centered wave.

The  $x-t$  diagram for an electromagnetically-driven shock tube is shown in Fig. C2, where region 0 is the cold upstream gas; region 1 the shock heated gas where  $B$  is a constant  $= B_1$ ; region 2 is the simple centered rarefaction wave where  $B = B\left(\frac{x}{t}\right)$ ; region 3 is the constant state behind the wave where  $B$  is again constant  $= B_{\max}$ ; where  $x_1$  and  $x_1 + m$  are the left and right hand sides of the pick-up probe, respectively; and where  $U$ ,  $U_1$  and  $U_2$  are, respectively, the shock velocity, the velocity of the leading edge of the rarefaction wave, and the velocity of the trailing edge of the rarefaction wave.

Up to time  $t_1$ , (see Fig. C3) the probe sees a magnetic field of the time independent variety discussed above, and hence the above analysis applies up to  $t_1$ . After

$t_1$ , however, the probe experiences the time-varying field in the rarefaction wave and we must, therefore, re-examine the effects produced.

Referring to Fig. C3, which is a detail of Fig. C2, we see that for

$$t_1 < t < t_2$$

the left hand side of the probe is in the rarefaction fan while the right hand side is still in the time-independent region. Thus, the right-hand side generates a voltage =  $UB_1 l$  while the left-hand side generates a voltage =  $U_{x_1} B(x_1, t) l$  where  $U_1 < U_{x_1} < U_2$  is the velocity of the characteristic cutting  $x_1$  at time  $t_1 < t < t_2$ . The EMF actually observed is the difference between these two voltages since each generates the same polarity voltage and, therefore, we have

$$EMF(t_1 < t < t_2) = U_{x_1} B(x_1, t) l - UB_1(m, t) l \quad (C20).$$

Assuming we know  $U_{x_1}$ , we know  $B(x_1, t_1 < t < t_2)$  because we know  $B_1, l$ , and  $U$ . That  $U_{x_1}$  is, in fact, known remains to be discussed.

Continuing to the region  $t_2 < t < t_3$  and realizing that  $B = B(\frac{x}{t})$  we see that  $B(x_1, t_1 < t < t_2)$  is transported to  $(x_1 + m)$  and appears there for  $t_2 < t < t_3$ . Knowing  $B(x_1 + m, t_2 < t < t_3)$  we calculate  $B(x_1, t_2 < t < t_3)$  as follows:

$$EMF(t_2 < t < t_3) = U_{x_1}(t) B(x_1, t) l - U_{x_2}(t) B(x_1 + m, t) l \quad (C21)$$

where  $U_{x_i}$  ( $i = 1, 2$ ) means the characteristic velocity in the rarefaction wave at time  $t$  at position  $x_i$ , (Note:  $x_2 \equiv x_1 + m$ ).

But,

$$B(x_1 + m, t_2 < t < t_3) = B(x_1, t_1 < t' < t_2)$$

where  $B(x_1, t_1 < t' < t_2)$  represents the already calculated value of  $B$  at  $x_1$  and at time  $t_1 < t' < t_2$  that is convected to  $x_1 + m$  at time  $t_2 < t < t_3$ . Consequently, we get

$$EMF(t_2 < t < t_3) = U_{x_1}(t) B(x_1, t) - U_{x_2}(t) B(x_1, t_1 < t' < t_2) \quad (C22).$$

In this way  $B(x_1, t)$  is calculated for all  $t > t_1$ .

There remains for us to examine how one determines  $U_{x_i}$ . Taussig<sup>25</sup> has shown that for any reasonable situation in an electromagnetically-driven shock tube  $U_{x_i}$  decreases almost linearly between  $U_1$  and  $U_2$ . If we know  $U_1$  and  $U_2$  we linearly interpolate at any  $t$  between  $U_1$  and  $U_2$  and get  $U_{x_i}$  at that time. To determine  $U_1$  and  $U_2$  we note that for the situation depicted, the field starts at 0 and eventually for  $t > t_4$  reaches a constant value  $B_{max}$ . Therefore, beyond  $t_4$  there is no EMF generated across the probe.

In the lab we see the EMF rise to a maximum and then fall to 0 at  $t_4$ . If one measures the velocity of this point at which the EMF goes to 0 one has measured  $U_2$ . To get  $U_1$  map  $B(x_1, t)$  using (C15) for  $t > 0$  until the point is reached where  $B_1$  begins to depart from its constant value. This is the point that corresponds to the leading edge of the rarefaction fan and the velocity of this point is  $U_1$ . Thus one gets  $U_1$  and  $U_2$  for use in measuring  $B$  for all  $t$ .

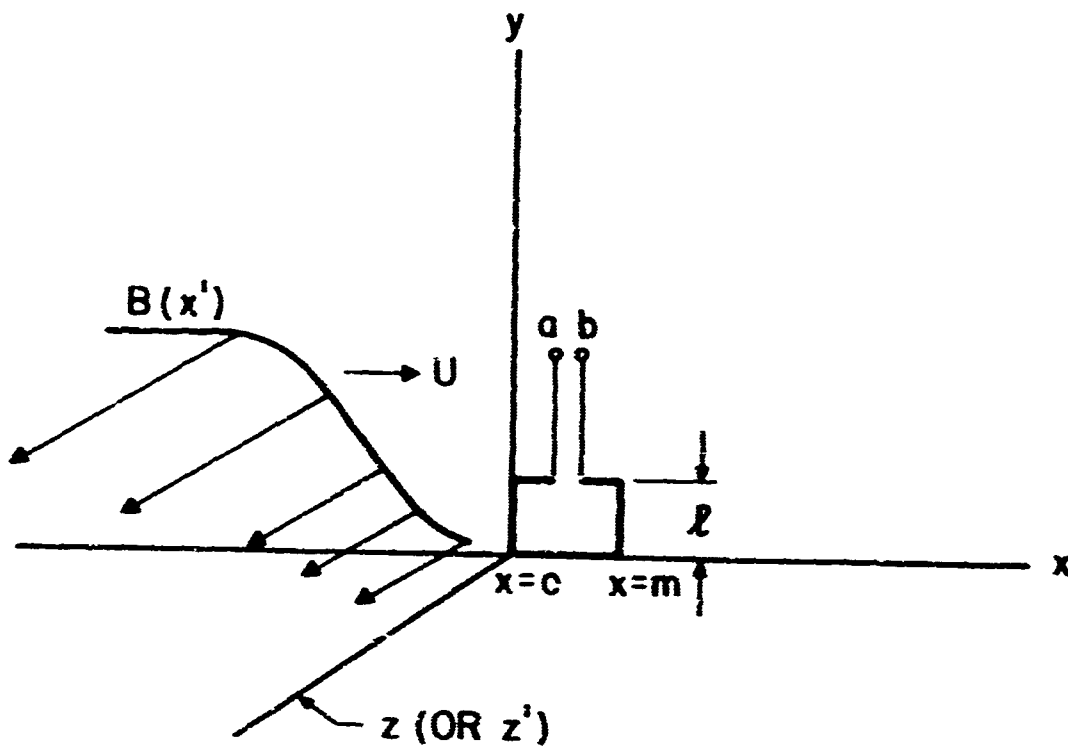


FIG. C1 PROBE GEOMETRY AND MOVING  
FIELD CONFIGURATION

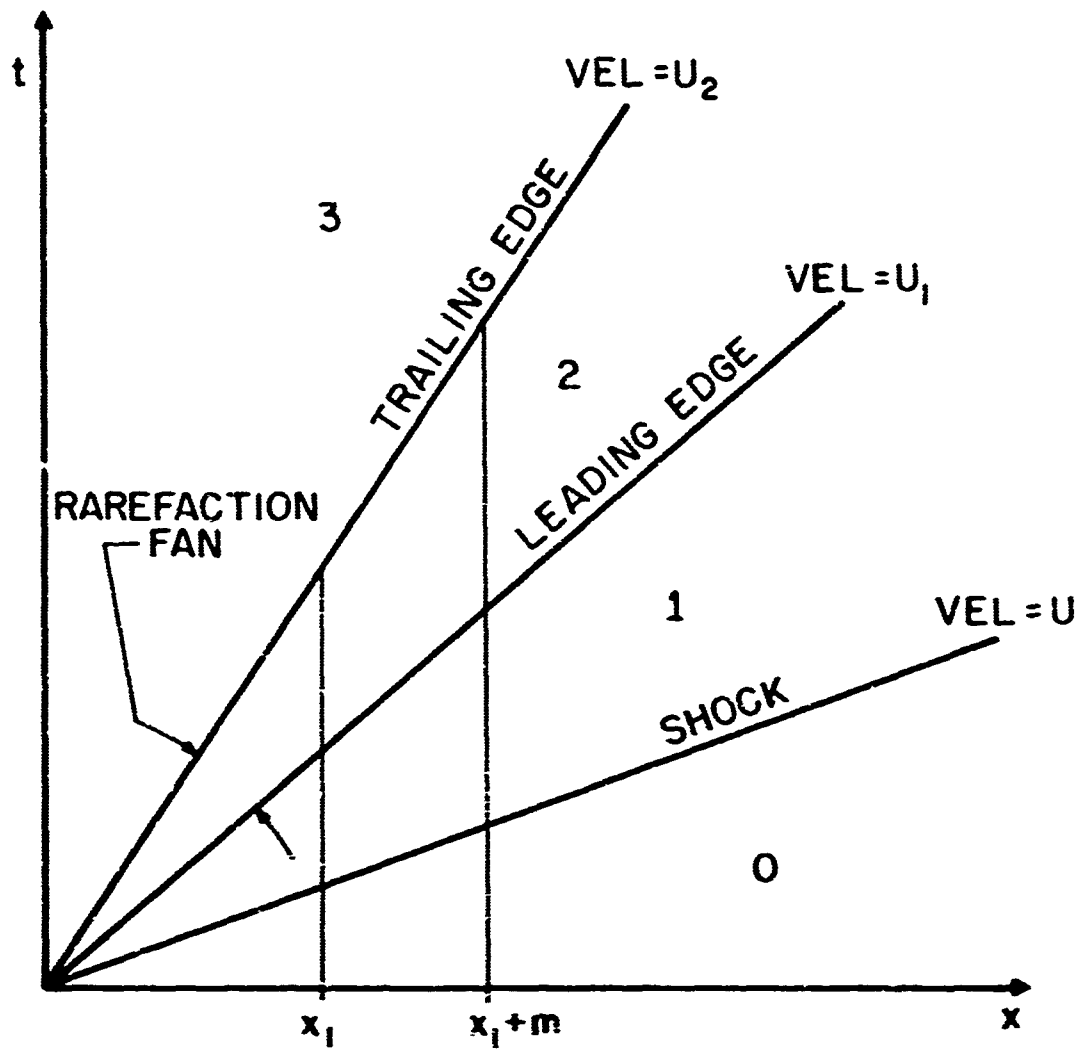


FIG. C2 SHOCK TUBE  $x-t$  DIAGRAM

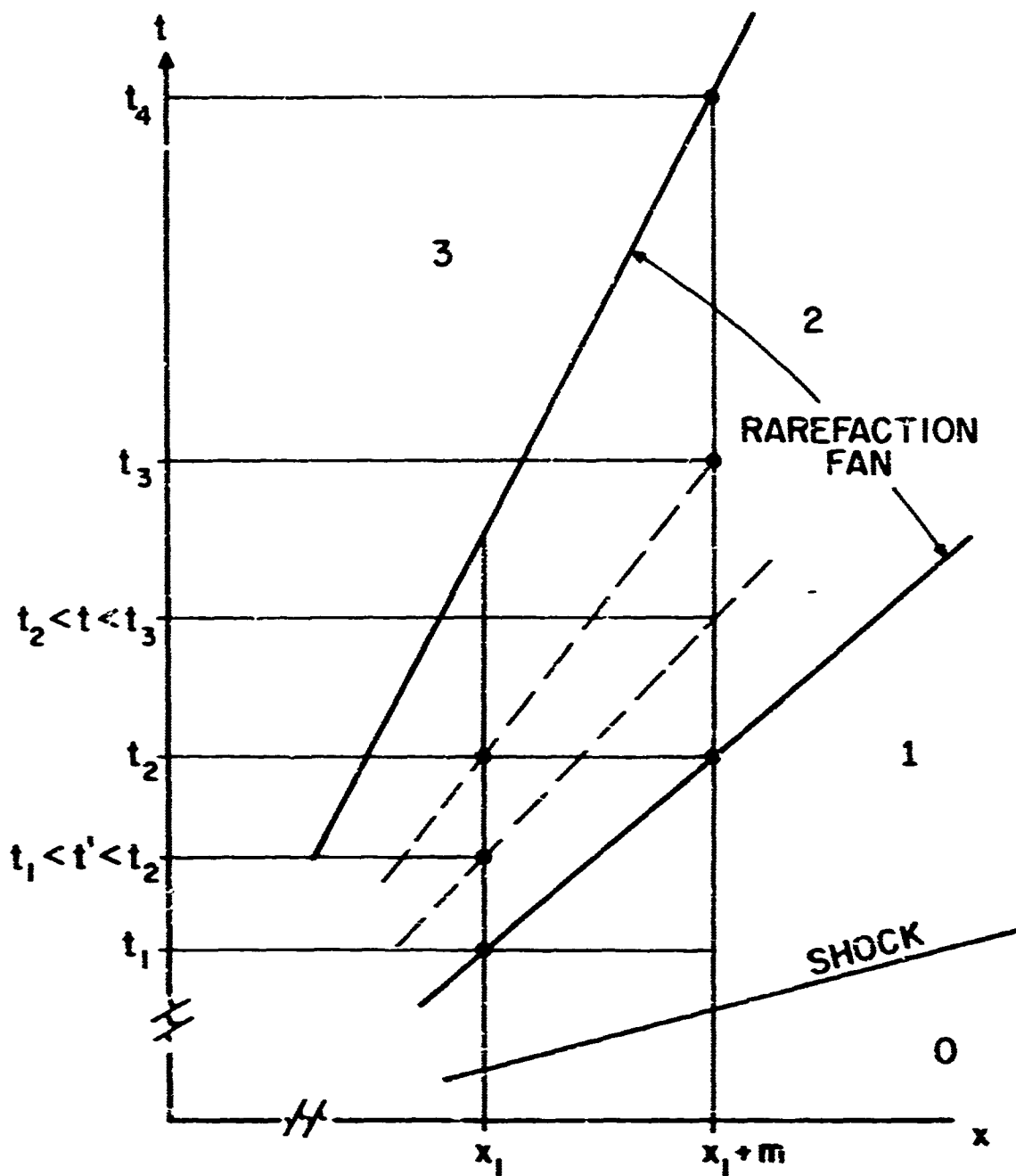


FIG. C3 DETAILS OF  $x-t$  DIAGRAM

## 7.4 APPENDIX D

### SHOCK WIDTH AND SHOCK FORMATION STUDY

As a by-product of the study described in the text, we present here two interesting results.

The first concerns an estimate of the width of the ionizing shock front and rarefaction fan. From analysis of the  $B_{\theta}$  data, we conclude that in all cases the shock width is of the order of 2 cm., while the rarefaction fan is of the order of 4 - 5 cm. From the data of Table IV, we can derive that the hgs is of the order of 2 - 3 cm.

The second result involves a study of ionizing shock formation time. From gas dynamics, it has been shown<sup>34</sup> that the stronger the shock is, i.e. the higher the ratio of shock speed to sound speed, the more rapidly it forms; i.e. it takes fewer mean collision times to reach a steady state. We would expect to observe this same general feature in ionizing shocks, and this is, indeed, the case. Fig. D1 shows a composite study of three different shocks, ranging from weak ( $M_a > .2$ ) to strong ( $M_a = 2.3$ ). It should be noted that here the relevant ratio is wave speed to Alfvén speed. The strong shock is well-formed by 20 cm., while the weak shock is barely formed at 35 cm. The intermediate case is not formed at 20 cm, but is well-formed at 35 cm. This result should bring attention to the fact that ionizing shock strength plays an important role in shock formation time in electromagnetic shock tube technology.

# SHOCK FORMATION STUDY

PRESSURE : 125 microns      BANK VOLTAGE : 10 KV

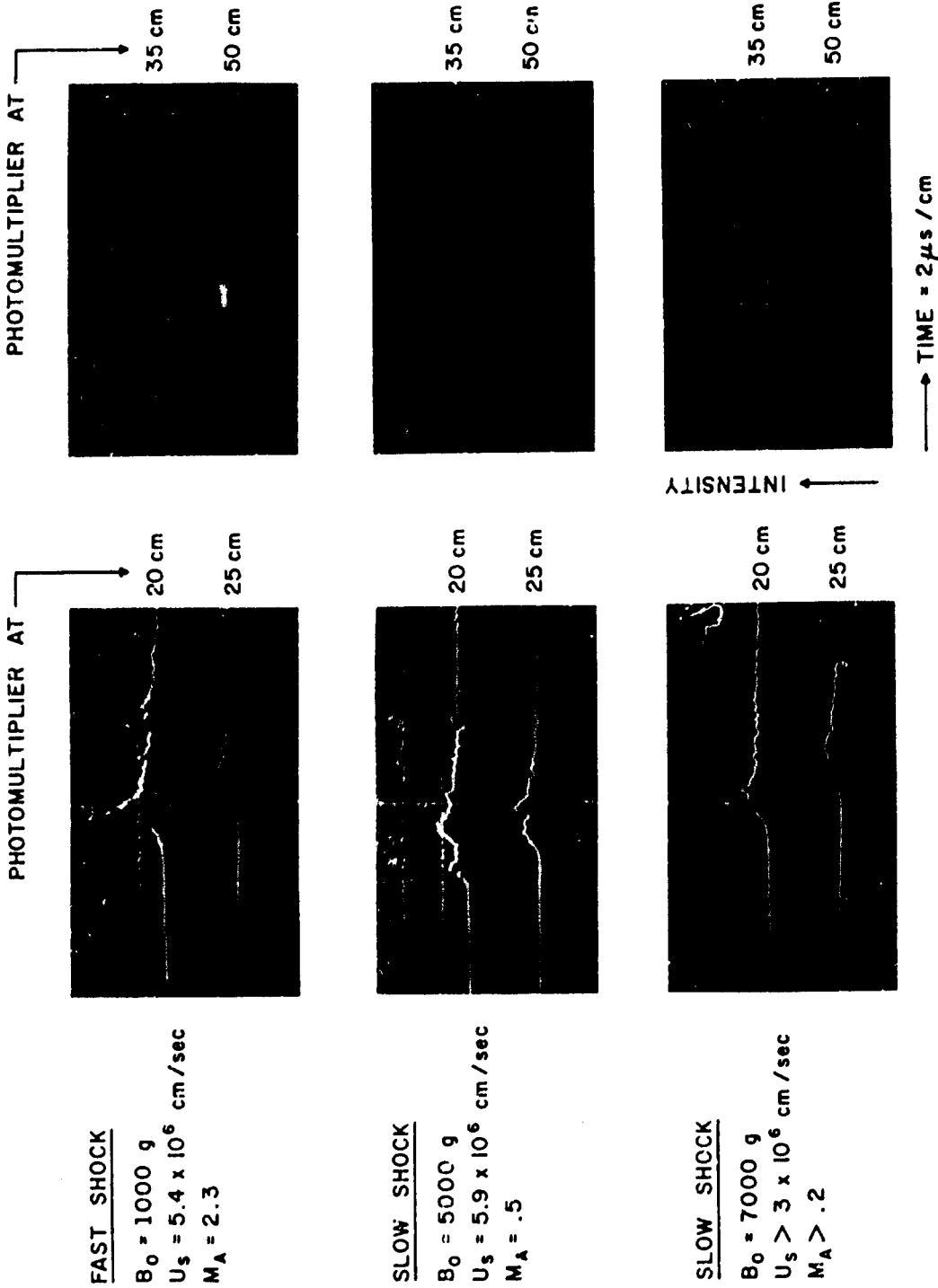


FIG. D1